Experimental studies of fluctuations in a reconnecting current sheet

Troy Alan Carter

A DISSERTATION

PRESENTED TO THE FACULTY

OF PRINCETON UNIVERSITY

IN CANDIDACY FOR THE DEGREE

OF DOCTOR OF PHILOSOPHY

RECOMMENDED FOR ACCEPTANCE

BY THE DEPARTMENT OF

ASTROPHYSICAL SCIENCES

NOVEMBER, 2001

Abstract

The role of turbulence in the process of magnetic reconnection has been the subject of a great deal of study and debate in the theoretical literature. At issue in this debate is whether turbulence is essential for fast magnetic reconnection to occur in collisionless current sheets. Some theories claim it is necessary in order to provide anomalous resistivity, while others present a laminar fast reconnection mechanism based on the Hall term in the generalized Ohm's law. In this work, a thorough study of fluctuations in the current sheet of the Magnetic Reconnection Experiment (MRX) was performed in order to ascertain the importance of turbulence in a laboratory reconnection experiment. Using amplified Langmuir and magnetic probes, broadband fluctuations in the lower hybrid frequency range ($f_{\mathrm{LH}} \sim 5 - 15$ MHz) were measured which arise with the formation of the current sheet in MRX. The frequency spectrum, spatial amplitude profile, and spatial correlations in the measured turbulence were examined carefully, finding consistency with theories of the lower-hybrid drift instability (LHDI). The LHDI and its role in magnetic reconnection has been theoretically studied for decades, but this work represents the first detection and detailed study of the LHDI in a laboratory current sheet. The observation of the LHDI in MRX has provided the unique opportunity to uncover the role of this instability in collisionless reconnection. It was found that: (1) the LHDI fluctuations are confined to the low-beta edge of current sheets in MRX;

(2) the LHDI amplitude does not correlate well in time or space with the reconnection electric field, which is directly related to the rate of reconnection; and (3) significant LHDI amplitude persists in high-collisionality current sheets where the reconnection rate is classical. These findings suggest that the LHDI does not play an essential role in determining the reconnection rate in MRX.

Dedicated to my wife, Rebecca

Acknowledgments

I would first like to thank my advisors, Dr. Masaaki Yamada, Prof. Russell Kulsrud, and Dr. Hantao Ji for their guidance and instruction during my dissertation research. I am grateful to Masaaki for his constant encouragement and for teaching me his dedication to high-quality experimental research. I have truly appreciated the opportunity to work with Russell[1], who is perhaps the best teacher I have ever had inside or outside of the classroom. Hantao has been an excellent advisor and an even better friend, spending countless hours with me in the lab or in his office, where he was quick to provide encouragement during even the most frustrating periods of my dissertation work.

I thank the faculty of the Program in Plasma Physics at Princeton for their excellent instruction. In particular, I would like to thank Prof. Ron Davidson and Dr. Stewart Zweben for their reading of this dissertation and Dr. Stephen Jardin for supervising my second year theoretical project. I owe a great deal to Barbara Sarfaty for her administrative help during my years at Princeton and for the many pleasant conversations I have enjoyed in her office.

I would like to thank the many past and present collaborators on the MRX project, especially Dr. Scott Hsu, Dr. Fedor Trintchouk, Sorin Zaharia, Kyle Morrison, Luis Delgado-Aparicio, Yang Ren, and the numerous undergraduate students

[1] I narrowly avoided being Russell's last student to graduate, losing that title to Leonid Malyshkin by probably less than a month.

who have spent time working on MRX participating in the NUF, ERULF or other summer programs. I would like to thank Dave Cylinder, Bob Cutler, Jim Taylor, Don Long, Bob Marsala, and Gary Gibilisco for their excellent technical support. In particular, I would like to thank Dave not only for his expert assistance in designing and constructing (and often reconstructing!) the diagnostics used to make measurements in this thesis, but also for his friendship.

I have made many good friends while a graduate student at Princeton; knowing them has made my stay very enjoyable. These include Scott Hsu, Phil Snyder, Joel Shapiro, Mike Towns, Kevin Narizny, John Thomson, Wade Crow, and Tobin Munsat, among others. I also enjoyed the company of my classmates during the plasma physics program; thanks to Josh Breslau, Alex Schekochikin, Andrei Litvak, and Sean Strasburg. I thank Jill Foley for her friendship and for putting up with me as an officemate. I have spent way too much time dabbling with Linux[2], and I give partial blame for this to Jef Spaleta, who was always available to discuss (at length) the finer points of the operating system.

My parents have been a source of constant support during my many years as a student, and I thank them for their love and encouragement. Last, but certainly not least, I would like to thank my wife, Rebecca. Having her, and now our son, Matthew, in my life has made me immensely happy. Becky, I love you very much, and for everything you endured and did to make it possible, I dedicate this dissertation to you.

I gratefully acknowledge financial support from a National Science Foundation Graduate Fellowship (1995-1998) and from a National Space and Aeronautics Administration Graduate Researchers Program Fellowship (1998-2001).

[2]This dissertation was, of course, typeset on a Linux workstation using LaTeX 2_ε (actually, pdfLaTeX).

Contents

List of Figures

Chapter 1

Introduction

MAGNETIC RECONNECTION is an important process in magnetized plasmas which results in rapid release of magnetic energy and rapid changes in magnetic topology even in highly conductive plasmas [see, e.g. BISKAMP, 1994]. The rapid energy release in this process is thought to be the source of solar flares and heating in the solar corona [MASUDA *et al.*, 1994; PREIST *et al.*, 1998], particle acceleration in the magnetosphere (causing phenomena like the Aurora) [MCPHERRON, 1979], and ion heating in some magnetic fusion devices [HOWELL and NAGAYAMA, 1985]. The topological change associated with this process can lead to global effects such as enhanced particle and heat transport (e.g. sawteeth and IRE's in fusion plasmas [YAMADA *et al.*, 1994]) and loss of equilibrium and confinement (e.g. coronal mass ejections in the solar corona [ANTIOCHOS *et al.*, 1999]). Magnetic reconnection has been studied theoretically and experimentally for decades. While much progress has been made in our understanding of the problem, many key issues remain either unresolved or their proposed solutions are currently controversial. The primary focus of this dissertation

is a study of plasma turbulence and its role in the process of magnetic reconnection. This topic is at the heart of an important question in reconnection: what is the physical mechanism behind magnetic energy dissipation in collisionless magnetic reconnection?

First, a proper introduction to the problem of magnetic reconnection must be given. We will start with heuristic arguments and quantitative derivations based on the resistive magnetohydrodynamic (MHD) model, which is quite appropriate for application on macroscopic scales in plasmas such as the solar corona. The governing equation for the magnetic field in a resistive MHD plasma can be constructed from Faraday's law:

$$\frac{\partial \mathbf{B}}{\partial t} = -\frac{1}{c}\nabla \times \mathbf{E}$$

and Ohm's law, which is an approximation to the electron fluid momentum equation:

$$\mathbf{E} + \frac{\mathbf{v} \times \mathbf{B}}{c} = \eta \mathbf{j}$$

Ohm's law states that the electric field in the reference frame of the plasma is balanced by friction due to Coulomb collisions. The resistive MHD induction equation is then:

$$\frac{\partial \mathbf{B}}{\partial t} = \underbrace{\nabla \times (\mathbf{v} \times \mathbf{B})}_{\sim B/\tau_{\mathrm{A}}} + \underbrace{\frac{\eta c^2}{4\pi}\nabla^2 \mathbf{B}}_{\sim B/\tau_{\mathrm{R}}} \tag{1.1}$$

Two timescales are present in this equation, the Alfvén timescale $\tau_{\mathrm{A}} = L/v_{\mathrm{A}}$, and the resistive timescale $\tau_{\mathrm{R}} = 4\pi L^2/\eta c^2$, where L is the scale length of the magnetic field. The resistive timescale represents the time for the magnetic field to diffuse over the scale length L. It also represents the timescale for magnetic energy dissipation in this model. The Alfvén timescale, τ_{A}, is the time for an Alfvén wave

to propagate over a distance L, and represents the fastest timescale over which the magnetic field can change in the MHD model. A dimensionless number $S = \tau_R/\tau_A$ can be defined from these two timescales, which is called the Lundquist number. As this dimensionless number becomes very large, $S \rightarrow \infty$ (or, equivalently, on timescales much shorter than the resistive timescale, τ_R), Eqn. 1.1 tends toward the ideal MHD equation for the magnetic field:

$$\frac{\partial \mathbf{B}}{\partial t} = \nabla \times (\mathbf{v} \times \mathbf{B})$$

The ideal MHD induction equation has very important conservation properties, most notably the topology of the magnetic field and the number of field lines (and magnetic flux) are conserved. In this limit, the magnetic field is said to be "frozen" into the plasma, meaning that the two move together and diffusion of one relative to the other is not possible.

In some physical systems with large S, such as the solar corona, topological change and energy release are observed on time scales much shorter than τ_R. This behavior might be allowed in a resistive MHD plasma by the formation of sharp gradients in the magnetic field, called current sheets[1] [SYROVATSKII, 1971]. In these current sheets, the scale sizes are such that the resistive term becomes important and magnetic energy dissipation and topological change are possible. These fine-scale structures can be developed through macroscopic flows in an MHD plasma. As an example, consider magnetic loops in the solar corona, an observation of which by the TRACE[2] satellite is shown in Figure 1.1. The structure in this EUV

[1] In this dissertation, "current sheet" will refer to what is typically called a neutral sheet, where the magnetic field reverses direction across a region of large current density

[2] Transition Region and Coronal Explorer, TRACE, is a mission of the Stanford-Lockheed Institute for Space Research, and part of the NASA Small Explorer program.

image is due to magnetic fields emerging from the photosphere of the sun. Figure 1.2(a) is an two-dimensional illustration of two magnetic loops, motivated by this type of observation[3]. The field lines lie in two types of regions: "private" re-

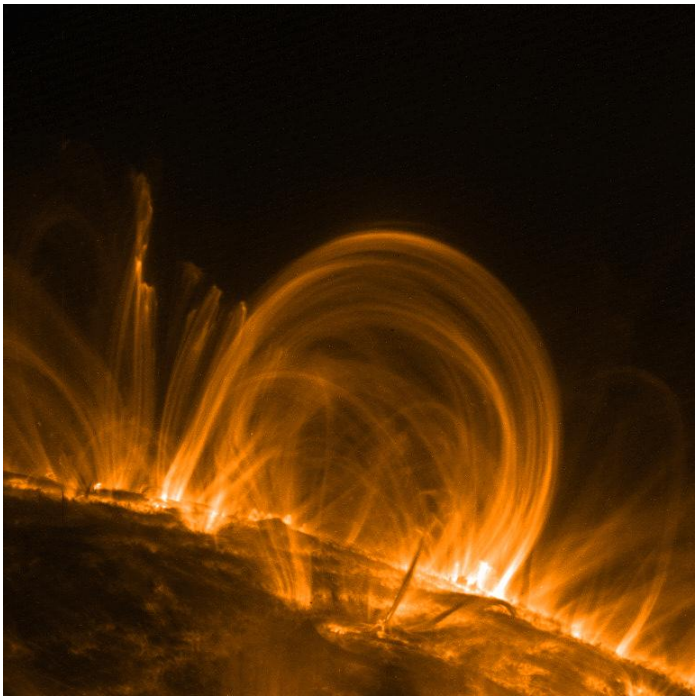

Figure 1.1: Extreme ultraviolet image of the Sun's surface showing coronal loops. (Image courtesy of TRACE)

gions in which field lines are confined to one loop, and "public" regions in which the field lines connect to both loops. The foot points of the two loops are in the photosphere of the sun, and are imagined to be convected by fluid motions along the surface. This convection might lead to a situation like that shown in Figure 1.2(b), where the loops are forced toward one another. If a highly conducting plasma is present on the field lines, no electric field would be allowed to develop at the null line (N), and therefore no flux would be allowed to pass from the "private" regions

[3]This scenario is originally due to SWEET [1958]; figures from KULSRUD [1998].

to the "public" region. A current density will arise at the null point to resist the attempt to push flux through the null point, and a current sheet will be formed. The current sheet will thin and the current density will build until the point that dissipation becomes significant and the frozen-in condition is broken. At this point, magnetic field lines from the private regions can diffuse through the null point, where may break and "reconnect" with lines from the other private region, leading to a final state shown in Figure 1.2(c). The rate at which this process, called magnetic reconnection, should proceed has been the topic of theoretical studies for decades.

1.1 2-D, Steady-State Resistive MHD Models of Reconnection

1.1.1 Sweet-Parker reconnection

The first quantitative model of magnetic reconnection was proposed by SWEET [1958] and PARKER [1957]. The current sheet geometry in the Sweet-Parker model is shown in Figure 1.3. The model assumes steady-state resistive MHD with constant inflow velocity u and outflow velocity v, using the steady-state momentum equation (ignoring magnetic tension):

$$\rho(\mathbf{v}\cdot\nabla)\mathbf{v} = -\nabla\left(p + \frac{B^2}{8\pi}\right)$$

and the steady-state induction equation, with a classical collisional resistivity, η:

$$\frac{\partial \mathbf{B}}{\partial t} = 0 = \nabla\times(\mathbf{v}\times\mathbf{B}) + \frac{\eta c^2}{4\pi}\nabla^2\mathbf{B}.$$

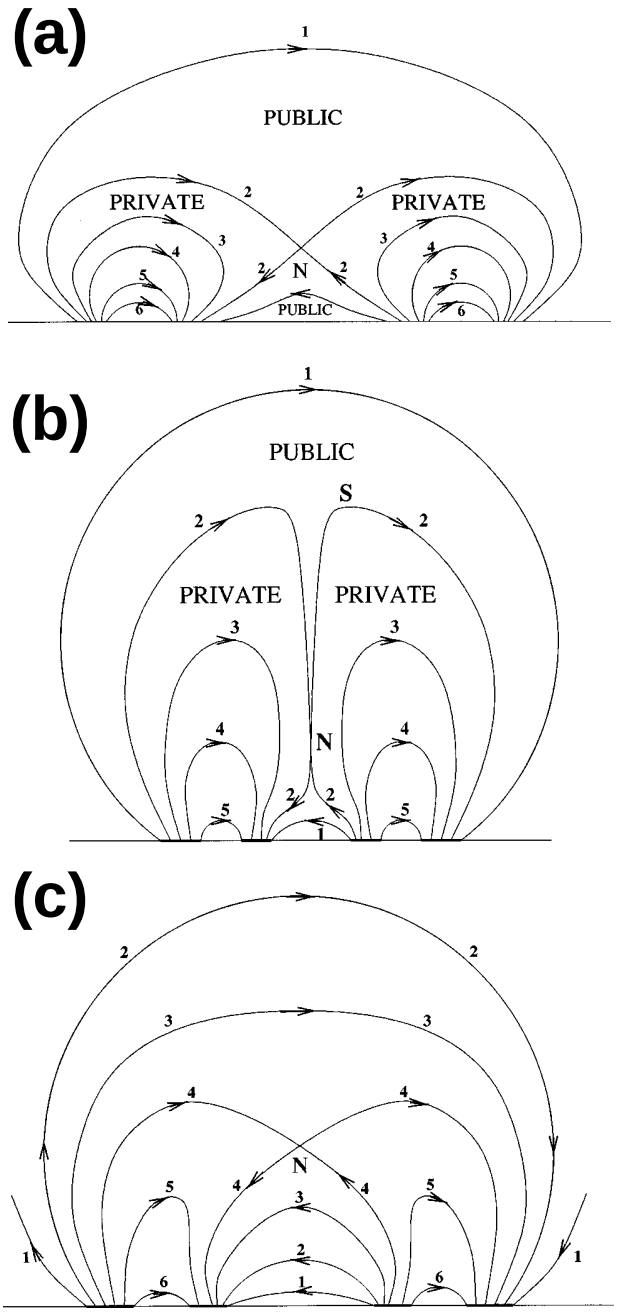

Figure 1.2: Illustration showing a two-dimensional example of current sheet formation due to macroscopic flows. (a) Two magnetic loops prior to photospheric forcing. (b) Formation of a current sheet (at N) due to forcing. (c) Field line structure after the lines are allowed to break and reconnect at the current sheet.

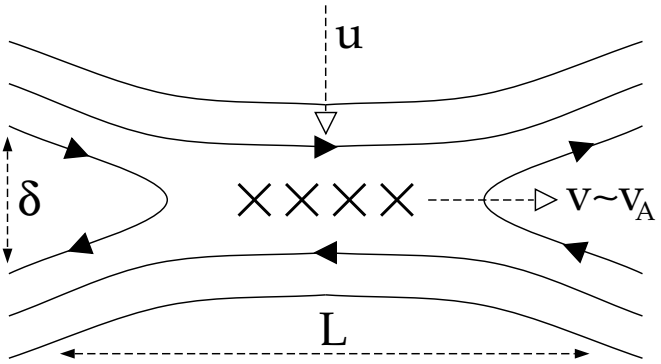

Figure 1.3: Sweet-Parker current sheet geometry.

The momentum equation can be integrated along a streamline to obtain a magnetic Bernoulli equation:

$$\frac{\rho v^2}{2} + p + \frac{B^2}{8\pi} = \text{constant}$$

Evaluating this equation from the upstream region to the center of the current sheet, assuming velocity gradients are small, we find $\Delta p = B^2/8\pi$, where Δp is the plasma pressure difference between the upstream region and the current sheet. A second application of the Bernoulli equation to the outflow region (assumed to be magnetic field-free) results in the determination of the outflow speed:

$$v = \sqrt{\frac{B^2}{4\pi\rho}} = v_{\mathrm{A}}$$

The induction equation tells us that any magnetic field which is brought into the current layer is resistively destroyed:

$$u\frac{B}{\delta} = \frac{B}{\delta^2}\frac{\eta c^2}{4\pi}$$

We now need an additional condition to get both δ and u; the continuity equation provides this constraint. If we assume that the flow is incompressible, we have the simple expression:

$$uL = v\delta = v_A\delta$$

Combining this with the induction equation, we find that the inflow speed normalized to the Alfvén speed is:

$$\frac{u}{v_{\mathrm{A}}} = \sqrt{\frac{1}{S}} \tag{1.2}$$

The time to reconnect a macroscopic piece of flux can be estimated from this result:

$$\tau_{\mathrm{rec}} = \frac{L}{u} = \sqrt{\tau_A \tau_R}$$

This timescale is significantly faster than the resistive diffusion timescale, τ_{R}, but is still too slow to explain observed timescales in natural phenomena such as solar flares. Solar flares are observed on timescales of tens of minutes to a few hours, while the Sweet-Parker model predicts reconnection timescales of a few months. For this reason, the Sweet-Parker theory is sometimes called "slow" reconnection. The bottleneck in Sweet-Parker reconnection is the tie between the dissipation rate (η) and width of the current sheet. In order for the resistive term to be effective, the current sheet scale must shrink to the point where collisional dissipation is significant. The resulting narrow sheet, coupled with a fixed outflow velocity, limits the outflow mass flow rate, which in turn limits the inflow and hence the reconnection rate. The challenge for reconnection researchers in the decades following the introduction of the Sweet-Parker model has been to determine what new physics must be added to this picture to achieve the fast timescale reconnection which is observed in nature.

1.1.2 Petschek reconnection

PETSCHEK [1963] proposed a solution to the mass outflow bottleneck in the Sweet-Parker model. In this model it is proposed that slow-mode shocks, propagating in the upstream direction, might develop in the outflow region of a Sweet-Parker

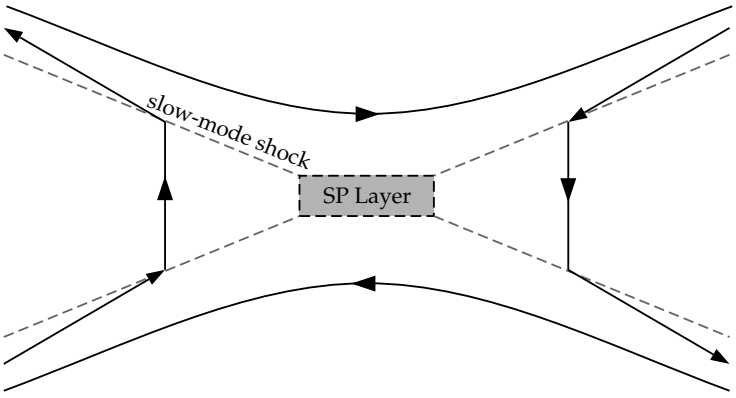

Figure 1.4: Current sheet geometry for Petschek reconnection

current layer, as shown in Figure 1.4. Breaking of the frozen-in condition occurs in the small Sweet-Parker layer, however, most of the mass can bypass this small layer by moving across the shocks, where it is accelerated to the Alfvén speed in the outflow direction. The aspect ratio of the current sheet is near unity, allowing nearly Alfvénic inflow in the incompressible case. The reconnection rate in the Petschek model is fairly insensitive to the value of the resistivity (the rate is found to go as $\ln S$), and is therefore attractive for collisionless plasmas where dissipation is small. However, it was pointed out by BISKAMP [1986] that Petschek's shocks could not be created self-consistently in a current sheet governed by resistive MHD, if a current-independent resistivity, such as the Spitzer resistivity, is employed. Later simulations [see, e.g. UZDENSKY and KULSRUD, 2000] have confirmed that Petschek current sheets can not be supported by resistive MHD alone.

1.2 Non-MHD reconnection

A starting point that is often chosen for extending the single fluid resistive MHD models of magnetic reconnection is an investigation of ignored terms in the generalized Ohm's law (or momentum equation for the electron fluid)[4]:

$$\underbrace{\mathbf{E}+\frac{\mathbf{v}\times\mathbf{B}}{c}=\eta\mathbf{j}}_{\text{resistive MHD}}+\underbrace{\eta^{*}\mathbf{j}}_{\text{turb.}}+\underbrace{\frac{\mathbf{j}\times\mathbf{B}}{nec}}_{\text{Hall}}+\frac{\nabla\cdot\mathbf{P}}{ne}+\underbrace{\frac{m_{\mathrm{e}}}{e^{2}}\mathbf{v}_{\mathrm{e}}\cdot\nabla\frac{\mathbf{j}}{n}}_{\text{inertia}} \tag{1.3}$$

The two terms which have been most often invoked to explain fast reconnection are the anomalous resistivity term (due to fluctuations), $\eta^{*}\mathbf{j}$, and the Hall term ($\mathbf{j}\times\mathbf{B}/nec$). Theories based on these two terms have opposing views of the importance of turbulence in reconnection: turbulence is essential for theories based on anomalous resistivity while a laminar fast reconnection mechanism is found using the Hall term.

1.2.1 Turbulence and anomalous resistivity

One of the earliest suggestions to speed up the rate of reconnection in the Sweet-Parker model was a turbulently enhanced, or anomalous, resistivity [Syrovatskii, 1972]. Current sheets have many sources of free energy associated with them, including currents and gradients in density, temperature, and flows. These can drive unstable fluctuations in the current sheet, and the resulting turbulence can enhance the scattering rate of the current carrying particles, and thus result in an anomalously large resistivity [Buneman, 1958; Hamburger and Friedman, 1968]. The

[4]The turbulent resistivity term ($\eta^{*}j$) can be introduced to Ohm's law through a wave-particle collision operator in the Boltzmann equation prior to taking the first velocity moment. It may also be possible to introduce this term through a perturbation expansion of Ohm's law, where the first order terms are grouped into $\eta^{*}j$.

resistivity enhancement helps alleviate the bottleneck in Sweet-Parker reconnection by increasing the dissipation rate and widening the current sheet. When turbulence arises due to an instability, the thickness of the current sheet might be determined by the marginal state of the instability. During the process of current sheet formation, the sheet thickness collapses until the threshold for the instability is reached and then sufficient turbulent dissipation arises to limit the sheet current and prevent further collapse. The Sweet-Parker reconnection rate in a turbulent current sheet is still inversely proportional to the square-root of the Lundquist number, but now the Lundquist number is based on the turbulent resistivity and not the classical value. In addition to providing a mechanism to speed up Sweet-Parker reconnection, turbulent resistivity may also allow Petschek reconnection to occur in the case that the turbulent resistivity value depends on the current density. Simulations using a current-dependent resistivity have shown that Petschek-like reconnection is possible [UGAI, 1995], and KULSRUD [1998] has given a physical argument to explain this based on the regeneration of in-plane magnetic field components by a current-dependent turbulent resistivity. The instabilities which are operative in a current sheet depend crucially on the equilibrium configuration of the sheet, especially on the presence of a "guide" field along the current direction (out of the page in Figure 1.3). It is believed that current sheets in the solar corona likely contain guide fields, although current sheets in the magnetosphere can be free of such fields. We will focus on the case of no guide field in our discussions, motivated by the types of experiments which will be presented in this dissertation.

There have been extensive theoretical investigations of instabilities which could provide a turbulent resistivity in a reconnecting current sheet. Several of these instabilities have essentially been ruled out based on recent understandings of the

characteristics of the natural environments in which reconnection takes place. In particular, it is now known that a proposed instability must operate with large ion to electron temperature ratio ($T_i/T_e \sim 1$) and with only moderate drift speeds between the electrons and ions ($j/ne \sim v_{th,i}$). Instabilities which have previously been proposed, but which most likely would not be important in these situations include the Buneman instability[5] [HEYVAERTS *et al.*, 1977], the electron cyclotron drift instability [HAERENDEL, 1978], and the ion acoustic instability [CORONITI and EVITAR, 1977]. High frequency instabilities ($\omega > \omega_{p,i}$) such as the Buneman instability are unlikely to produce a resistive effect, even if they were excited in the current sheet. A phenomenon causing resistivity must be able to limit the current density in a plasma, which means it must be effective at transferring momentum between electrons and ions. If the ions do not have time to respond to the wave electric field of a high frequency instability, regardless of the effects on the electron distribution, it is unlikely that a resistivity will be generated[6]. For this reason, along with observations [YAMADA *et al.*, 2000] of current sheet thicknesses on the order of the ion gyroradius, lower hybrid frequency range instabilities are of particular interest.

The lower hybrid drift instability (LDHI) [DAVIDSON *et al.*, 1977, and references therein] has been invoked often to explain resistivity in current sheets [HUBA *et al.*, 1977] (Chapter 2 of this dissertation will present a detailed review of the LHDI). However, the instability is linearly stabilized by large plasma beta [DAVIDSON *et al.*, 1977], and would be expected to be restricted to the edge of high beta current

[5] Both the Buneman and ion acoustic instabilities would be appropriate only in the case of a field aligned current (with a guide field) but some have argued they can operate in the field free region at the null in the zero guide field case.

[6] Electron instabilities may generate viscosity and hyperresistivity, which could be important at small scales (such as $c/\omega_{p,e}$ or ρ_e), and which could possibly play a role in fast reconnection.

sheets. This may limit its effectiveness as a mechanism for generating resistivity, as dissipation is needed at the center of the current sheet to break the frozen-in condition. Still, the instability is considered by some to be the "best bet" for generating anomalous resistivity in current sheets [SHINOHARA *et al.*, 1998], with the expectation that some mechanism (perhaps non-linear) will allow its penetration into regions of high-beta. There is some observational evidence for the presence of the LHDI in the magnetotail current sheet [HUBA *et al.*, 1978; SHINOHARA *et al.*, 1998], however it has not before been observed in laboratory reconnection experiments. Recent three-dimensional particle simulations of magnetic reconnection have shown that LHDI turbulence does develop in the current sheet [HORIUCHI and SATO, 1999] and could play a crucial role in reconnection, either through assisting in electric field penetration or through modifying the current sheet profile and driving new instabilities. As a result of profile modification by the LHDI, these simulations saw the drift-kink instability (DKI) develop and generate significant anomalous resistivity. The DKI [ZHU and WINGLEE, 1996] is a long-wavelength ($k\rho_i \sim 1$) instability whose real frequency and growth rate are comparable to the ion cyclotron frequency. This instability has been frequently invoked as a mechanism for current sheet disruption and substorm onset in the magnetotail[7] [YOON *et al.*, 1994]. However, the instability was discovered in low-mass ratio kinetic simulations, and there is a controversy over the effectiveness of this instability at realistic mass ratios [DAUGHTON, 1999].

For anomalous resistivity to explain observed reconnection rates, turbulence must develop in the current sheet, whether it be provided by LHDI, DKI or some unknown or unexpected instability. While significant progress can and has been

[7]The problem of onset of magnetic reconnection is not discussed here, but instabilities like the LHDI and DKI are thought to be of crucial importance in this problem.

made theoretically in understanding turbulence in current sheets, experimental data on the nature and role of turbulence during magnetic reconnection is crucial.

1.2.2 Laminar Hall-dominated reconnection

Recently, two-dimensional simulations of reconnection have revealed that the addition of non-dissipative terms in the generalized Ohm's law, specifically the Hall term, can lead to laminar fast reconnection [BIRN *et al.*, 2001]. The Hall term in Equation 1.3 becomes important on scales of order $c/\omega_{p,i}$, a scale which is observed in current sheets in the laboratory and in space [YAMADA *et al.*, 2000]. The mechanism behind fast reconnection in this model has been described by invoking the dispersive nature of the whistler wave, which is introduced with the Hall term[8]. On scales less than $c/\omega_{p,i}$, the primary normal mode of magnetic field oscillations in the fluid plasma is no longer the Alfvén wave, but is instead the whistler wave. When a field line is reconnected, it is expected to be in a tensed state (i.e. with significant, unsupported curvature; see the reconnected field line in the outflow of the current sheet in Figure 1.3). In an MHD plasma, the relaxation of the tensed field line is governed by the Alfvén wave, and this results in a standing Alfvén wave in the outflow region of the Sweet-Parker model (represented by the Alfvénic outflow). Inside a current sheet where the Hall term is active, the relaxation of reconnected field lines is instead governed by the dispersive whistler wave, and a standing whistler wave is seen in the outflow region of simulations where the Hall term is included [SHAY *et al.*, 1998]. An important difference between the Alfvén

[8]There is currently a great deal of confusion in the community over the use of "whistler wave physics" to describe reconnection in these simulations. Some have misunderstood this comment to mean that unstable whistler waves are creating an anomalous resistivity. In fact, these (2D) simulations are generally laminar, and any fluctuations that are generated are unimportant.

wave and the whistler wave is that the whistler has a phase velocity which depends on the scale of the wave. This property can result in an "opening-up" of the outflow region by the standing whistler wave, into a more "X"-like configuration. This is due to the fact that the whistler velocity actually decreases in the outflow direction, resulting in the need for the area of the outflow region to increase along the direction of outflow in order for mass conservation to be satisfied. This results in a reconnection geometry that is low aspect ratio, quite similar to the Petschek model. Dissipation in these simulations can be provided by collisionless mechanisms such as electron inertia through the formation of a small scale ($\gtrsim c/\omega_{p,e}$) electron current sheet, embedded in an ion current sheet which has $\delta_i \sim c/\omega_{p,i}$. The rate of reconnection is found to be independent of the choice of dissipation mechanism, and hence independent of the size of the electron current layer.

A large majority of the simulations done supporting the Hall-dominated picture of reconnection have been done in two-dimensions, artificially suppressing instabilities which grow as perturbations in the current direction. If turbulence were allowed to develop, it is possible that turbulent dissipation could dominate in the current sheet and become more important than the Hall mechanism described above. However, initial three dimensional Hall MHD simulations have shown that while turbulence does develop, no anomalous resistivity is generated, and the rate of reconnection is still controlled by effects associated with the Hall term [ROGERS *et al.*, 2000]. The LHDI is seen in these simulations, but seems to result in a slowing down of the reconnection process relative to the laminar two-dimensional case. Further three-dimensional simulations, particularly particle simulations, are needed in order to confirm these initial claims that reconnection may actually be slowed by turbulence. There is an obvious controversy over the role of turbulence

in current sheets which is presented by the Hall model and the anomalous resistivity model of magnetic reconnection. Experimental studies are critical in resolving this controversy and exposing the role of turbulence in magnetic reconnection.

1.3 Reconnection Experiments

The work reported in this dissertation is primarily experimental, and was performed using the Magnetic Reconnection Experiment (MRX) [YAMADA *et al.*, 1997a] (see Chapter 3 for a more detailed discussion of the experimental apparatus). In this section, a review of results which motivate the study of turbulence in MRX will be given, followed by a review of previous experimental studies of fluctuations in laboratory reconnection experiments.

1.3.1 Observations in MRX which motivate the study of turbulence

Collisionality in MRX current sheets is characterized by the parameter $\lambda_{\mathrm{mfp}}/\delta$, where δ is the width of the current sheet and λ_{mfp} is the electron mean free path against Coulomb collisions. Two observations which motivate the study of turbulence have been made as the collisionality was lowered ($\lambda_{\mathrm{mfp}}/\delta$ is increased) in MRX. The first observation is that the measured toroidal reconnection electric field, E_θ, is no longer balanced by classical collisional drag at the center of the current sheet, $E_\theta/\eta_{\mathrm{sp}} j_\theta \gg 1$, where η_{sp} is the classical Spitzer perpendicular resistivity. Figure 1.5 shows the measured ratio of the reconnection electric field to the classical resistive term in Ohm's law, ηj, measured at the center of the current sheet. If the ratio E/j is defined as an effective resistivity, $\eta^* = E/j$, reconnection data from

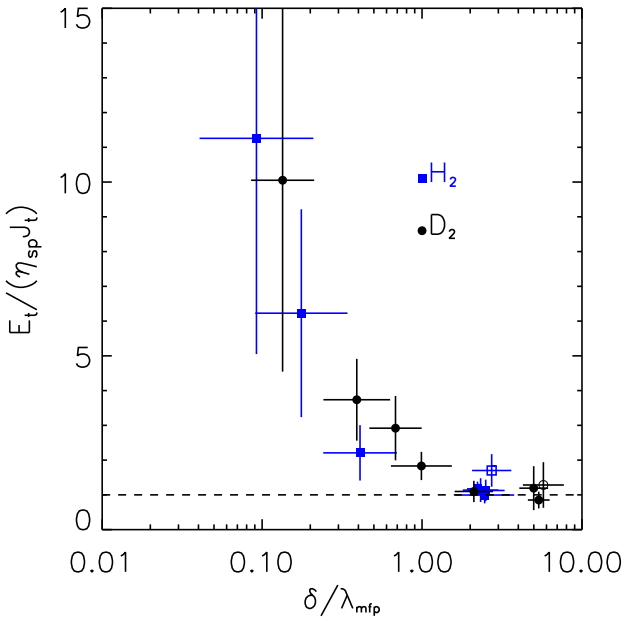

Figure 1.5: Ratio of reconnection electric field to the classical resistive term in Ohm's law versus collisionality in MRX. [TRINTCHOUK *et al.*, 2001]

MRX is found to agree with a generalized Sweet-Parker theory based on this effective resistivity (and also including compressibility and downstream pressure)[JI *et al.*, 1998], as shown in Figure 1.6.

The second observation is that of direct, nonclassical ion heating during reconnection in MRX current sheets [HSU *et al.*, 2000]. Figure 1.7(a) shows a spectroscopic measurement of ion temperature in helium discharges in MRX which demonstrates that ions are heated during the reconnection process in MRX. Figure 1.7(b) shows a comparison between the total heating energy input to the ions during reconnection and the measured effective resistivity, η^*. This figure shows that the fraction of the reconnected field energy going to the ions increases as collisionality is lowered (as η^* increases). One possible explanation for these two observations is the presence of turbulence in low-collisionality MRX current sheets,

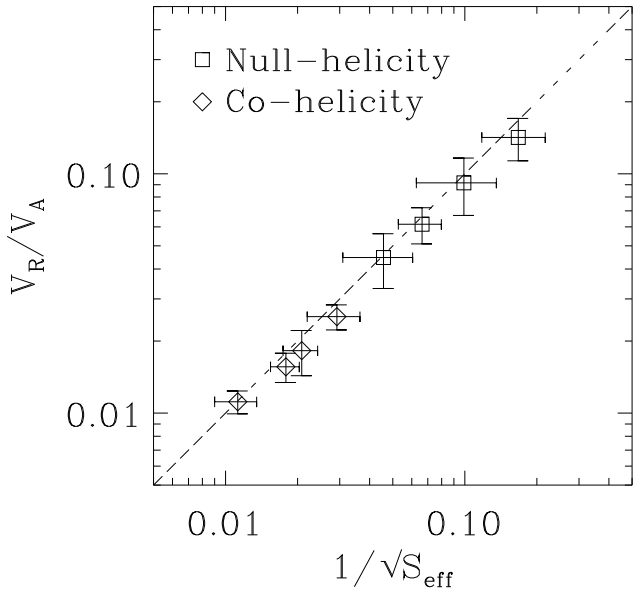

Figure 1.6: Comparison of MRX data with the Sweet-Parker model, generalized to include a measured effective resistivity [JI *et al.*, 1998].

which creates a turbulent anomalous resistivity $\eta^* > \eta_{sp}$ (so that $E_\theta/\eta^* j_\theta = 1$) and directly heats the ions.

Another observation which motivates the study of turbulence in MRX is the observation of the thickness of the current sheet, δ, scaling as $c/\omega_{p,i}$ or ρ_i (the two scales are comparable due to an average beta value of unity in MRX current sheets). Figure 1.8(a) shows the measured current sheet thickness versus $c/\omega_{p,i}$ from MRX discharges with widely varying conditions (central density, reconnecting magnetic field, etc). At the same time, measurements show that the average drift speed in the current sheet (defined as $V_d = j/ne$) is fairly constant over a wide range of conditions, and is roughly three or four times the ion thermal velocity (see Figure 1.8(b)). These two observations might suggest that a current-driven instability is operative in the MRX current sheet, whose marginal state limits the drift speed

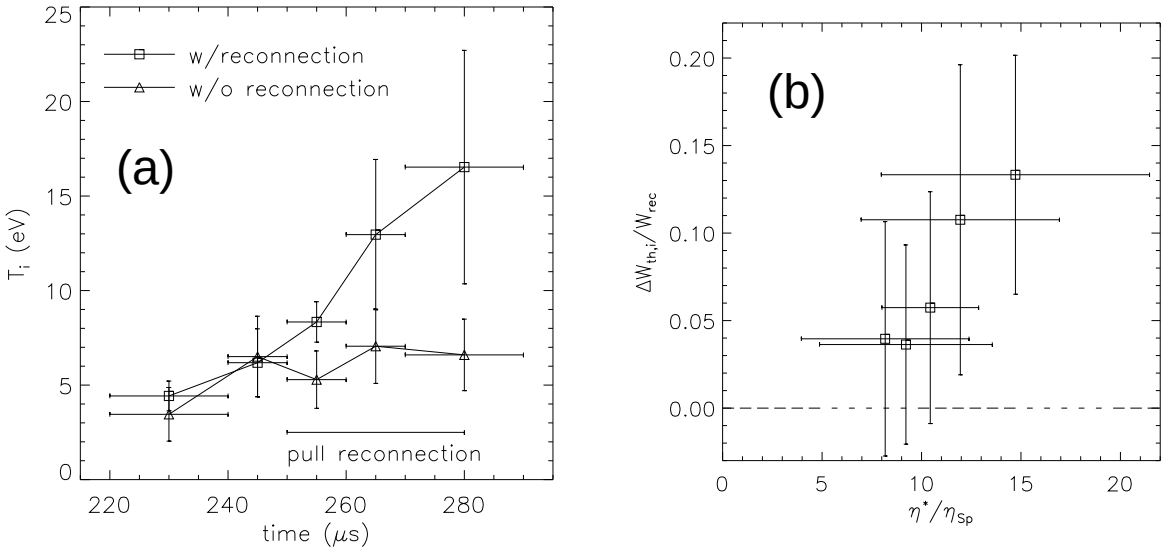

Figure 1.7: (a) Demonstration that ions are heated during the reconnection process in MRX. (b) Relationship between the fraction of the magnetic energy transferred to the ions and the resistivity enhancement, η^* [HSU *et al.*, 2000].

and sets the thickness of the current sheet. It should also be noted that this observation is consistent with the Hall dominated models of reconnection, which do not need turbulence for this scale length to develop in the current sheet.

1.3.2 Prior experimental studies of fluctuations in laboratory current sheets

There have been very few previous experimental studies of fluctuations in a laboratory current sheet, and none that have been done in an experiment in which the MHD approximation is satisfied in the bulk of the plasma ($S \gg 1$, $\rho_i \ll L$).

BAUM and BRATENAHL [1974] studied electrostatic fluctuations at the null point of a double-inverse pinch device. These experiments revealed fluctuations whose

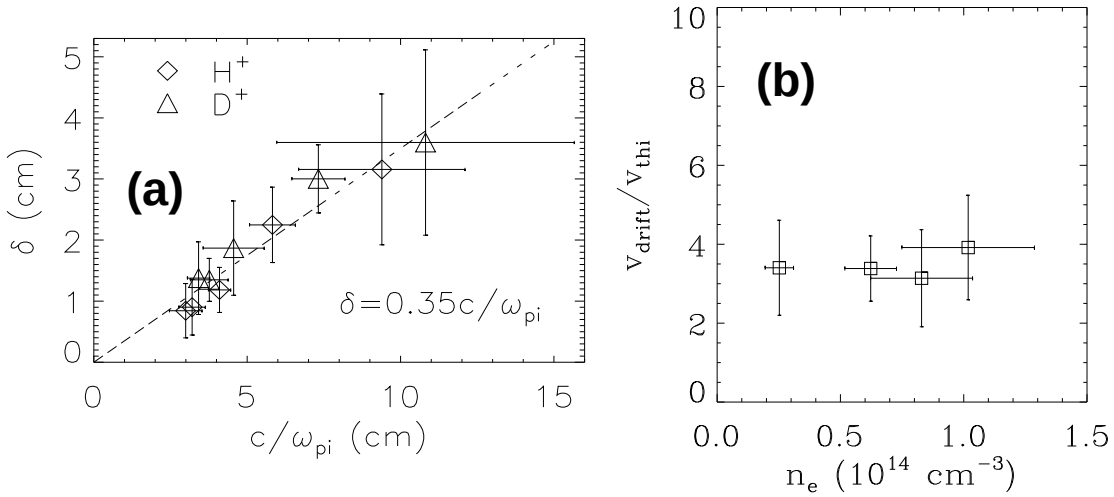

Figure 1.8: (a) Current sheet thickness in MRX. (b) Drift speed in the current layer of MRX [YAMADA *et al.*, 2000; JI *et al.*, 1998].

spectra were consistent with the presence of ion acoustic turbulence at the magnetic null. Anomalous resistivity had previously been observed in these experiments, and it was suggested, but not experimentally demonstrated, that the ion acoustic fluctuations were responsible. For several reasons these experiments are of limited relevance to current sheets and magnetic reconnection in nature. The ions in this experiment were not magnetically confined, as the ion gyroradius was larger than the apparatus size. The Lundquist number in these experiments was also quite low $S \lesssim 1$ and the discharge was quite short ($\tau \lesssim 10\mu s$) and difficult to adequately diagnose.

GEKELMAN and STENZEL [1984] studied magnetic and electrostatic fluctuations in a current sheet in a well-diagnosed reconnection experiment in linear geometry. Measurements of magnetic fluctuations revealed the presence of large amplitude whistler waves propagating along the reconnecting magnetic field. In addition, Langmuir probe and microwave measurements showed evidence for ion acoustic and Langmuir turbulence in the current sheet. Electron distribution

functions were measured in the current sheet and it was demonstrated that wave-particle interactions with these fluctuations were affecting the electron distribution function [GEKELMAN and STENZEL, 1985]. Anomalous resistivity was observed in these experiments, but no definitive tie to the measured fluctuations was made. These experiments were also done in a regime where the ions were unmagnetized, even outside of the current sheet, ($\rho_i >$ device size) and in plasmas with low Lundquist number ($S \lesssim 10$).

1.4 Dissertation objectives

The primary focus of this dissertation was to study fluctuations in a laboratory current sheet which is undergoing magnetic reconnection. This type of study has not before been performed in a laboratory current sheet in a plasma where, in the bulk of the plasma, the MHD approximation is satisfied ($S \gg 1$, $\rho_i \ll L$). The main experimental goals were the following: (1) detection of fluctuations in plasma potential and magnetic field, if present; (2) characterization and identification of instabilities driving these fluctuations; and (3) determination of the role of the observed fluctuations, if any, in the reconnection process.

1.5 Summary and Outline

The work presented in this dissertation has led to the first observation of the lower-hybrid drift instability in a laboratory current sheet. Fluctuations observed on the edge of MRX current sheets were identified as lower-hybrid drift waves due to

their measured frequency spectrum, radial amplitude profile, and spatial correlation characteristics. This observation provided an opportunity to study in detail the role of turbulence in magnetic reconnection in the laboratory. Data and analyses from this study suggest that the presence of the LHDI is not essential in determining the reconnection rate in collisionless current sheets in MRX. This dissertation is divided into the following 5 chapters and 2 appendices:

Chapter 1 This chapter presents an introduction to the problem of magnetic reconnection in a conducting plasma, and to the importance of turbulence in this problem.

Chapter 2 In this chapter a review of the theory of the lower-hybrid drift instability is offered. A derivation of the local linear dispersion relation for the electrostatic LHDI is presented.

Chapter 3 The experimental apparatus used for this dissertation work is described, focusing on diagnostics used to make high-frequency measurements of fluctuations in potential and magnetic field.

Chapter 4 Experimental fluctuation measurements and analysis are presented for an observation of the lower-hybrid drift instability in a laboratory current sheet. Comparisons with the theoretical model derived in Chapter 2 are made, along with discussions of the role of the LHDI in magnetic reconnection in MRX.

Chapter 5 Conclusions from this experimental work are presented along with a discussion of the repercussions for reconnection in MRX and in other physical systems. Speculations on the nature of reconnection in MRX are offered

along with suggestions for future research, based on the data presented in this dissertation.

Appendix A A short calculation revealing the perturbation to magnetic fields in the experiment by a small ferrite core transformer used in buffer amplifiers at the tip of fluctuation probes.

Appendix B A presentation of magnetic fluctuations other than lower-hybrid drift waves which were observed. The possible sources of these fluctuations and the effects the fluctuations may have on the current sheet and the reconnection process are discussed.

Chapter 2

Review of the Lower Hybrid Drift Instability

THE LOWER-HYBRID DRIFT INSTABILITY has been studied theoretically for decades, motivated by its possible role in magnetic reconnection [HUBA *et al.*, 1977], theta-pinches and other fusion devices [KRALL and LIEWER, 1971], and space plasmas (e.g. the magnetosphere [YOON *et al.*, 1994]). In this chapter, a review of the theory and prior experimental studies of this instability is presented. In Section 2.1 reviews the theory of the LHDI, including the derivation and discussion of a local, linear, electrostatic model of the LHDI. This model will be utilized to explain features of the experimental data in Chapter 4. Section 2.2 briefly discusses prior observational studies of the LHDI.

2.1 Theory of the LHDI

The first studies of the lower-hybrid drift instability (LHDI) were made by KRALL and LIEWER [1971], who were motivated by the observation of anomalously large shock widths in theta-pinch experiments. The theta-pinch configuration, like many magnetic confinement configurations, involves gradients of plasma pressure which are supported by gradients in the magnetic field strength. The scale lengths of the experimentally observed gradients in theta-pinches were such that the ions could be treated as unmagnetized in the instability theory. The same situation exists in current sheets associated with magnetic reconnection; the measured thickness of the current sheet in the MRX experiment is on the order of the ion gyroradius (based on the peak field in the current sheet) [YAMADA *et al.*, 2000]. The free energy sources which drive the LHDI are density gradients and cross-field currents. Cross-field currents are due in part to the diamagnetic currents arising from the density gradient, but there can also be current due to $E \times B$ electron flows in the current sheet, as the ions are unmagnetized and should not develop $E \times B$ flows in response to transverse electric fields. An electrostatic, linear analysis of these plasma profiles reveals the LHDI, an instability with real frequency $\omega \sim \omega_{LH}$ ($\omega_{LH} \sim \sqrt{\Omega_e \Omega_i}$) and wavenumber at peak growth $k\rho_e \sim 1$. The growth rate of the LHDI can be quite strong, with $\gamma \sim \omega_{LH}$, even in cases where the ion temperature far exceeds the electron temperature. DAVIDSON *et al.* [1977] and HUBA and WU [1976] studied the influence of finite plasma beta ($\beta = 8\pi p/B^2$) on the growth rate of the LHDI. These studies showed that large beta provided a stabilizing influence in the electrostatic model, through the effect of ∇B drifts on electron orbits. This stabilization is of great importance for the impact of the LHDI on the process

of magnetic reconnection, as high plasma beta is found near the center of current sheets, where anomalous resistivity would be needed to speed up Sweet-Parker reconnection.

2.1.1 Derivation of local, electrostatic LHDI model

In order to gain further understanding of the LHDI and to develop a model to be used to compare with data taken on the MRX experiment, we present a derivation of a local, linear, electrostatic theory of the instability. The following closely follows the procedures used by KRALL and ROSENBLUTH [1962], DAVIDSON *et al.* [1977], and HUBA and WU [1976] in deriving the dispersion relation for the lower-hybrid drift instability. We consider a local model of the current sheet, assuming that the wavelength of the mode of interest is much smaller than the gradient scale length in the plasma, $\lambda \ll (d \ln n/dx)^{-1}$, $(d \ln B/dx)^{-1}$. We therefore use a slab model in the derivation, and the geometry[1] of our model current sheet is shown in Figure 2.1(a). Figure 2.1(b) shows a drift wave operating in the model geometry with k in the y direction: oscillating electric fields in the y direction create density fluctuations through inducing $E \times B$ flows in the gradient direction. This simple drift wave picture is modified in two ways in the LHDI derivation. First, the ions and electrons are drifting across the field, providing an additional energy source (aside from the density gradient) to drive the wave unstable. Second, the ions are unmagnetized, as the density gradient scale length is comparable to the ion gyroradius, and their response should therefore be primarily a polarization response rather than $E \times B$. We will include these effects in the following derivation.

We treat the ions as unmagnetized, and flowing across the field with velocity V.

[1] To translate model coordinates to MRX coordinates, $x \rightarrow r$, $y \rightarrow \theta$.

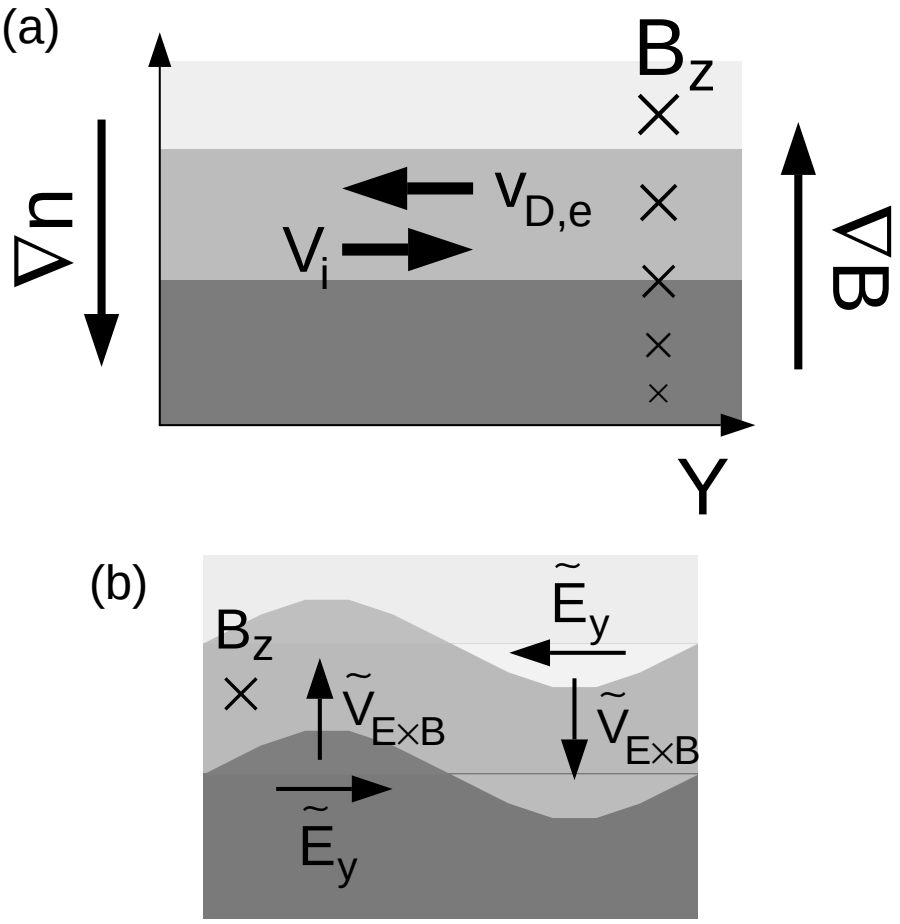

Figure 2.1: (a) Model geometry for LHDI derivation. The magnetic field is in the z direction, and the density and field vary in the x direction. (b) Simple drift wave in this geometry, with $\tilde{E}$ primarily in the current direction (y).

The derivation will take place in the frame where the electric field is zero, and the ion flow velocity, V, therefore represents both the ion diamagnetic drift speed and any $E \times B$ electron current. The equilibrium ion distribution function is chosen to be a shifted Maxwellian:

$$f_{\mathrm{i}}^{0} = \frac{n}{\pi^{3/2} v_{\mathrm{th,i}}^{3}} \exp\left(-\frac{v_{\mathrm{x}}^{2} + (v_{\mathrm{y}} - V)^{2} + v_{\mathrm{z}}^{2}}{v_{\mathrm{th,i}}^{2}} \right)$$

Where $v_{\mathrm{th,i}} = \sqrt{2T_{\mathrm{i}}/M}$ and n are evaluated locally. The electrons are magnetized, and we write the equilibrium distribution function as a function of the constants of the electron motion: v^2, p_z, and $p_y = mv_y - eA_y(x)/c$. If we assume that the gradient in the magnetic field is weak, we can approximate $p_y \approx mv_y - eB_{\mathrm{o}}x/c$. The electron distribution function is chosen to be:

$$f_{\mathrm{e}}^{0} = \frac{n(X)}{\pi^{3/2} v_{\mathrm{th,e}}^{3}} \exp\left(-\frac{v_{\perp}^{2} + v_{\mathrm{z}}^{2}}{v_{\mathrm{th,e}}^{2}} \right)$$

Where X is related to the canonical momentum in the y direction, $X = x - v_y/\Omega_{\mathrm{e}} = -(eB/c)p_y$. We choose a local model and expand about $x = 0$ to find:

$$f_{\mathrm{e}}^{0} \approx \left(1 - \epsilon_{\mathrm{n}} \frac{v_y}{\Omega_{\mathrm{e}}} \right) F_{\mathrm{m,e}}$$

Where $\epsilon_{\mathrm{n}} = d \ln n/dx$ and $F_{\mathrm{m,e}}$ is a Maxwellian electron distribution.

In the following we use the electrostatic approximation and introduce $k_{\perp} = \sqrt{k_x^2 + k_y^2}$ and $k_{\parallel} = k_z$. The Vlasov equation is used to calculate perturbed distribution functions, from which the perturbed charge densities are calculated and used in Poisson's equation.

$$\left(\frac{d\delta f_{\mathrm{e}}}{dt} \right)_{0} = -\frac{q}{m} \mathbf{E} \cdot \frac{\partial f_{\mathrm{e}}^{0}}{\partial \mathbf{v}}$$

We use the method of characteristics to solve for δf_{e}, integrating along the zero-order orbits of the particles:

$$\delta f_{\mathrm{e}} = -\frac{q}{m} \int_{-\infty}^{t} dt' \left(\mathbf{E} \cdot \frac{\partial}{\partial \mathbf{v}} f_{\mathrm{e}}^{0} \right)_{v',r',t'}$$

$$
\begin{aligned}
&= \frac{q}{m}\int_{-\infty}^{t} dt' \left[-\mathbf{v}\cdot\nabla\phi \frac{2F_{\mathrm{m,e}}}{v_{\mathrm{th,e}}^2} + \frac{\epsilon_{\mathrm{n}}}{\Omega_{\mathrm{e}}} F_{\mathrm{m,e}} \left(\nabla\phi\right)_y \right] \\
&= -\frac{2q}{m}\frac{F_{\mathrm{m,e}}}{v_{\mathrm{th,e}}^2}\phi_{t'=t} + \frac{2q}{m}\frac{F_{\mathrm{m,e}}}{v_{\mathrm{th,e}}^2}\int_{-\infty}^{t} dt' \frac{\partial\phi}{\partial t'} + \frac{ik_y q\epsilon_{\mathrm{n}}}{m\Omega_{\mathrm{e}}} F_{\mathrm{m,e}} \int_{-\infty}^{t} dt'\phi
\end{aligned}
$$

The final step is accomplished by using $\mathbf{v}\cdot\nabla\phi = d\phi/dt - \partial\phi/\partial t$, and by assuming $\phi_{t'\to-\infty} = 0$.

In order to complete the time integrals, we must first solve the single particle equations of motion for the electrons. These are:

$$
\frac{d\mathbf{v}}{dt} = \frac{q}{m_{\mathrm{e}}}\frac{\mathbf{v}\times\mathbf{B}(x)}{c}
$$

$$
\frac{d\mathbf{r}}{dt} = \mathbf{v}
$$

Assuming that the gradient scale length in the magnetic field is much longer than the electron gyroradius, we can use the guiding center expansion to obtain the electron orbit. Introducing the variable $\tau = t' - t$, we find:

$$
\begin{aligned}
y' &\approx \frac{v_\perp}{\Omega_{\mathrm{e}}}\cos\left(\varphi+\Omega_{\mathrm{e}}\tau\right) - \frac{v_\perp}{\Omega_{\mathrm{e}}}\cos\varphi - \frac{1}{2}\epsilon_{\mathrm{b}}\frac{v_\perp^2}{\Omega_{\mathrm{e}}}\tau \\
x' &\approx \frac{v_\perp}{\Omega_{\mathrm{e}}}\sin\left(\varphi+\Omega_{\mathrm{e}}\tau\right) - \frac{v_\perp}{\Omega_{\mathrm{e}}}\sin\varphi \\
z' &= -v_\parallel\tau
\end{aligned}
$$

Where $\epsilon_{\mathrm{b}} = (1/B)\partial B/\partial x$ and $\epsilon_{\mathrm{b}} v_\perp^2/2\Omega_{\mathrm{e}} = V_{\nabla\mathrm{B}}$, the electron ∇B drift speed. Here we are ignoring oscillating terms of order $\epsilon_{\mathrm{b}} v_\perp^2/\Omega_{\mathrm{e}}$. If we assume $\phi = \tilde{\phi}\exp(i\mathbf{k}\cdot\mathbf{r} - i\omega t)$, then the equation for δf_{e} becomes:

$$
\begin{aligned}
\delta f_{\mathrm{e}} &= -\frac{2q}{m}\frac{F_{\mathrm{m,e}}}{v_{\mathrm{th,e}}^2}\left[\tilde{\phi} + i(\omega - k_y v_{\mathrm{D,e}})\tilde{\phi}\times\right. \\
&\qquad \left.\int_0^\infty d\tau \exp\left(-i\left(\frac{k_\perp v_\perp}{\Omega_{\mathrm{e}}}(\cos(\varphi+\Omega_{\mathrm{e}}\tau) - \cos\varphi)\right) + (\omega - k_\parallel v_\parallel - k_y V_{\nabla\mathrm{B}})\tau\right)\right]
\end{aligned}
$$

Using the fact that

$$
\exp(iz\sin\varphi) = \sum_{n=-\infty}^{\infty}\exp(in\varphi)J_n(z)
$$

and

$$\exp(iz\sin(\varphi+\Omega_{\rm e}\tau))=\sum_{n=-\infty}^{\infty}\exp(im(\varphi+\Omega_{\rm e}\tau))J_n(z),$$

$\delta f_{\rm e}$ becomes:

$$\delta f_{\rm e}=-\frac{2q}{m}\frac{F_{\rm m,e}}{v_{\rm th,e}^2}\tilde{\phi}\left[1-(\omega-k_y v_{\rm D,e})\sum_{n,m}\left(\frac{J_n(z)J_m(z)\exp(i(m-n)(\varphi-\pi/2))}{\omega-k_\parallel v_\parallel-k_y V_{\nabla \rm B}-m\Omega_{\rm e}}\right)\right]$$

Where we have introduced the electron diamagnetic velocity, $v_{\rm D,e}=\epsilon_{\rm n}v_{\rm th,e}^2/2\Omega_{\rm e}$ and $z=k_\perp v_\perp/\Omega_{\rm e}$. The perturbed electron density can now be calculated by integrating $\delta f_{\rm e}$ over velocity space.

$$\begin{aligned}\delta n_{\rm e} &= -\frac{2qn_{\rm o}}{mv_{\rm th,e}^2}\tilde{\phi}-\frac{2q}{mv_{\rm th,e}^2}\tilde{\phi}(\omega-k_y v_{\rm D,e})\times\\ &\sum_{m,n}\int v_\perp dv_\perp\int dv_\parallel\frac{J_n(z)J_m(z)F_{\rm m,e}}{\omega-k_\parallel v_\parallel-k_y V_{\nabla \rm B}-m\Omega_{\rm e}}\int d\varphi\exp(i(m-n)(\varphi-\pi/2))\end{aligned}$$

The velocity phase integral is nonzero only for $m=n$. The integral over $v_\parallel$ evaluates to a plasma dispersion function, Z:

$$Z(\xi)=\frac{1}{\sqrt{\pi}}\int_{-\infty}^{\infty}dz\frac{\exp(-z^2)}{z-\xi}$$

The perturbed electron density then becomes:

$$\begin{aligned}\delta n_{\rm e} &= -\frac{2qn_{\rm o}}{mv_{\rm th,e}^2}\tilde{\phi}-\frac{2qn_{\rm o}}{mv_{\rm th,e}^2}\tilde{\phi}(\omega-k_y v_{\rm D,e})\frac{2}{k_\parallel v_{\rm th,e}}\times\\ &\sum_n\int xdx\exp(-x^2)J_n^2(k_\perp\rho_{\rm e}x)Z\left(\frac{\omega-k_y\bar{V}_{\nabla \rm B}x^2-n\Omega_{\rm e}}{k_\parallel v_{\rm th,e}}\right)\end{aligned}$$

Where we have introduced $x=v_\perp/v_{\rm th,e}$, and $\bar{V}_{\nabla \rm B}=\epsilon_{\rm b}v_{\rm th,e}^2/2\Omega_{\rm e}$. The frequency range of interest for the LHDI is $\omega\sim\omega_{\rm LH}\ll\Omega_{\rm e}$, and we will therefore keep only the $n=0$ term in the sum. So the final expression for the perturbed electron density is then:

$$\begin{aligned}\delta n_{\rm e} &= -\frac{2qn_{\rm o}}{mv_{\rm th,e}^2}\tilde{\phi}-\\ &\frac{2qn_{\rm o}}{mv_{\rm th,e}^2}\tilde{\phi}(\omega-k_y v_{\rm D,e})\frac{2}{k_\parallel v_{\rm th,e}}\int xdx\exp(-x^2)J_0^2(k_\perp\rho_{\rm e}x)Z\left(\frac{\omega-k_y\bar{V}_{\nabla \rm B}x^2}{k_\parallel v_{\rm th,e}}\right)\end{aligned}\tag{2.1}$$

The perturbed ion density is straightforward to calculate in the limit of unmagnetized, drifting ions, yielding [STIX, 1992]:

$$\delta n_{\mathrm{i}} = \frac{2qn_{\mathrm{o}}}{Mv_{\mathrm{th,i}}}\tilde{\phi}\left[1+\zeta_{\mathrm{i}}\mathrm{Z}(\zeta_{\mathrm{i}})\right] \tag{2.2}$$

Where $\zeta_{\mathrm{i}} = (\omega - k_{\mathrm{y}}V)/kv_{\mathrm{th,i}}$. We can then use Poisson's equation to relate the density perturbations to the potential perturbation:

$$\begin{aligned} -k^2\phi &= 4\pi e(\delta n_{\mathrm{i}} - \delta n_{\mathrm{e}}) \\ &= \phi\left\{-\frac{1}{2\lambda_{\mathrm{d,i}}^2}\mathrm{Z}'(\zeta_{\mathrm{i}}) + \frac{1}{\lambda_{\mathrm{d,e}}^2}\left(1+\frac{2(\omega-k_y v_{\mathrm{D,e}})}{k_{\parallel}v_{\mathrm{th,e}}}\times\right.\right. \\ &\quad \left.\left.\int x dx \exp(-x^2)J_0^2(k_{\perp}\rho_{\mathrm{e}}x)\mathrm{Z}\left(\frac{\omega-k_y\bar{V}_{\nabla\mathrm{B}}x^2}{k_{\parallel}v_{\mathrm{th,e}}}\right)\right)\right\} \end{aligned}$$

The dispersion relation can then be obtained from roots of the following expression:

$$\begin{aligned} 0 &= 1 - \frac{1}{2k^2\lambda_{\mathrm{d,i}}^2}\mathrm{Z}'(\zeta_{\mathrm{i}}) + \frac{1}{k^2\lambda_{\mathrm{d,e}}^2}(1+\psi) \\ \psi &= \frac{2(\omega-k_y v_{\mathrm{D,e}})}{k_{\parallel}v_{\mathrm{th,e}}} \times \int x dx \exp(-x^2)J_0^2(k_{\perp}\rho_{\mathrm{e}}x)\mathrm{Z}\left(\frac{\omega-k_y\bar{V}_{\nabla\mathrm{B}}x^2}{k_{\parallel}v_{\mathrm{th,e}}}\right) \end{aligned} \tag{2.3}$$

The value of the electron ∇B drift velocity can be shown to depend on the value of the total plasma beta. If we assume equilibrium between the magnetic and plasma pressure, and also that the temperature is spatially uniform, we find:

$$\begin{aligned} \nabla\left(\frac{B^2}{8\pi}\right) &= -\nabla p \\ \frac{2B^2}{8\pi}\frac{\partial \ln B}{\partial x} &= -n(T_{\mathrm{e}}+T_{\mathrm{i}})\frac{\partial \ln n}{\partial x} \\ \epsilon_{\mathrm{b}} &= -\frac{1}{2}\beta\epsilon_{\mathrm{n}} \\ \therefore \bar{V}_{\nabla B} &= -\frac{\beta}{2}v_{\mathrm{D,e}} \end{aligned}$$

Where β is the total plasma beta, $\beta = 8\pi n(T_e + T_i)/B^2$. Thus the plasma beta enters into equation 2.3 through the ∇B drift term in the plasma dispersion function.

Using equation 2.3, we can explore the linear characteristics of the LHDI using parameters relevant to the MRX experiment. The relevant dimensionless parameters in MRX are $\epsilon_n \rho_i/2 \sim 1$ (density gradient scale length is roughly $2\rho_i$), $V/v_{th,i} \sim 2.5$ ($j/ne - nev_{D,e} \sim 2.5 v_{th,i}$), and $T_i/T_e \sim 1$. Figure 2.2 shows the real frequency and growth rate as a function of normalized wavenumber, $k_\perp \rho_e$, for these parameters and for several values of the normalized parallel wavenumber, $k_\parallel/k_\perp \sqrt{M/m_e}$, for the case $\beta = 0$. The frequencies obtained from roots of equation 2.3 are Doppler shifted by $k_\perp V$ in this plot in order to show the frequency in the ion rest frame. The frequency in the electron rest frame is inset, for $k_\parallel = 0$. In the ion rest frame, positive real frequency is found for $k_\perp$ in the electron diamagnetic direction, indicating that the unstable waves propagate in that direction. The growth rate of the LHDI is found to be quite strong, and peaked near $k_\perp \rho_e \sim 1$ and $\omega \sim \omega_{LH}$. Significant growth is found at a wide range of $k_\perp \rho_e$, translating to a range of real frequencies up to two to three times the lower hybrid frequency. In the ion rest frame, the phase velocity of the waves at peak growth ($\omega \sim \omega_{LH}$, $k_\perp \rho_e \sim 1$) is:

$$\frac{\omega}{k_\perp} \sim \omega_{LH} \rho_e = \sqrt{\frac{T_e}{T_i}} v_{th,i}$$

Therefore the strongest growth is found where ion Landau damping of the waves is strongest. This actually drives growth of the LHDI, as it is a negative energy drift wave in the ion rest frame [DRAKE *et al.*, 1984]. For $k_\parallel = 0$, the growth rate of the waves is due to $-(\partial f_i^0/\partial v)_{\omega/k}$ and no damping is provided by the electrons (for $\beta = 0$). As $k_\parallel$ is acquired by the wave, access to electron Landau damping along the field line is provided, resulting in a lowering and eventual suppression

of the growth rate, at very small values of $k_\parallel/k_\perp$.

There is an additional instability mechanism which is available when $\epsilon_n = 0$ and $k_\parallel/k_\perp \sim \sqrt{m_e/M}$ in Eqn. 2.3. Near this value of $k_\parallel/k_\perp$, the electrons appear as heavier particles when their response is projected along k. A two-stream like instability can develop as a result of this scenario with ions streaming through effectively heavier electrons, which is called the modified two-stream instability (MTSI) [AREFEV, 1970; KRALL and LIEWER, 1971]. This instability has characteristics which are almost identical the LHDI, in that $\omega \sim \omega_{LH}$ and $k_\perp \rho_e \sim 1$, but is found in the case that the density gradient is zero yet the ion cross-field flow is finite. However, the growth rate of the MTSI is smaller than the LHDI when the density gradient is appreciable (i.e. in MRX current sheets). Figure 2.3(a) shows the $k_\parallel$ dependence of the peak growth rate for the same conditions as explored in Figure 2.2 along with the peak growth rate due to the MTSI, calculated by setting the density gradient to zero so that the LHDI is suppressed. While the MTSI growth rate is not necessarily insignificant in this figure, the growth rate for the finite-$k_\parallel$ LHDI dominates the MTSI growth rate. Figure 2.3(b) shows the growth rate for the two cases as a function of normalized perpendicular wavenumber for $k_\parallel/k_\perp\sqrt{M/m_e} = 0.55$ (at the peak of the MTSI growth). This figure demonstrates that the LHDI instability mechanism produces growth at a much wider range of wavenumbers than does the MTSI. So, while Eqn. 2.3 contains the physics describing both the MTSI and the LHDI, the dominant instability in conditions relevant to MRX should be the LHDI.

Figure 2.2 is for the case of zero plasma beta. Significant beta values are found in the MRX current sheet, from roughly 10%-100% at the edge to infinite local beta at the field null. Figure 2.4 shows the effect of increasing plasma beta on the peak

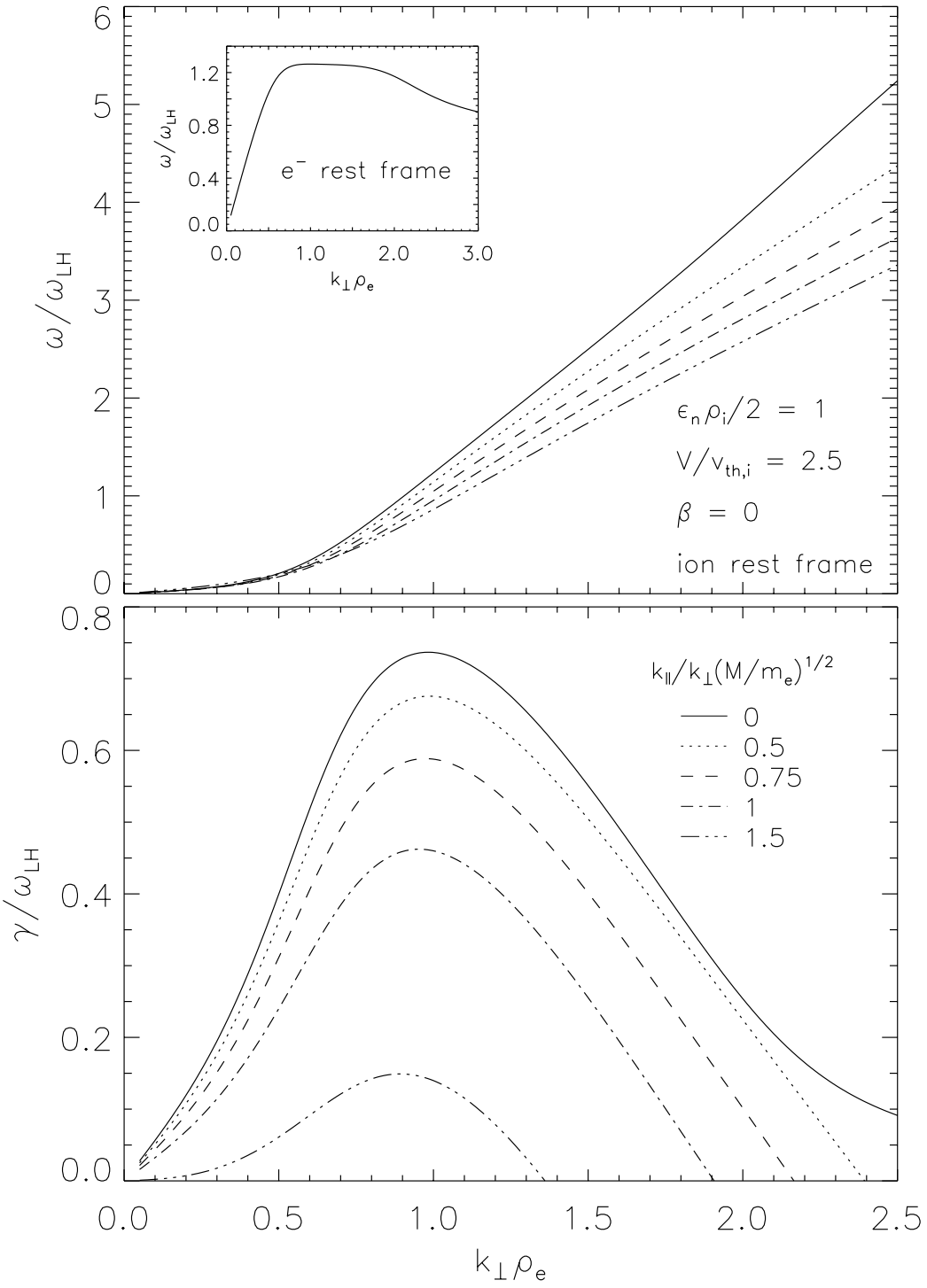

Figure 2.2: Real frequency and growth rates for the LHDI using parameters relevant to the MRX experiment. Inset to the real frequency plot is a plot of the frequency observed in the electron rest frame.

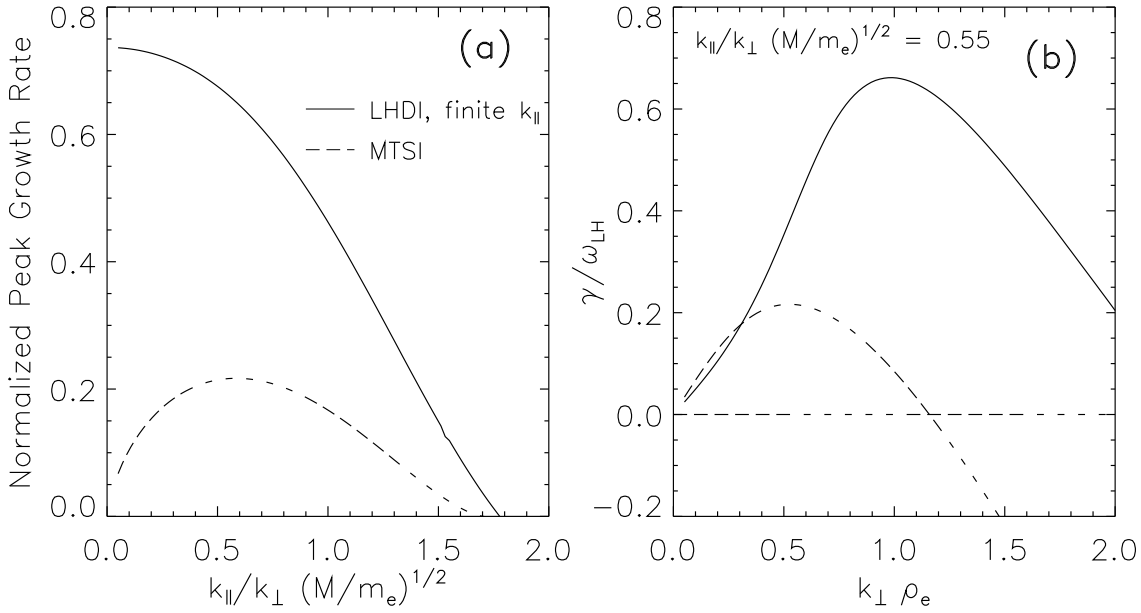

Figure 2.3: (a) The peak growth rate as a function of $k_{\|}$ with a density gradient and without (MTSI). (b) The growth rate as a function of $k_{\perp}$ without a density gradient (MTSI, dotted line) and with a density gradient (solid line, LHDI).

growth rate and wavenumber at peak growth for the LHDI under the same conditions in Figure 2.2 and for $k_{\|} = 0$. As beta is initially increased there is little change in the peak growth rate, but after $\beta \approx 1$, the peak growth rate drops dramatically. The wavenumber at peak growth is increased from $k_{\perp}\rho_e \sim 1$ to $k_{\perp}\rho_e \sim 2$ over the same range, indicating a shift to shorter normalized wavelength. Figure 2.5 shows the growth rate versus normalized perpendicular wavenumber for three values of beta, $\beta = 0, 1, 2$. As beta is raised, the growth rate for longer wavelength modes is reduced and eventually these modes are damped. The LHDI is stabilized as beta is raised by resonant effects of the electron ∇B drift, which becomes comparable to the electron diamagnetic drift speed as beta is raised to near unity. As the average ∇B drift speed is raised to be comparable to the phase speed of the waves, resonant interactions of the waves with drifting electrons (via the plasma dispersion

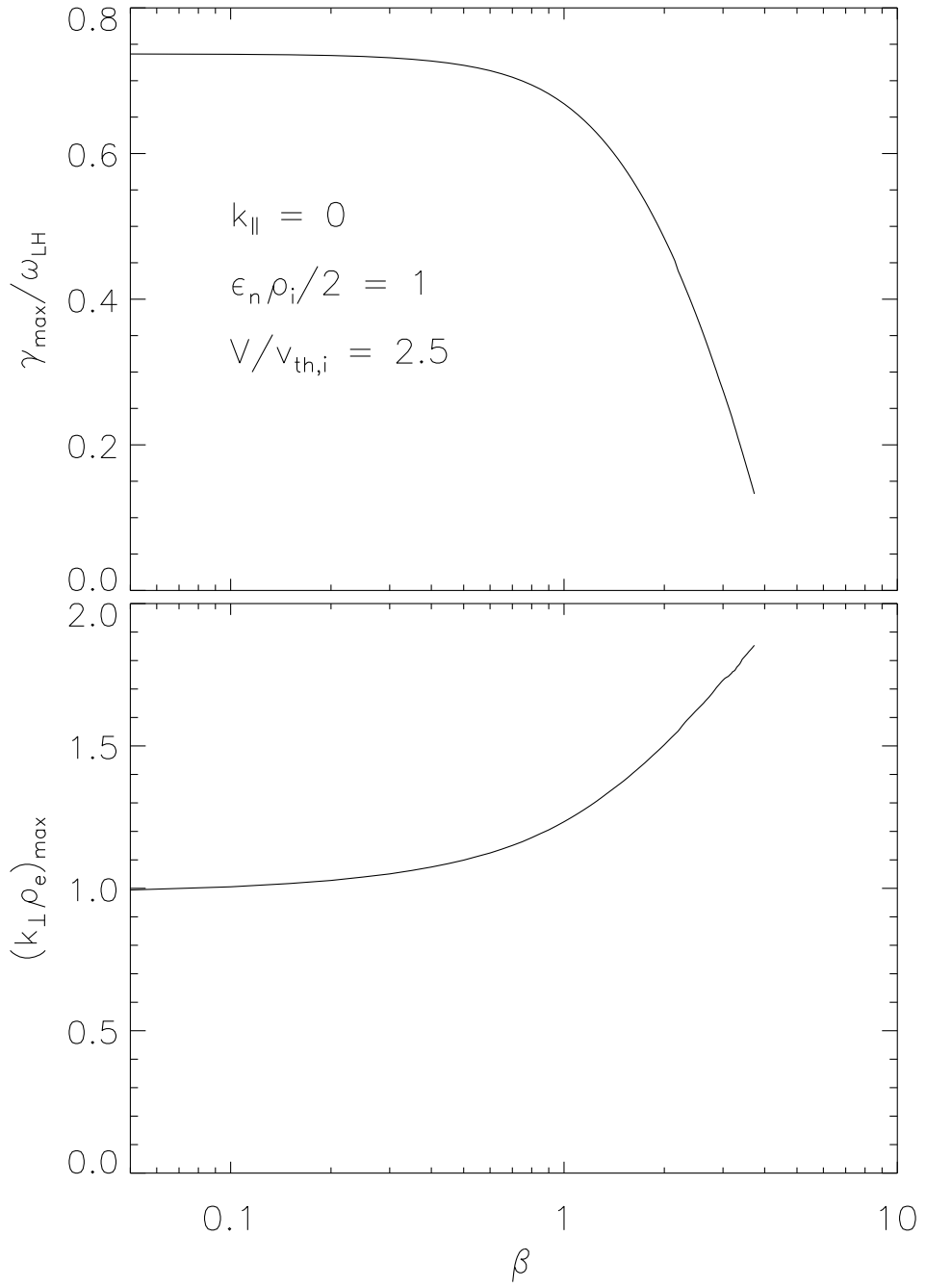

Figure 2.4: Peak growth rate and normalized wavenumber at peak growth for the LHDI as a function of beta.

function in ψ in Eqn. 2.3) leads to damping.

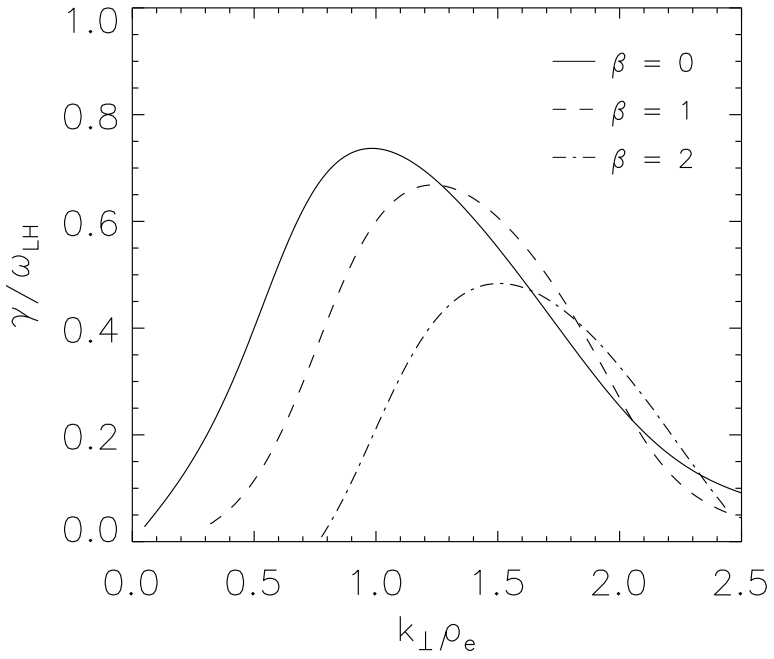

Figure 2.5: Growth rate as a function of perpendicular wavenumber for different values of beta.

The local, electrostatic, linear model of the LHDI presented in this section shows that we should expect the LHDI to be fairly strongly growing in conditions similar to those found in MRX, with $\gamma \sim \omega_{LH}$ at $k_\perp \rho_e \sim 1$. It is interesting to note that the marginal state of the LHDI is predicted to occur at significantly shallower density gradients than those observed in MRX. An estimate of the critical density gradient (assuming the cross-field current to be entirely diamagnetic) is $\rho_i \epsilon_n / 2 \sim 2\Omega_i \omega_{LH} \sim 1/20$ [DAVIDSON *et al.*, 1977]. The predicted LHDI growth rate drops dramatically as beta is raised, and the instability is likely to be suppressed in the center of the current sheet, where beta is locally infinite. In the remainder of this section, linear extensions to this model will be discussed, along with a review of nonlinear theory and simulations of the LHDI.

2.1.2 Electromagnetic effects

Electromagnetic corrections to the LHDI were first explored by DAVIDSON *et al.* [1977]. In this paper electrostatic and electromagnetic corrections due to large plasma beta were considered. The stabilizing effects of beta were found to be due to resonant ∇B effects, as found in the electrostatic model derived in this chapter, rather than due to electromagnetic effects. In fact, in regimes similar to those found in MRX ($V/v_{\mathrm{th,i}} \gtrsim 1$), electromagnetic effects were found to be *destabilizing*. These destabilizing effects were found to lead to the restoration of growth at longer wavelengths (small $k_\perp \rho_\mathrm{e}$ in Figure 2.5), but only increased the value of the peak growth rate slightly compared to the electrostatic case. Thus, the overall effect of beta is a stabilizing one, however the electrostatic model presented in this chapter slightly overestimates the degree of stabilization. For this reason, as well as for simplicity, the electrostatic model presented above, which captures the dominate finite-beta effect of resonant ∇B stabilization, is used instead of a fully electromagnetic theory to calculate peak growth rates for comparison with data presented in Chapter 4. For $k_\parallel = 0$, the electromagnetic LHDI is flute-like, only generating perturbations in the background magnetic field component (B_z in MRX).

Later work on electromagnetic corrections to the LHDI focused on including cases with finite $k_\parallel$. These studies brought renewed interest to the modified two-stream instability. Studies of electromagnetic corrections to the LHDI which included $k_\parallel$ found that the MTSI could couple to obliquely propagating whistler waves [WU *et al.*, 1983; CHOUEIRI *et al.*, 1991]. While these efforts were successful in connecting perpendicularly propagating electrostatic instabilities to nearly or fully parallel propagating electromagnetic waves, the growth rate difference between the $k_\parallel = 0$ LHDI and these modes was found to be large except in cases

of very large cross-field ion flow ($V/v_{\mathrm{th,i}} \gtrsim 10$) [Wu *et al.*, 1983; Choueiri *et al.*, 1991], which is not found in MRX.

2.1.3 Nonlinear effects and simulations

Saturation mechanisms

The anomalous transport properties of the LHDI have been of great interest in the theoretical literature, especially as applied to theta pinches [Davidson and Gladd, 1975] and magnetic reconnection [Huba *et al.*, 1978]. The starting point for estimates of transport coefficients is the determination of the saturation level of the LHDI. The earliest estimate of this level was done by Davidson [1978], where quasilinear theory was employed to determine the efficiency of saturation by plateau formation and current relaxation. The former is unlikely to be important in MRX plasmas, as collisions are likely to maintain Maxwellian particle distribution functions (this has been observed spectroscopically [Hsu *et al.*, 2001]). It has been pointed out [Drake *et al.*, 1984] that current relaxation does not provide a realistic bounds on the saturated amplitude, as the energy in the field is tied to the current, and this thermodynamic estimate should be based on the total magnetic energy in the system. Ion trapping was observed as the saturation mechanism for the LHDI in simulations by Winske and Liewer [1978]. This mechanism is effective when the LHDI spectrum is nearly monochromatic, as was observed in these simulations at moderate drift velocity $V/v_{\mathrm{th,i}} \gtrsim 3$. Huba and Papadopoulos [1978] considered the effect of electron resonance broadening on the saturation of the LHDI. In this study, the stabilizing electron ∇B resonance was shown to be nonlinearly broadened, allowing a larger population of electrons to interact with

and damp the LHDI waves. A saturation estimate for this process (however for $V/v_{\mathrm{th,i}} \lesssim 1$) was made by GARY [1980]:

$$\left(\frac{\mathcal{E}}{nT_\mathrm{i}}\right) \approx \frac{2}{5}\frac{m_\mathrm{e}}{M}\frac{\Omega_\mathrm{e}^2}{\omega_\mathrm{p,e}^2}\left(\frac{T_\mathrm{i}}{T_\mathrm{e}}\right)^{1/4}\frac{V^2}{v_\mathrm{th,i}^2} \tag{2.4}$$

However, this saturation mechanism, which is similar to electron trapping, might be hampered in MRX by high electron collisionality. Finally, a numerical calculation of the effect of nonlinear Landau damping (or mode-mode coupling) on the saturation of the LHDI was performed by DRAKE *et al.* [1984]. In this case, nonlinear transfer of energy from growing long wavelength modes ($k\rho_\mathrm{e} \sim 1$) to damped short wavelength modes provided a saturation mechanism. This calculation yielded an estimate for the saturation level of the LHDI:

$$\frac{e\phi}{T_\mathrm{i}} \approx 2.4\left(\frac{2m_\mathrm{e}}{M}\right)^{1/2}\frac{V}{v_\mathrm{th,i}} \tag{2.5}$$

This calculation ignored any nonlinear coupling into damped modes with finite $k_\parallel$, and therefore is likely to be an overestimate of the saturation amplitude.

Quasilinear resistivity

DAVIDSON and GLADD [1975] presented a calculation of the anomalous resistivity and heating rates of the LHDI, motivated by measurements of anomalous resistivity in theta pinches, which will be reviewed here. The quasilinear equation for the evolution of the zero order distribution function of species j due to the presence of waves in the plasma is:

$$\left(\frac{\partial}{\partial t} + \mathbf{v}\cdot\frac{\partial}{\partial \mathbf{x}} + \frac{q_j}{m_j}\left(\frac{\mathbf{v}\times\mathbf{B}}{c}\right)\cdot\frac{\partial}{\partial \mathbf{v}}\right) f_j = \left(\frac{\partial f_j}{\partial t}\right)_\mathrm{anom} = -\frac{q_j}{m_j}\left\langle \delta\mathbf{E}\cdot\frac{\partial \delta f_j}{\partial \mathbf{v}}\right\rangle$$

The anomalous momentum exchange rate between species j and the fluctuations can be calculated by taking the first velocity moment of $(\partial f_j/\partial t)_\mathrm{anom}$ for velocity in

the current direction:

$$\left(\frac{\partial}{\partial t} n_j m_j V_{y,j}\right)_{\text{anom}} = q_j \left\langle \delta E_y \delta n_j \right\rangle \tag{2.6}$$

Eqn. 2.6 can then be used to compute an effective collision rate due to the waves:

$$\nu_{\text{eff}} = \frac{q_j}{n_j m_j V_{y,j}} \left\langle \delta E_y \delta n_j \right\rangle \tag{2.7}$$

Eqn. 2.7 provides an instability-model-independent way to experimentally determine the effective collision rate due to a measured spectrum of electric field and density fluctuations. However, simultaneous measurement of the amplitude and phase of both density and electric field fluctuations in a plasma is quite a difficult task, and was not attempted as part of this dissertation work. A simpler, yet model-dependent, expression for the effective collision rate can be obtained through using the linear theory for the LHDI to compute the density perturbation as a function of the electric field perturbation, $\delta n_j = -\chi_j i k_y \delta E_{y,k_y} / 4\pi q_j$. Using the expression for the ion density perturbation in Eqn. 2.2, the effective collision rate estimate reduces to [DAVIDSON and GLADD, 1975]:

$$\nu_{\text{LHDI}} = \text{Im}\left[k_\perp \frac{4\omega_{\text{p,i}}^2}{k_\perp^2 v_{\text{th,i}}^2} \zeta_{\text{i}} Z(\zeta_{\text{i}})\right]_{k_{\perp,\text{max}}} \frac{T_{\text{i}}}{m_{\text{e}} V} \frac{\mathcal{E}}{n T_{\text{i}}} \tag{2.8}$$

Where $k_{\perp,\text{max}}$ indicates that the expression should be evaluated at the frequency and wavenumber at peak growth, and $\mathcal{E} = (\delta E)^2 / 8\pi$. This expression can be re-written in the form

$$\nu_{\text{LHDI}} \propto \gamma \mathcal{E} / v_\phi,$$

where γ is the linear growth rate and v_{phi} is the phase velocity of the waves. In this form, it is clear that the effective collision rate is set by the rate of increase of wave momentum ($\mathcal{E}/v_{\text{phi}}$) due to the linear growth of the wave. Experimental

evaluation of Eqn. 2.8 can be performed with knowledge of only the amplitude of the electric field fluctuations in the plasma.

Review of simulations of the LHDI

Although predictions of strong anomalous resistivity due to the LHDI have been made, the usefulness of this resistivity in reconnection is questionable if the LHDI is suppressed at the center of high-beta current sheets where it would be needed to provide dissipation. Several simulations of the LHDI in current sheets have been performed to investigate the likelihood of the LHDI successfully penetrating to the center of a current sheet. BRACKBILL *et al.* [1984] reported on particle simulations of the LHDI in a two-dimensional Harris sheet geometry (the $x - y$ plane in the model presented in section 2.1), using an implicit code with mass ratios from 100 to 1836, but with only 90000 particles. The results of previous simulations by WINSKE and HEWETT [1975]; WINSKE and LIEWER [1978], CHEN and BIRDSALL [1983]; CHEN *et al.* [1983], and TANAKA and SATO [1981] were reviewed and included in a study of the nature of the saturation mechanism for the LHDI. It was demonstrated that the saturation mechanism in these simulations was controlled by electron dissipation, either through resonance broadening or through coupling to damped modes, and that ion trapping should not saturate the LHDI. The simulations by BRACKBILL *et al.* showed that under most conditions, any penetration of the LHDI to the magnetic null was very slow, as was any anomalous diffusion of density or magnetic field resulting from the turbulence. However, at relatively high values of the drift velocity (in fact, for $V/v_{\mathrm{th,i}} \sim 2.5$) it was found that penetration of the LHDI could occur, resulting in a possible anomalous resistivity at the magnetic null. In addition, a low-frequency magnetic perturbation was seen

to be non-linearly excited at the null by the LHDI, consistent with calculations by WINSKE [1981]. At later times, the LHDI amplitude was observed to decay during rapid diffusion of density and magnetic field, caused by the LHDI and the low-frequency perturbation. This low-frequency perturbation was also observed to develop in earlier two-dimensional particle simulations (at lower mass ratio) by TANAKA and SATO [1981], where the LHDI was also seen to penetrate to the null line and contribute substantial anomalous resistivity.

Recently, three-dimensional particle simulations of reconnection have been performed by HORIUCHI and SATO [1999], using millions of particles but at relatively low mass ratio ($m_e/M \sim 100$). These simulations found qualitatively the same result – that LHDI grows up early on the edges of the current sheet and drives a low-frequency magnetic instability at the null through modification of the neutral sheet profile. The low-frequency instability was identified as the drift-kink instability (DKI), which was so named by ZHU and WINGLEE [1996] after observations in simulations of the magnetotail, but which was perhaps first studied analytically by YAMANAKA [1977] (and later by WINSKE [1981]). It should also be pointed out that earlier 3D numerical studies of current sheet stability by PRITCHETT *et al.* [1996] had already made the suggestion that the magnetic perturbation at the null of earlier particle simulations of the LHDI was due to the growth of the DKI. In the simulations by HORIUCHI and SATO, the LHDI did not penetrate to the null unless a driving electric field was applied at the boundary. In the case that no driving electric field was present, a reconnection electric field was not induced at the null by the LHDI but was instead provided by the DKI, which was seen to generate significant anomalous resistivity. In the case that a driving electric field was applied at the boundary, the LHDI was seen to penetrate to the center of the

current sheet and initiate reconnection prior to excitation of the DKI. In either case, the LHDI was seen as quite essential to reconnection dynamics in these simulations, either through penetration to the null line or through nonlinearly driving the DKI. Recent two-dimensional particle simulations of current sheet stability by SHINOHARA and HOSHINO [1999] make similar predictions, but suggest that the development of the DKI can result in a strengthening of the density gradients near the current sheet and a re-excitation of the LHDI, resulting in efficient heating and dissipation of magnetic energy. It should be noted that the importance of the DKI in current sheets is currently the topic of much theoretical debate. The DKI has been primarily observed in low mass ratio particle simulations, and DAUGHTON [1999] has shown that while the growth rate of this instability can be large when the mass ratio is artificially small, the DKI should have negligible growth rate at realistic mass ratios in Harris equilibria. DAUGHTON does however suggest that other equilibrium profiles, especially those with significant background density, may increase the growth rate of the DKI.

Recently, an alternative to the picture of fast collisionless reconnection via the LHDI and the DKI has emerged, in which the Hall term in the generalized Ohm's law can result in fast laminar reconnection [BIRN *et al.*, 2001]. The simulations supporting this fast reconnection mechanism have been almost exclusively done in two-dimensions (the $x - z$ plane in the model presented in section 2.1), artificially suppressing instabilities like the LHDI. However, recent 3D simulations by ROGERS *et al.* [2000] using a Hall MHD model have shown that while LHDI does develop, it does not dramatically alter the physical picture of fast reconnection found in the 2D simulations. In fact, development of the LHDI was observed to *slow* the reconnection rate relative to the rate found in laminar 2D simulations.

The simulations summarized here demonstrate the theoretical controversy over the role of turbulence, specifically due to the LHDI, in reconnection. All of the simulations agree on the fact that the LHDI should be present in a reconnecting current sheet, but do not necessarily agree on the effect the instability should have on the process of magnetic reconnection. A key problem which can be addressed through experiment is the extent to which the LHDI can penetrate to the center of a current sheet and provide anomalous resistivity during reconnection.

2.2 Prior experimental studies of the LHDI

There have been very few experimental observations of the LHDI, and none in previous laboratory reconnection experiments. The earliest report of an experimental observation of the LHDI was made by GURNETT *et al.* [1976], who studied satellite measurements of fluctuations in the Earth's magnetotail. Analysis by HUBA *et al.* [1978] suggested that the frequency spectrum and amplitude of the waves was consistent with the operation of the LHDI in the magnetotail. SHINOHARA *et al.* [1998] also presented an analysis of recent satellite measurements in the magnetotail, suggesting that the observed fluctuations were due to the LHDI. An estimate of the anomalous resistivity due to these fluctuations was made, but it was found that the value of this resistivity was not enough to increase the growth rate of the tearing mode to the level necessary to explain the triggering of an associated substorm. However, SHINOHARA *et al.* suggested that the computed anomalous resistivity might still be enough to be essential to magnetic reconnection in the tail. In these satellite measurements, detailed observation and analysis of the LHDI is

quite difficult, as the profile and location of the tail current sheet is not well measured simultaneously to the fluctuation measurements. In both cases, however, the data suggested that electrostatic fluctuations might be strongest away from the center of the current sheet.

There have been experimental studies of the LHDI and associated instabilities such as the MTSI in other plasma configurations which are not directly relevant to the problem of magnetic reconnection. A CO_2 laser scattering measurement of fluctuations in a theta-pinch plasma was made by FAHRBACH *et al.* [1981]. These measurements provided some limited information on the wavelength and frequency spectrum of fluctuations in the plasma, and the characteristics were shown to be consistent with linear and nonlinear theories of the LHDI [DRAKE *et al.*, 1984]. Measurements in magnetoplasmadynamic (MPD) thrusters, which involve strong cross-field current and density gradients, have also revealed evidence for the LHDI and MTSI [CHOUEIRI *et al.*, 1991; TILLEY *et al.*, 1996]. CHOUEIRI *et al.* [1991] extended the theoretical model of the MTSI to include electromagnetic and collisional effects, and successfully used this theory to explain dispersion and growth characteristics measured experimentally in a thruster using wave launching techniques. Finally, the MTSI was studied in a low-beta Q-Machine by YAMADA and OWENS [1977] by driving cross-field electron $E \times B$ currents using radial electric fields in a layer smaller than the ion gyroradius. In these experiments stochastic ion heating was observed to take place as a result of the excitation of the instability.

2.3 Summary

In this Chapter, a review of the lower-hybrid drift instability has been presented. A linear, electrostatic theory of the LHDI was derived and will be used to explain features of the data presented in Chapter 4. A review of the linear and nonlinear theoretical literature on the LHDI was presented, discussing electromagnetic effects and possible nonlinear saturation mechanisms. Some simulations reviewed in this chapter have suggested that the LHDI might be important during collisionless reconnection through the direct generation of anomalous resistivity or through exciting a secondary electromagnetic instability at the magnetic null. However, other simulations have suggested that the Hall term is more important in providing fast collisionless reconnection and that the development of the LHDI actually might slow the rate of reconnection. Previous experimental studies of the LHDI were discussed. However, these studies have been very limited, and this dissertation work represents the first experimental identification and detailed characterization of the LHDI in a laboratory current sheet.

Chapter 3

Experimental Apparatus

The measurements reported in this dissertation were taken on the Magnetic Reconnection Experiment (MRX) [YAMADA *et al.*, 1997b] at Princeton Plasma Physics Laboratory. The details of the MRX experimental apparatus has been explained in depth elsewhere [HSU, 2000; YAMADA *et al.*, 1997b], and therefore this section, after a brief review of these details, will focus on experimental diagnostics and techniques crucial to the topic of this dissertation. These topics include the measurement of profiles of magnetic field, density and temperature in MRX current sheets and the measurement of high-frequency fluctuations in potential and magnetic field.

3.1 Magnetic Reconnection Experiment (MRX)

The Magnetic Reconnection Experiment was constructed for the purpose of studying magnetic reconnection in a well-controlled laboratory plasma where MHD is satisfied in the plasma bulk. A photograph of the experiment is shown in Figure 3.1

along with a schematic drawing of the apparatus.

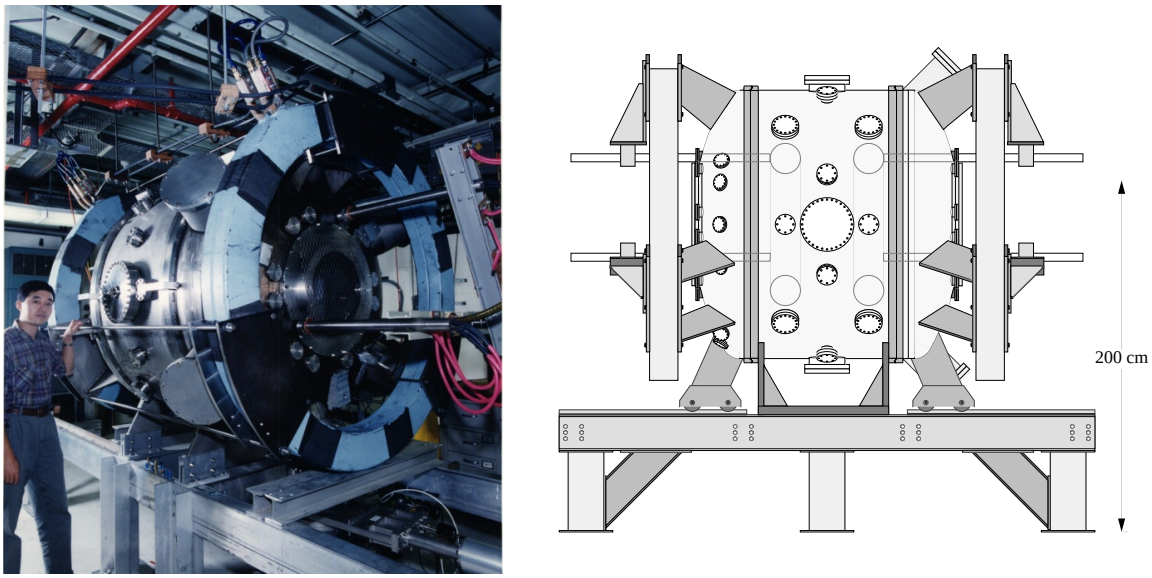

Figure 3.1: Photograph and schematic of the MRX device. The schematic shows an outline of the two coil sets internal to the vacuum vessel (flux cores).

Internal to the MRX vacuum vessel are two toroidally shaped coil sets, which are used to generate poloidal flux and breakdown the working gas and make a plasma. These coilsets are called "flux cores" and were originally used in formation of spheromak plasmas in fusion research [YAMADA *et al.*, 1981]. Current sheets are formed between the two flux cores, as shown in the cartoon in Figure 3.2. The fluxcores (shaded gray) are surrounded with a schematic surface of constant poloidal flux during "pull" reconnection in MRX. The large black arrows represent expected plasma flows during reconnection in MRX. The bulk of the experimental work reported in this dissertation is in MRX current sheets where no macroscopic B_θ (sometimes called "guide" field) is present during reconnection ("null-helicity" reconnection, as opposed to "co-helicity", where a guide field is present).

Table 3.1 shows a list of typical plasma parameters in MRX in the experiments

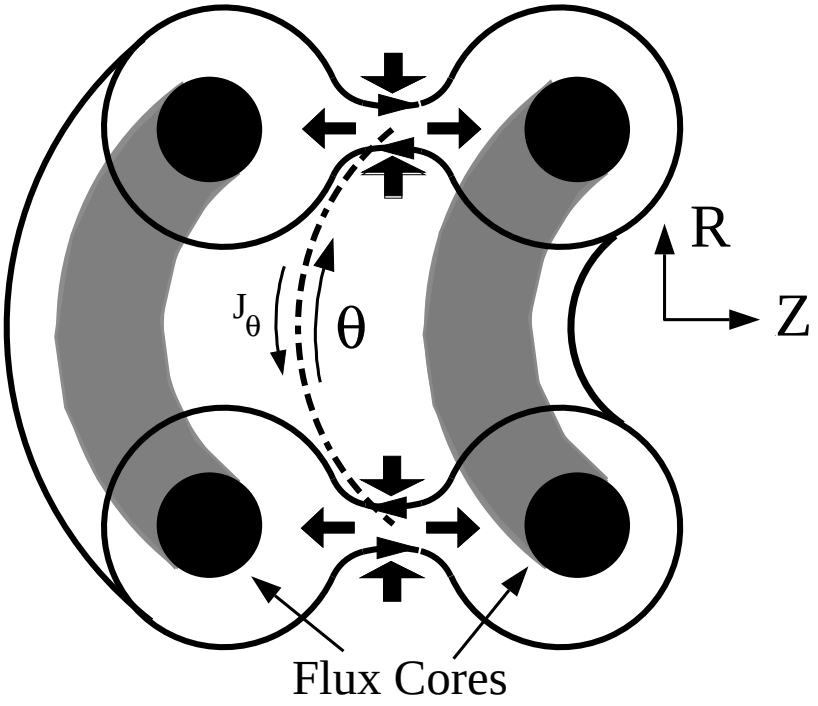

Figure 3.2: A cartoon showing the geometry of current sheets formed by flux cores in MRX.

reported in this dissertation. The ion temperature is not measured, however previous studies in helium have shown $T_i \gtrsim T_e$, and this is used in the estimates in Table 3.1.

3.2 Equilibrium profile measurements

The free energy sources available to drive instabilities in MRX current sheets can be at least partially revealed through the measurement of profiles of magnetic field (and hence current) and plasma temperature and density. The knowledge of these profiles will also allow theoretical prediction of instability characteristics in MRX

Central density, $n_{e,o}(\mathrm{cm}^{-3})$	$2-10\times10^{13}$
Central temperature, T_e (eV)	4-15
Sheet thickness, δ (cm)	1-5 ($\sim \rho_i$)
Peak magnetic field, B_o (G)	200-300
Normalized current density, $j/nev_{th,i}$	3-4
Ion thermal speed, $v_{th,i}$ (km/s)	30
Alfvén speed, v_A (km/s)	60
Lower hybrid frequency, f_{LH} (MHz)	10-15
Ion cyclotron frequency, $f_{c,i}$ (MHz)	0.2-0.4
Electron gyroradius, ρ_e (mm)	0.5
Normalized density gradient, $\epsilon_n\rho_i/2$	~ 1
Electron diamagnetic speed, $v_{D,e}$ (km/s)	$\sim 30(\sim v_{th,i})$
Plasma beta	~ 1 (locally ∞)
$\omega_{p,e}/\Omega_e$	100

Table 3.1: Parameters typical for MRX discharges studied in this dissertation.

for comparison with fluctuation measurements. These profiles were measured using diagnostics whose frequency response is limited to around a few hundred kilohertz, primarily due to the sampling time of the digitizers used (LeCroy 2264 and LeCroy 8210 operated at 500 kS/s).

The bulk of the diagnostics in the MRX device are for the measurement of magnetic fields, with close to 180 magnetic pickup coils in the vacuum vessel. These coils are hand wound, using 80 turns of 38 gauge magnet wire on 3mm diameter, 3mm long cylindrical plastic forms. The coils are distributed among three probes, as shown in Figure 3.3. Two of these probes (90-channel and 60-channel 2D probes) are for the purpose of measuring all three vector components of the field in a coarse

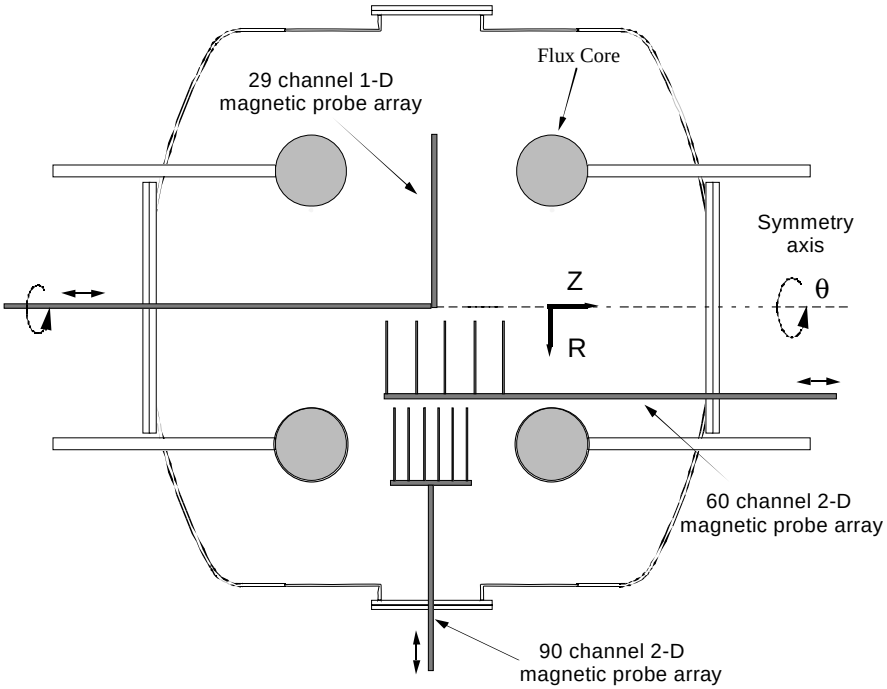

Figure 3.3: Schematic of the MRX vessel with magnetic probe arrays drawn.

grid spacing (4 cm near the current sheet, and 6 or 8 cm at radii well inside the current sheet location) in one toroidal plane of the experiment. Using these magnetic measurements and assuming axisymmetry, the poloidal flux and electric field can be calculated:

$$\psi = \int_0^R 2\pi r B_z(r) \mathrm{d}r$$

$$E_\theta = -\frac{1}{2\pi R}\frac{\partial \psi}{\partial t}$$

Figure 3.4(a) shows poloidal flux derived from magnetic probe measurements. To generate this figure, a scan of the 90 channel probe in the r direction is made, and interpolation is performed in the z direction. Figure 3.4(b) shows magnetic field vectors derived from measurements of B_z and B_r.

A high-resolution (0.5 cm) 1D magnetic probe is used to measure B_z along the r

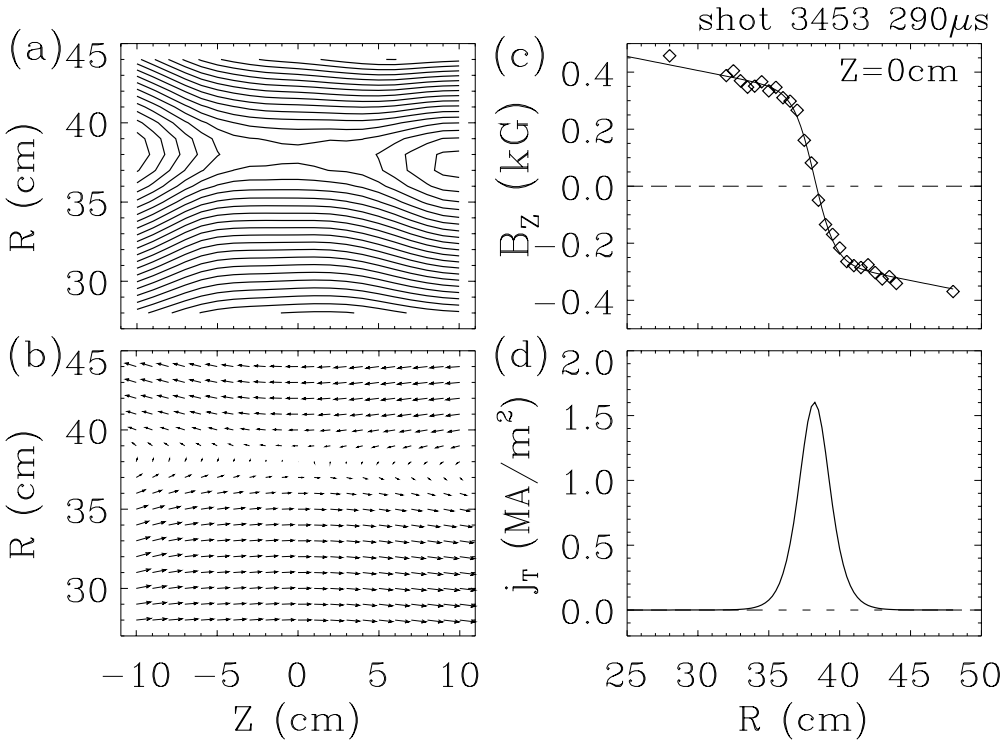

Figure 3.4: Example magnetic field measurements in MRX. (a) Poloidal flux derived from 2D magnetic measurements in MRX. (b) Magnetic field vectors in the current sheet. (c) High-resolution 1D measurement of the reconnecting field, along with fit to Harris profile. (d) Neutral sheet current density derived from Harris profile fit.

direction. Figure 3.4(c) shows a measurement using this probe at $z = 0$. The magnetic field profile in MRX is well described by the Harris sheet theoretical equilibrium profile [HARRIS, 1962; YAMADA *et al.*, 2000]. The measured B_z field in MRX is fit to this theoretical profile ($B \propto \tanh((r - r_o)/\delta)$) and the current density is derived analytically from the fit. A plot of the derived current density is shown in Figure 3.4(d).

A triple Langmuir probe [CHEN and SEKIGUCHI, 1965] is employed to measure density (n_e), electron temperature (T_e), and floating potential (V_f) profiles in the current sheet. Both radially-inserted and axially-inserted probes have been

used, to allow measurements in the $r - z$ plane in MRX. Figure 3.5 shows triple Langmuir probe along with magnetic data taken at $z = 0$. Radial profiles taken by the Langmuir probe are acquired through shot-to-shot positioning of the probe and averaging multiple shots per position. The error bars shown are representative of the shot-to-shot variation in the data. The electron density profile in MRX is typically strongly peaked at the current sheet, while the electron temperature is usually broader.

3.3 High-frequency fluctuation measurements

3.3.1 Probe-tip buffer amplifiers

Initial high-frequency measurements in MRX using probes revealed broadband noise generated by impedance mismatches in both power transmission lines from the MRX capacitor banks and in transmission lines of the diagnostics themselves. This noise precluded the detection of signals from the plasma and had to be addressed in order to study fluctuations in the MRX current sheet. In order to improve immunity to noise generated by the power circuitry in MRX and to facilitate active impedance matching in the diagnostics, small broadband buffer amplifiers were built into probes used for the fluctuation studies reported here[1].

The circuit used is based on the Texas Instruments/Burr-Brown OPA 682 operational amplifier. A schematic of the amplifier circuit is shown in Figure 3.6, and a picture of a completed circuit board is shown in Figure 3.7. The use of a miniature SOT-23 surface mount package for the buffer, along with 0805 package surface mount capacitors and resistors, allowed the placement of all components

[1]Similar diagnostic techniques have been employed before, see, e.g. [BENJAMIN, 1982]

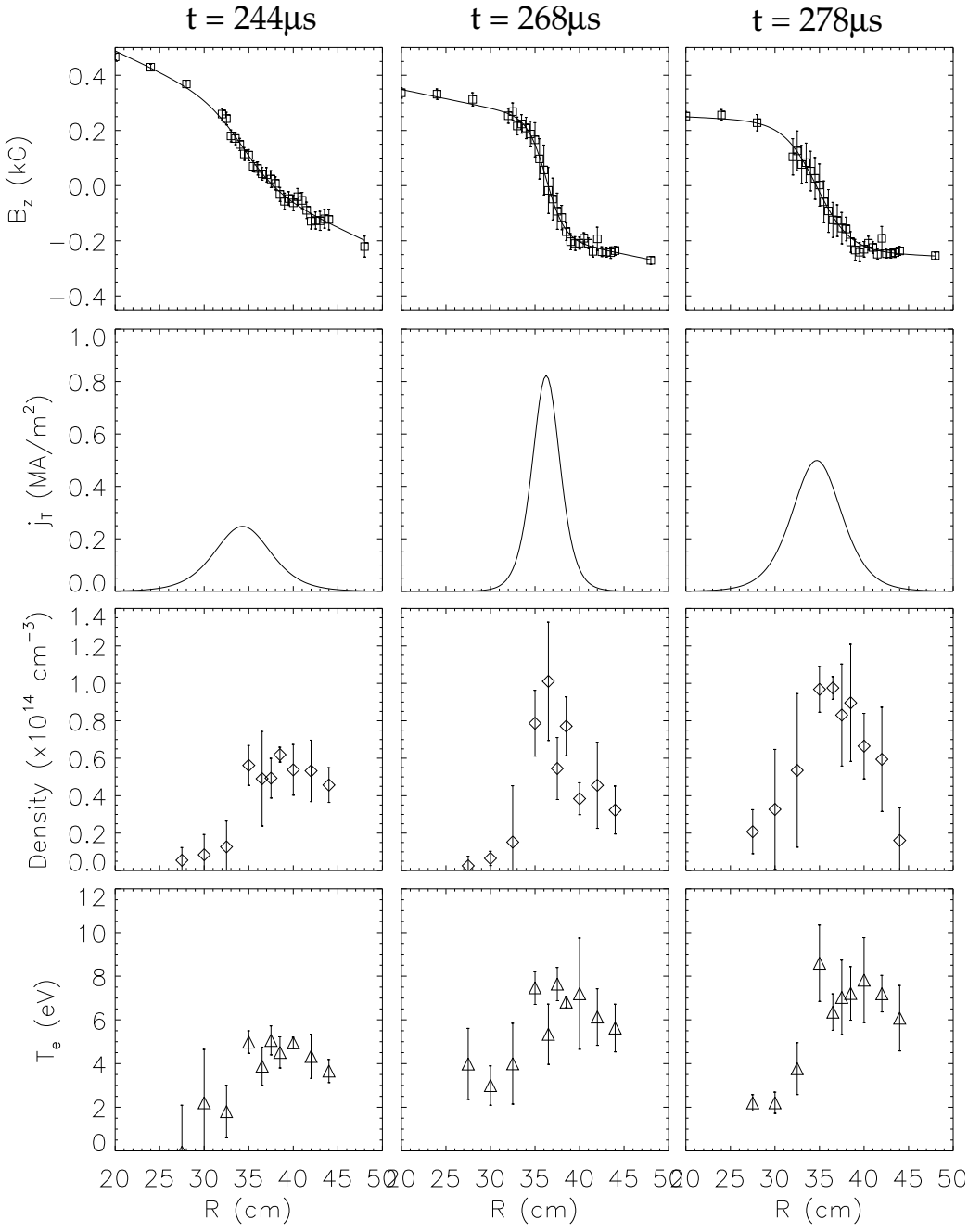

Figure 3.5: Example triple Langmuir probe measurements in the MRX current sheet.

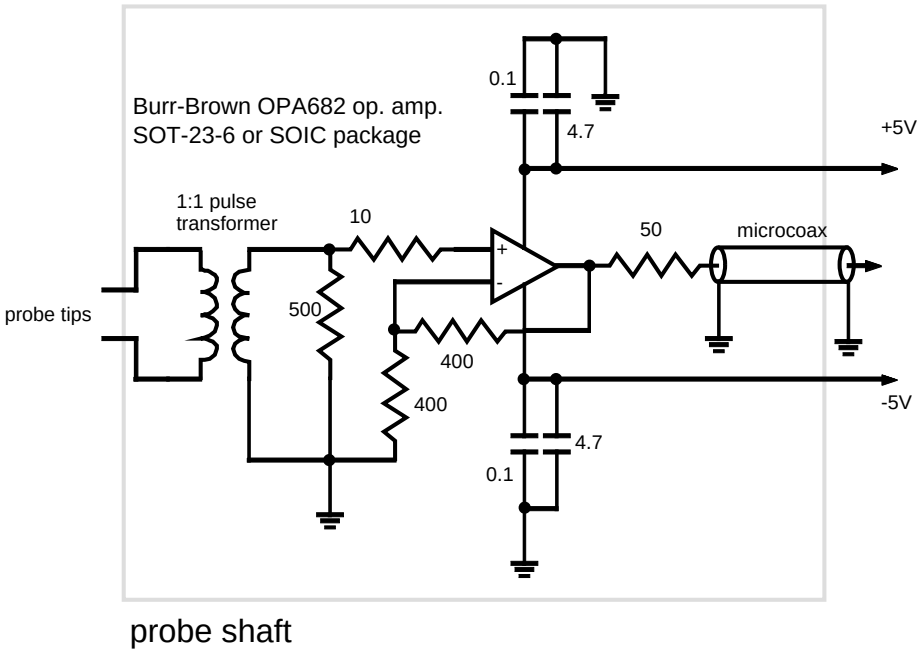

Figure 3.6: Schematic of the buffer amplifiers used in fluctuation probes

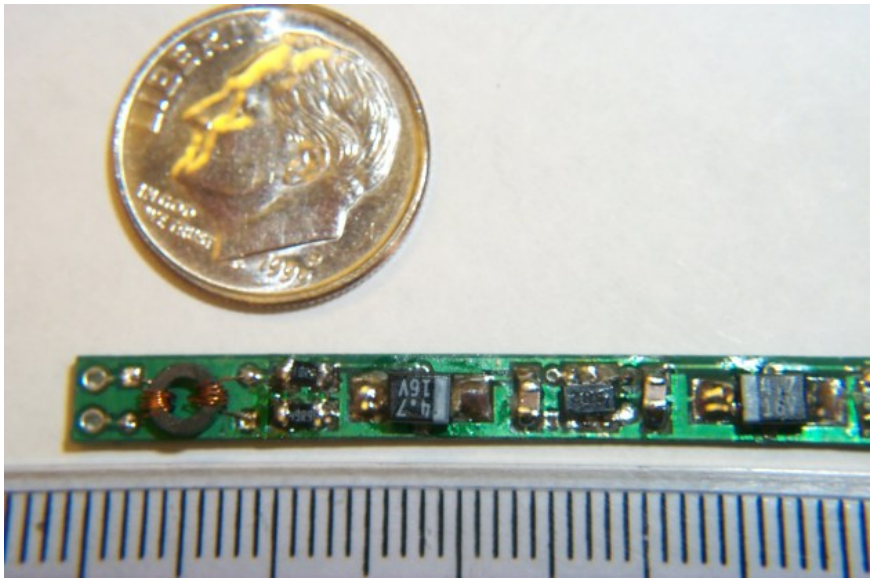

Figure 3.7: A picture of an assembled buffer amplifier circuit board.

on a double-sided printed circuit board of 4.5×50 mm approximate dimensions (see Fig. 3.7). The boards are placed inside 1/4″ (0.635 cm) to 3/8″ (0.9525 cm) stainless probe shafts, which allows the leads connecting the probe tips to the amplifier to be only several millimeters (5-10mm) long. The amplifier allows an easy transition from a potentially high-impedance probe tip into a 50Ω transmission line, eliminating impedance matching issues. While the overall voltage gain is unity, the amplifier does boost the signal current to assist in noise immunity. A high-bandwidth ferrite core 1:1 pulse transformer is used to provide isolation from the plasma in electrostatic (Langmuir probe) diagnostics, but is not present in amplified magnetic pick-up coil diagnostics. The magnetic field value of the core saturation is well above the fields used in these experiments ($\sim$ 200G). Perturbation of the background field due to the presence of a high-μ ferritic material is negligible due to the size and geometry of the transformer (see Appendix A for more thorough discussion of this point). The amplifier is powered using batteries placed at the end of the probe shaft (3 1.5V Alkaline batteries to provide $\pm$4.5V). The battery power is brought in on a shielded twisted triplet (V+,V-, return). Signals are propagated down the probe shafts using low-loss semi-rigid coaxial line (UT-85LL). The UT-85 cable is capacitively decoupled from the probe shaft using several layers of aluminized Mylar. In cases where more than one amplifier is used in a single shaft, the individual channels are individually wrapped in aluminized Mylar to capacitively decouple one channel from another. Signal transport from the probe to the digitizing oscilloscope (approximately 12m away) is accomplished using low-loss RG8 coaxial cable. The bandwidth of the system (amplifier input to RG8 output) is measured to be 100kHz $\lesssim f \lesssim$ 125MHz when the transformer is used for isolation and $f \lesssim$ 300MHz when no transformer is used. Figure 3.8(a)

shows a calibration of the amplifier gain (including a transformer), performed using a Wavetek 2001 frequency source and a Tektronix 510A oscilloscope. Output

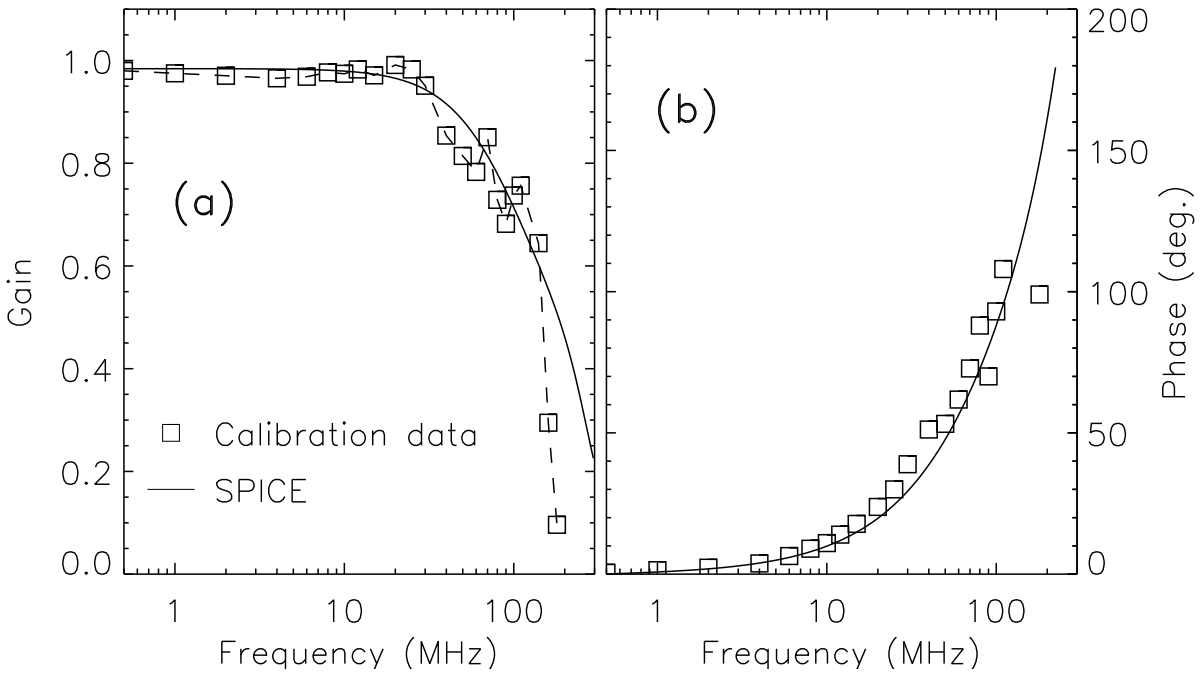

Figure 3.8: (a) Amplifier gain as a function of frequency, compared to a simulation using SPICE. (b) Measured phase shift during calibration, also compared to SPICE output.

of a SPICE simulation of the amplifier board is also plotted. There is good agreement between the SPICE model and the calibration data, aside from discrepancies at high frequency which are likely due to impedance mismatch problems between the calibration source and the transformer input, a problem that is unique to the calibration and should not effect the measurement. From this calibration, a 3dB point of roughly 125-150MHz is evident. Figure 3.8(b) shows the measured phase shift between the input and output of the amplifier board, along with the SPICE calculated phase, again showing good agreement. The input impedance of the amplifier, computed using the SPICE simulation, is shown in Figure 3.9. The input

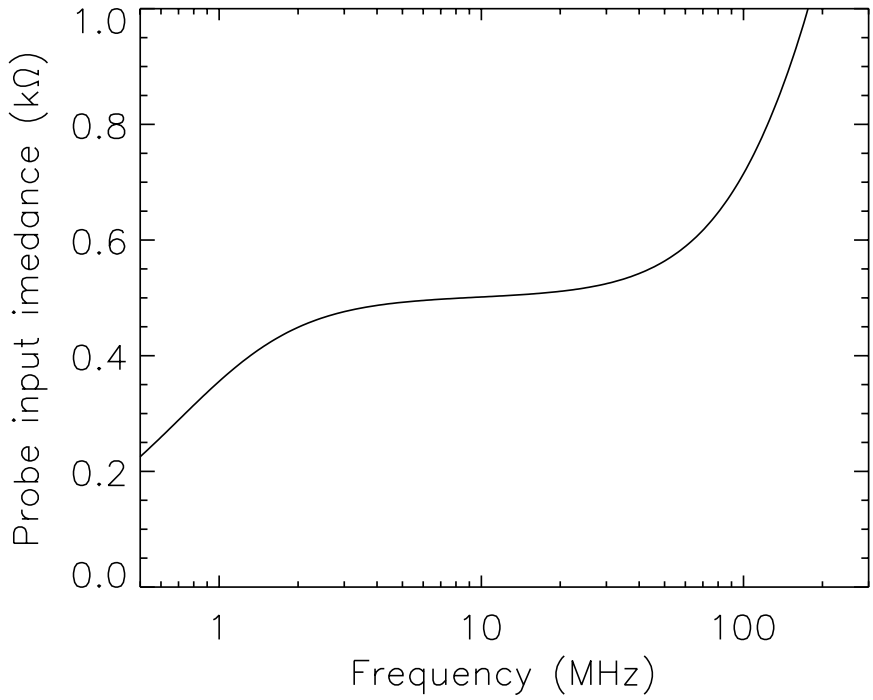

Figure 3.9: Input impedance of the amplifier, calculated from a SPICE simulation.

impedance is roughly constant and equal to 500Ω from 1MHz to 30MHz. High frequency signals are digitized using high sampling rate oscilloscopes (various models, including Tektronix 510A, 754C, 714L; LeCroy Waverunner 3345). Labview software on a Solaris workstation was used to communicate with the oscilloscopes over a GPIB interface and data was saved to an NFS attached disk for analysis using IDL.

3.3.2 Electrostatic fluctuation probes

Fluctuations in the plasma floating potential were measured using differential floating Langmuir probes. Floating potential measurements were chosen over ion saturation current measurements due to the difficulty of measuring high frequency

current signals accurately in the presence of cable capacitance. The floating potential is not the actual plasma potential, but its frequency spectrum and relative amplitude profile should correspond well to fluctuations in the actual plasma potential. Low frequency floating potential signals in MRX can be on the order of 100V, and therefore a differential measurement is preferred to remove long-wavelength, low-frequency components and measure fluctuating signals on the order of 1V. Single floating probe measurements using voltage division were not practical due to the limited dynamic range of the data acquisition system (8 bit) and noise generated by the high-power pulsed electronics, which would overwhelm the signals of interest if voltage division were used. Differential floating Langmuir probes are constructed using two spatially separated cylindrical tungsten wires sheathed in alumina (Al_2O_3). The diameter of the tungsten tips varied from 30 mil (0.762 mm) to 5 mil (0.127 mm), and in all probe tips a 1 mm length of the wire is exposed to the plasma.

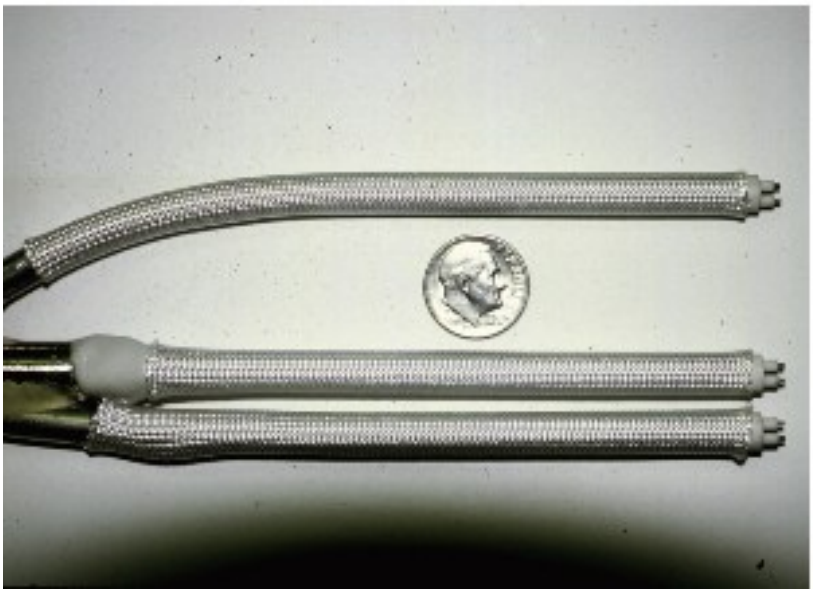

Figure 3.10: A 3-point differential floating Langmuir probe

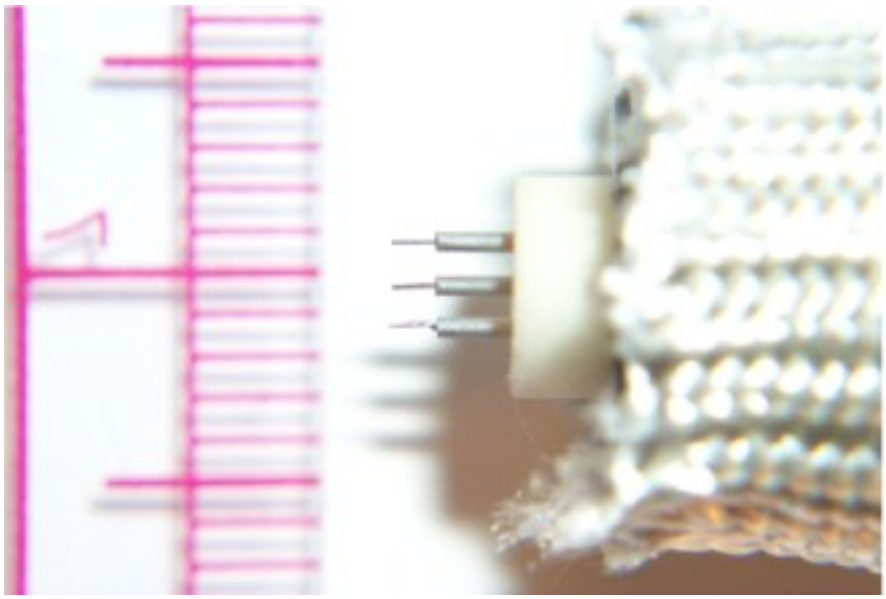

Figure 3.11: A 3 pin floating Langmuir probe for small-scale correlation measurements.

Figures 3.10 and 3.11 show two of the probes used in fluctuation studies reported here. Figure 3.10 is a three point double Langmuir probe, with 30 mil tips and 3 mm intertip spacing for each double probe. The spacing between double probes for this three point probe is 1 cm and 3 cm. The three point double probe was used to measure single point characteristics of the fluctuations in the MRX current sheet (radial profiles, frequency spectra) as well as long wavelength correlations. Three buffer amplifiers were used in this probe, one per double probe tip. The probe tips are connected to 1/4" stainless steel shafts, which houses the amplifier board and the UT-85LL semi-rigid cable. The steel shaft is covered with a fiberglass sleeve to help reduce the interaction of the plasma with the metal shaft. The probe shown in Figure 3.11 was used to study small scale correlations, and has three 5 mil tips spaced 1 mm apart. The central tip was used as a reference

for the other two tips, so that two measurements of the differential floating potential could be made at 1 mm separation. Two buffer amplifiers were used in this diagnostic, one per differential floating potential measurement. Another similar correlation probe was also used in these experiments, with tip sizes of 20 mil and interprobe spacing of 3.5 mm. Both correlation probes used 3/8" stainless steel shafts to house the amplifiers and semi-rigid coaxial line. In all probes, a vacuum seal is made near the probe tip (so that the amplifier is not exposed to vacuum) using a low-outgassing epoxy (Master Bond part number EP21TCHT-1). The probe shafts exit the vacuum vessel through O-ring seals (Wilson seals) and are isolated from the vacuum vessel (and allowed to float with respect to the plasma) using ceramic breaks. The floating probes were inserted radially into MRX plasmas, as shown in Figure 3.12.

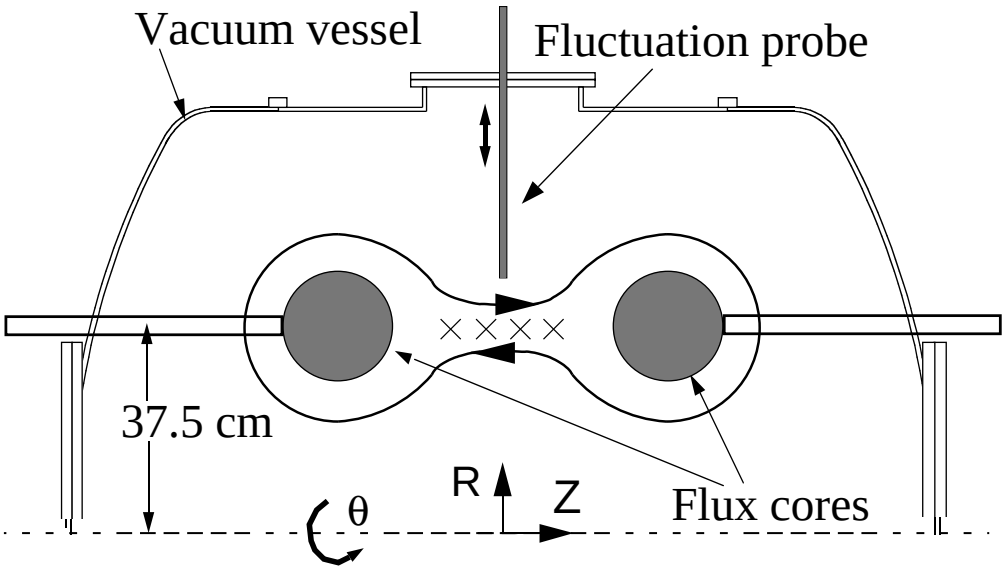

Figure 3.12: Schematic of the measurement geometry for radially inserted fluctuation diagnostics

The probe tips in these probes are coupled directly to the primary side of the transformer on the buffer amplifier board. The impedance seen by the plasma is

dependent on frequency, and is controlled by the efficiency and inductance of the transformer ($L \sim 20\mu$H) as well as the input impedance to the amplifier (set to 500Ω using a surface mount resistor). Over a wide range (1MHz $\lesssim f \lesssim$ 100MHz), the plasma sees roughly the input impedance of the amplifier, $Z \sim 500\Omega$, as shown in Figure 3.9. As the gain rolls off toward lower frequency, the input impedance of the probe drops, and is roughly 50Ω at 100kHz. It is desirable for the input impedance of the probe to be greater than the impedance of the sheath between the probe tip and the plasma in order to accurately measure the floating potential. The sheath impedance can be estimated roughly using the $I - V$ characteristic of a Langmuir probe near the floating potential [HUTCHINSON, 1987]:

$$\frac{dI}{dV} = \frac{1}{Z_{\text{sheath}}} = \frac{e}{T_e}(I - I_{\text{sat}})$$

Where $I_{\text{sat}} = -eA_p \exp(-1/2) n_e \sqrt{T_e/M}$ is the ion saturation current to the probe. At the floating potential, $I = 0$, and therefore:

$$Z_{\text{sheath}} = \frac{\sqrt{T_e M}\exp(1/2)}{A_p e^2 n_e}$$

For typical low-collisionality MRX parameters ($T_e \sim 8$eV, $n_e \sim 5 \times 10^{13}\text{cm}^{-3}$) this expression yields $Z_{\text{sheath}} \approx 25\Omega$ for a 30 mil probe tip. At higher frequencies ($f \gtrsim$ 1MHz), the probe input impedance ($Z_p \sim 500\Omega$) should be sufficiently large to allow the probe to float with respect to the plasma (and not load down the plasma).

The use of invasive diagnostics such as probes introduces the possibility of perturbing the plasma at the measurement site and therefore affecting the phenomena which one is attempting to measure. It is usually difficult to quantify this perturbative effect, but we can gain some insight into the problem by experimentally investigating the perturbation of a second probe on the measured signal of the fluctuation diagnostic. For the diagnostics used in this dissertation, it was found

that qualitatively there was no significant perturbation on the measured signals when a second probe was placed close (within a few cm) of the fluctuation diagnostic. However, significant perturbation to the signals were found when many (3 or more) diagnostics were placed nearby in the same toroidal plane as the fluctuation probe. In these cases, there was an obvious perturbation to the current sheet profiles in MRX (density and current density profile). For this reason, such probe arrangements were avoided during the experiments reported here.

Interpretation of differential floating potential measurements

We will now discuss the relationship between the actual fluctuating floating potential and the output of a differential floating Langmuir probe inserted into the plasma. We will first consider a monochromatic wave in the floating potential, $\phi = \phi_{o,k} \exp(ikx - i\omega t)$, traveling past two floating probe tips spaced Δx apart in the direction of propagation (x direction). We can easily calculate the potential difference between the two spatially separated probes, $\delta\phi_f = \phi_2 - \phi_1$:

$$\delta\phi_f = 2\phi_{o,k} \sin\left(\frac{k\Delta x}{2}\right) \exp\left(-\frac{ik\Delta x}{2} - i\omega t\right) \tag{3.1}$$

Here we have assumed that probe 1 is located at $x = 0$ and probe 2 is located at $x = \Delta x$. The measured differential signal in the presence of a monochromatic wave will therefore be significantly reduced near $k\Delta x/2 = n\pi$, or when the spacing is comparable to the wavelength of the wave. In the case of a superposition of monochromatic waves, the differential probe will measure a fraction of the actual fluctuation amplitude, depending on the wavenumber spectrum of the fluctuations. In order to make an estimate of the fraction of fluctuation amplitude detected by a differential probe, we will assume a k spectrum of $\phi_{o,k}^2$ which is described by the theoretically predicted linear growth rate for the LHDI in typical

MRX conditions, an example of which is shown as the solid line in Figure 3.13(a). The ensemble (or time) average of the square of the differential measurement of

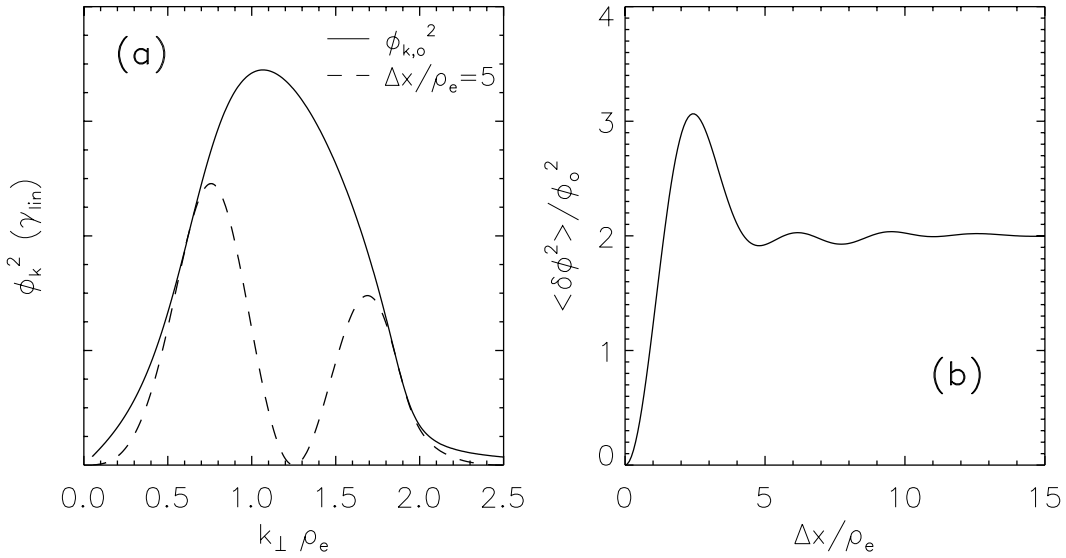

Figure 3.13: (a) The effect of a differential measurement on the spectrum of LHDI waves (solid line), for normalized probe spacing $\Delta x/\rho_e = 5$ (dotted line). (b) Total (k integrated) squared differential amplitude as a function of the normalized probe spacing.

this spectrum of waves is then, from Eqn. 3.1:

$$\left\langle (\delta\phi_f)^2 \right\rangle = 4 \int \sin^2\left(\frac{k\Delta x}{2}\right) \phi_{o,k}^2 dk$$

Again, this quantity depends crucially on the ratio of the differential probe spacing to the wavelength of the waves. The expected differentially measured spectrum for $\Delta x/\rho_e = 5$ is shown as a dotted line in Figure 3.13(a). Figure 3.13(b) shows the predicted total squared amplitude (integrated over k) as a function of normalized probe spacing, $\Delta x/\rho_e$. At normalized probe spacings above a few ($\Delta x/\rho_e \gtrsim 3$), the total measured wave amplitude is fairly constant:

$$\left\langle (\delta\phi_f)^2 \right\rangle \sim 2\phi_o^2 = \int 2\phi_{o,k}^2 dk$$

The normalized probe spacing used in the single point studies is typically well into this approximately constant region, with $\Delta x/\rho_e \gtrsim 4$.

Spatially separated differential floating potential measurements are used in this dissertation to ascertain the correlation length and propagation characteristics of fluctuations in the plasma. Here we will discuss the relationship between the measured phase difference between spatially separated differential probes and the actual phase difference in the waves. An example of the primary type of two-point correlation diagnostic used in these studies is shown in Figure 3.11. Two differential measurements are made using three probe tips, the central tip being used as a reference for both of the outer two tips, as shown in Figure 3.14. If we let $x_2 = 0$, and $x_3 = -x_1 = \Delta x$, in the presence of a monochromatic wave the two differential outputs will be (using Eqn. 3.1):

$$\begin{aligned} \delta\phi_{f,a} &= 2\phi_{o,k} \sin\left(\frac{k\Delta x}{2}\right) \exp\left(\frac{ik\Delta x}{2} - i\omega t\right) \\ \delta\phi_{f,b} &= 2\phi_{o,k} \sin\left(\frac{k\Delta x}{2}\right) \exp\left(-\frac{ik\Delta x}{2} - i\omega t\right) \end{aligned}$$

The difference in phase between the two differential signals is then $\Delta\varphi = k\Delta x$, exactly what would be expected for the phase difference between two single probes separated by Δx. Thus the we can interpret the phase shift in the two-point differential measurement as the actual phase difference in the floating potential (as measured from the centerpoint of probe pair "a" ($-\Delta x/2$) to the centerpoint of probe pair "b" ($\Delta x/2$)).

In order to construct dispersion relations from spatially separated differential probe signals, an analysis technique first presented by BEALL *et al.* [1982] is used, and we will review this technique here. The cross-spectrum, of the two differential

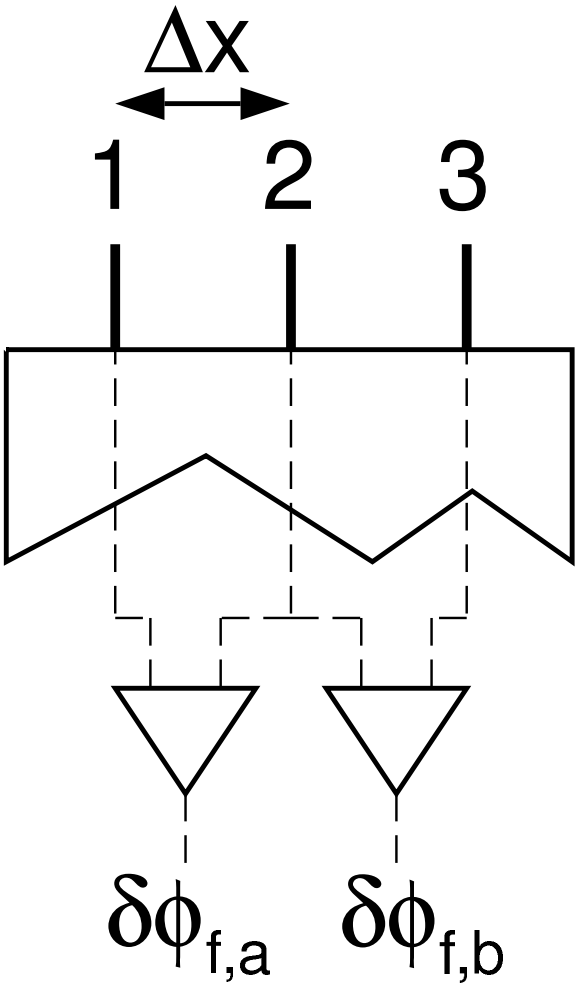

Figure 3.14: Schematic of a two-point differential floating potential probe.

probe signals is:

$$\mathcal{X}_{a,b} = \delta\tilde{\phi}_{f,a}\delta\tilde{\phi}^{*}_{f,b}.$$

Where $\delta\tilde{\phi}_{f,a}$ is the Fourier transform of the signal from differential probe "a". The "local" wavenumber, $K(\omega)$, as a function of frequency can be obtained from the phase in the cross-spectrum ($\varphi(\omega)$):

$$\begin{aligned} \varphi(\omega) &= \tan^{-1}\left(\frac{\mathrm{Im}\mathcal{X}_{a,b}}{\mathrm{Re}\mathcal{X}_{a,b}}\right) \\ K(\omega) &= \frac{\varphi(\omega)}{\Delta x} \end{aligned}$$

For the case of a single monochromatic wave, the cross-spectrum for spatially separated differential probes can be computed using the single point expression in Eqn. 3.1:

$$\mathcal{X}_{\mathrm{a,b}} = 4\phi_{\mathrm{o,k}}^2 \sin^2\left(\frac{k\Delta x}{2}\right) \exp\left(-ik\Delta x\right) \delta(\omega - \omega_{\mathrm{o}})$$

The phase in this cross-spectrum is $\varphi = k\Delta x$ (at the monochromatic wave frequency), and therefore $K = \varphi/\Delta x = k$, as expected.

In the presence of broadband turbulence, a statistical technique should be employed to estimate the dispersion relation of the waves and the wavenumber spectral width. Given M realizations of the two separated probe signals, a local wavenumber and frequency spectrum can be obtained by computing the local wavenumber spectrum in each realization, then binning the squared Fourier amplitude in each signal by local wavenumber and frequency:

$$\hat{S}_l(K,\omega) = \frac{1}{M}\sum_{j=1}^{M} \Theta_{0,\Delta K}\left(K - K^j(\omega)\right) \frac{1}{2}\left(S_a^j(\omega) + S_b^j(\omega)\right)$$

Where $\Theta_{0,\Delta k}$ is unity if its argument is between 0 and ΔK (the size of the wavenumber bin), and is zero elsewhere. Here we introduce $S_a(\omega) = |\delta\tilde{\phi}_{\mathrm{f,a}}|^2$, which is the squared Fourier amplitude of the signal from differential probe "a". The statistical local dispersion relation ($\hat{K}(\omega)$) and spectral width ($\hat{\sigma}_K^2(\omega)$) can then be computed, at a discrete set of $N = 2\pi/(\Delta K \Delta x)$ points:

$$\hat{K}(\omega) = \sum_{m=-N/2+1}^{N/2} m\Delta K \frac{\hat{S}_l(m\Delta K,\omega)}{\left(\hat{S}_a(\omega) + \hat{S}_b(\omega)\right)/2}$$

$$\hat{\sigma}_K^2(\omega) = \sum_{m=-N/2+1}^{N/2} \left(m\Delta K - \hat{K}(\omega)\right)^2 \frac{\hat{S}_l(m\Delta K,\omega)}{\left(\hat{S}_a(\omega) + \hat{S}_b(\omega)\right)/2}$$

Where $\hat{S}_a(\omega) = (1/M)\sum_j S_a^j(\omega)$ is the average squared Fourier amplitude of signal "a". The spectral width represents the spread of wavenumbers about the average wavenumber at a single frequency. This width can be created by turbulent

(nonlinear) broadening of the dispersion relation of the waves but might also be contributed to by experimental errors.

Effects of decorrelation

The discussion in the preceding section is primarily based on the assumption of monochromatic, ungrowing waves propagating in the plasma. The predicted linear growth rate for the LHDI in MRX plasmas, as shown in Figure 2.2, is comparable to the real frequency of the instability. We might therefore expect significant growth and decorrelation of the waves on length scales comparable to the wavelength of the wave. A short decorrelation length should effect the amplitude and phase difference measured by the differential probe and differential probe pairs, respectively.

We can rewrite the ensemble average of the measured square differential floating potential as:

$$\left\langle \left|\delta\phi_{\mathrm{f}}\right|^2 \right\rangle = \left\langle (\phi_1 - \phi_2)^2 \right\rangle = 2\left\langle \left|\phi_{\mathrm{f}}\right|^2 \right\rangle - \langle \phi_1 \phi_2^* \rangle - \langle \phi_1^* \phi_2 \rangle$$

Where ϕ_1 and ϕ_2 are the floating potentials at each tip, and we assume that $\langle |\phi_1^2| \rangle = \left\langle \left|\phi_2\right|^2 \right\rangle = \left\langle \left|\phi_{\mathrm{f}}\right|^2 \right\rangle$. One might expect that the cross terms in the expression for $\langle (\delta\phi_{\mathrm{f}})^2 \rangle$ would behave like $\langle \phi_1 \phi_2^* \rangle \propto \exp(-\Delta x/\lambda_{\mathrm{d}})$, where Δx is the probe tip spacing and λ_{d} is the decorrelation length in the turbulence. If the tips are spaced much larger than the decorrelation length, then the cross terms should tend toward zero, and the ensemble average of the square signal difference should be approximately

$$\left\langle \left|\delta\phi_{\mathrm{f}}\right|^2 \right\rangle \approx 2\left\langle \left|\phi_{\mathrm{f}}\right|^2 \right\rangle .$$

It is interesting to note that this is the same relationship as found in Figure 3.13(b)

for ungrowing waves (when the probe spacing is appropriate). Therefore, in the case of either correlated or decorrelated probe tips, the average of the square differential measurement should be approximately twice the square of the actual floating potential amplitude in the plasma.

The ability to interpret the phase difference between spatially separated potential measurements as being due to the propagation of a wave crucially depends on the decorrelation length. If the decorrelation length is small (comparable to or smaller than the probe spacing), new growth and damping as the waves propagate between the two measurement sites might result in a randomizing of the measured phase difference. It is therefore important to attempt phase measurements using two-point probes whose separation is sufficiently smaller than the decorrelation length in the turbulence.

3.3.3 Magnetic fluctuation diagnostics

Magnetic field fluctuations were measured using magnetic pick-up coil based probes. The coils used in these probes are identical to those used for low-frequency profile measurements as described in Section 3.2. The coils are coupled directly to the buffer amplifier with no transformer. The bandwidth of the probe is set by the L/R time of the coil ($L \approx 10\mu$H) based on the input impedance of the buffer amplifier (500Ω), which is around 20ns (making the bandwidth $f \lesssim$ 50MHz). The lower frequency end of the sensitivity of these coils is $f \lesssim$ 1kHz, as they are capable of measuring the lowest frequency fields generated by the MRX capacitor bank. The voltage signal on the coil due to magnetic fluctuations of amplitude $\tilde{B}$ and frequency ω can be calculated from the time rate of change of the magnetic flux, Φ,

through the coil:

$$V_{\text{out}} = \frac{\partial \Phi}{\partial t} \approx NA\frac{\partial \tilde{B}}{\partial t} \approx \omega NA\tilde{B}$$

where N is the number of turns and A is the cross-sectional area of the coil. The NA of the coil can be measured through a calibration procedure where the output of the coil is measured in the presence of a known amplitude and frequency applied field. Using this technique, an $NA \sim 2$ cm^2 is measured for coils used in fluctuation probes. This value can be used to to determine absolute fluctuating field values from probe output voltage.

Figure 3.15: Left: Photo of a magnetic coil attached to a buffer amplifier prior to insertion in to a stainless steel probe shaft and glass cap. Right: Photo of magnetic fluctuation probe tip, showing glass cap (with graphite coating internally) attached to a 1/4" stainless steel shaft.

Figure 3.15 shows a magnetic coil attached to a buffer amplifier as well as the tip of a completed single-coil magnetic fluctuation probe. The coil is enclosed in a 5 mm O.D. glass tube which has been sprayed internally with a conductive layer of graphite (T.V. tube coat) to provide electrostatic isolation from the plasma. The glass cap is attached to a 1/4" stainless steel shaft using low-outgassing epoxy.

The diameter of the coil chosen of course has an effect on the efficiency of detecting fluctuations at certain wavelengths. The magnetic probe measures the time rate of change of the flux passing through the coil. Assuming a square coil (for simplicity) and for a monochromatic signal $B = B_o \exp(ikx - i\omega t)$, the mean square amplitude measured by a coil of diameter d is:

$$\frac{\langle B^2 \rangle}{B_o^2} = \frac{1}{k^2 d^2} \left(\sin^2(kd) + (1 - \cos(kd))^2 \right) = \frac{2}{k^2 d^2} (1 - \cos(kd))$$

This results in efficient measurement of long wavelength ($\lambda \gtrsim d$) fluctuations, but the coil should fail to adequately detect fluctuations of shorter wavelengths. The two sets of diagnostics presented in this chapter should be complementary in this regard. The electrostatic probe has difficulties measuring waves with $\lambda \gg \Delta x$, precisely where the magnetic diagnostic should excel, and for $\lambda < \Delta x$, the electrostatic probe should work well, while the efficiency of the magnetic diagnostic should begin to falter (here we are equating the coil diameter with Δx). This helps with the goal of detecting all fluctuations in the MRX current sheet, as fluctuations should not be able to "hide" in the blind spot of a single diagnostic. However, in order to determine the relationship between electrostatic and magnetic fluctuations, a region of overlap in the efficiency of the two diagnostics is desired. This region of overlap is limited by the size of the magnetic coils employed, which in this dissertation work were $d \sim 3$ mm, comparable to the probe-tip separation in the primary electrostatic probe. Figure 3.16 shows the total magnetic fluctuation amplitude detected by a coil, as a function of the normalized diameter of the coil (here $\Delta x = d$), calculated in the same manner as for Figure 3.13. We have assumed that the magnetic wavenumber spectrum of the fluctuations is identical to the electrostatic wavenumber spectrum (which may be an incorrect assumption). The amplitude for the electrostatic differential measurement is repeated for comparison

(dotted line). For normalized coil diameter $d\rho_e \gtrsim 4$, as might be expected at the

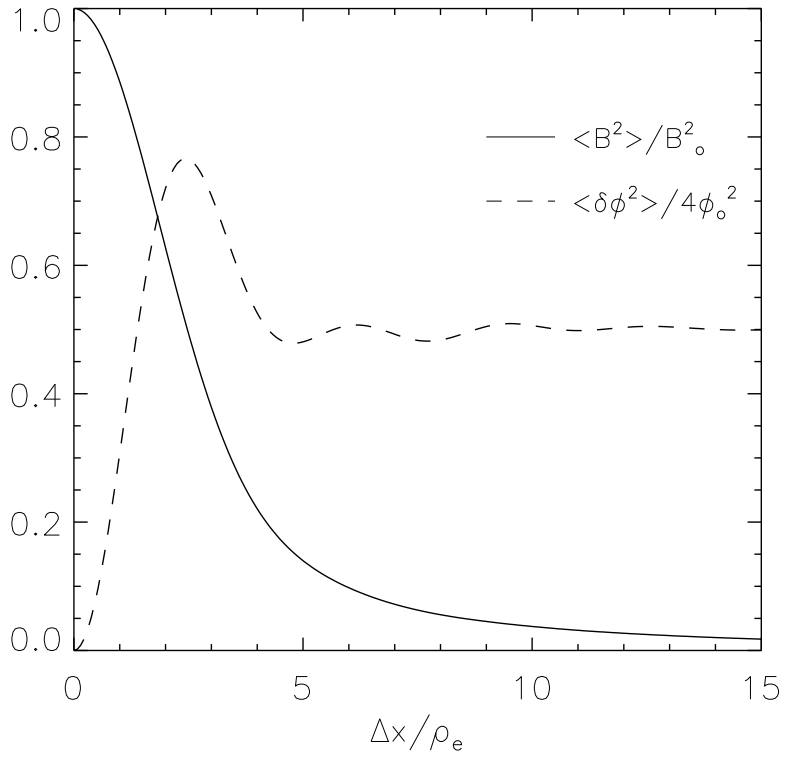

Figure 3.16: Measured total magnetic fluctuation amplitude as a function of coil size (here Δx is the coil diameter).

edge of MRX current sheets, the magnetic diagnostic might only detect 10-20% of the total fluctuation amplitude, assuming LHDI is the source of the fluctuations. In addition, it might be expected that the spectrum of the measured magnetic signals would be dominated by lower frequencies, where the coil is a more efficient detector.

Chapter 4

Measurements of fluctuations in the MRX current sheet

MEASUREMENTS OF FLUCTUATIONS in the current sheet of MRX are reported in this chapter. While fluctuations have been studied in current sheets previously, the measurements reported here are the first to be done in a current sheet formed in a plasma where the ions are magnetized ($\rho_i \ll L$) and the MHD approximation is satisfied in the bulk of the plasma ($S \gg 1$). In addition, non-classical reconnection has been identified in current sheets studied during this dissertation work, providing an opportunity to determine if turbulence plays an essential role in fast magnetic reconnection. Measurements of high-frequency fluctuations were performed in the current sheet of MRX, with the following goals: (1) Identify any instabilities present in the current sheet and determine their characteristics and (2) determine the influence of these instabilities on the process of reconnection in MRX. These measurements resulted in the first observation of the lower-hybrid drift instability in a laboratory current sheet.

This instability has been studied theoretically for decades in the context of current sheets and magnetic reconnection, yet no detailed experimental investigation of the instability has been possible until this work. The bulk of this dissertation work focused on measurements of floating potential fluctuations in null-helicity (no toroidal or guide field) current sheets in MRX. Magnetic fluctuations were also investigated during this study and those relevant to the LHDI will be discussed in this chapter, while others are discussed in Appendix B.

In Section 4.1 the observation and detailed characterization of LHDI fluctuations in MRX current sheets is presented and in Section 4.2 the role of these fluctuations in the process of magnetic reconnection in MRX is discussed.

4.1 Observation of the lower-hybrid drift instability

Measurements using amplified floating double Langmuir probes placed on the edge of current sheets in null-helicity discharges in MRX have revealed the presence of broadband fluctuations near the lower hybrid frequency. In this section, evidence supporting the identification of these fluctuations as lower-hybrid drift waves is presented. The evidence is provided by detailed studies of the frequency spectrum, radial amplitude profile, and spatial correlations and propagation characteristics of the fluctuations. These observations will be shown to compare well with theoretical predictions for the lower-hybrid drift instability, using the theory developed in Chapter 2 for comparison.

Figure 4.1 shows an example of an differential floating potential signal ($\delta\phi_f$) taken at $r = 0.34$m (refer to Figure 3.12 for measurement geometry), along with a trace of the total toroidal plasma current during a hydrogen discharge in MRX.

The plasma current rises during formation of the current sheet in MRX and then typically flattens in time during the quasi-steady period of magnetic reconnection. The fluctuations are seen to arise with the formation of the current sheet and persist for $10 - 20\mu s$. The amplitude of the measured fluctuations is typically several hundred millivolts, but can be as high as 1-2V. A normalized fluctuation amplitude can be constructed by comparing the amplitude to the measured electron temperature, $e\delta\phi_f/T_e$. This normalized amplitude is typically found to be several percent ($T_e \sim 5 - 10$eV, $e\delta\phi_f/T_e \lesssim 10\%$). A windowed FFT of the shown example signal is inset in Figure 4.1, with a vertical line marking the position of the time averaged lower hybrid frequency, $f_{LH} \sim 16$MHz. The FFT is performed using a Hanning window, $8\mu s$ wide about $t = 252\mu s$, and the plot is made using a linear vertical axis. The lower hybrid frequency is determined from measurements of the magnetic field near the fluctuation probe using $\omega_{LH} = \sqrt{\Omega_e \Omega_i}$. In MRX, current sheet

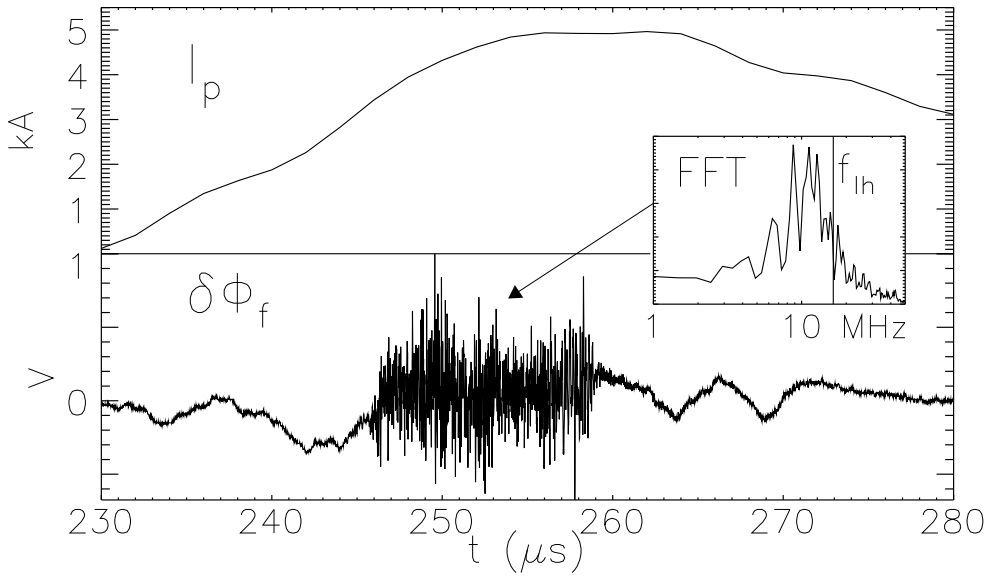

Figure 4.1: Traces of plasma current and measured floating potential signal along with an FFT of the signal. Current sheet formation and reconnection occur roughly from $t = 240\mu s$ to $280\mu s$.

formation can be prevented by shorting out (or "crowbarring") the driving coil after the poloidal field is generated, but prior to the downswing in the capacitor bank current which "pulls" flux back through the null point, resulting in a current response in the plasma. In the case that the driving coil is crowbarred and hence no current sheet is formed, no significant fluctuation amplitude is observed. Figure 4.2 shows magnetic and fluctuation data from two consecutive shots: in the first a current sheet is formed (as demonstrated by the magnetic vector plot at $t = 260\mu s$), while in the second the driving coil is crowbarred at $t = 180\mu s$, and the magnetic configuration remains "X"-like. A double floating Langmuir probe is placed at $r = 0.32$m in both cases, and significant fluctuations are only observed in the first case when a current sheet is formed.

4.1.1 Frequency spectrum

The LHDI is expected to produce fluctuations whose frequency spectrum is located near the lower hybrid frequency. The detailed dependence of the frequency spectrum of the measured floating potential fluctuations on the lower hybrid frequency was explored through varying the peak field in the current sheet and the mass of the working gas ($f_{\mathrm{LH}} \propto B/\sqrt{M}$). The peak magnetic field value was varied through raising or lowering the voltage on the capacitor bank used to generate the poloidal field. Using this technique, the peak field was scanned from roughly 100G (using 10kV/8kV on the toroidal field/poloidal field bank) to 300G (14/12 kV). Both hydrogen and helium were used as working gases, allowing for a factor of 2 change in the lower hybrid frequency due to ion mass. Figure 4.3(a) shows a set of example average floating potential fluctuation power spectra (linear vertical axis, logarithmic horizontal axis) at different local field values and with two different fill

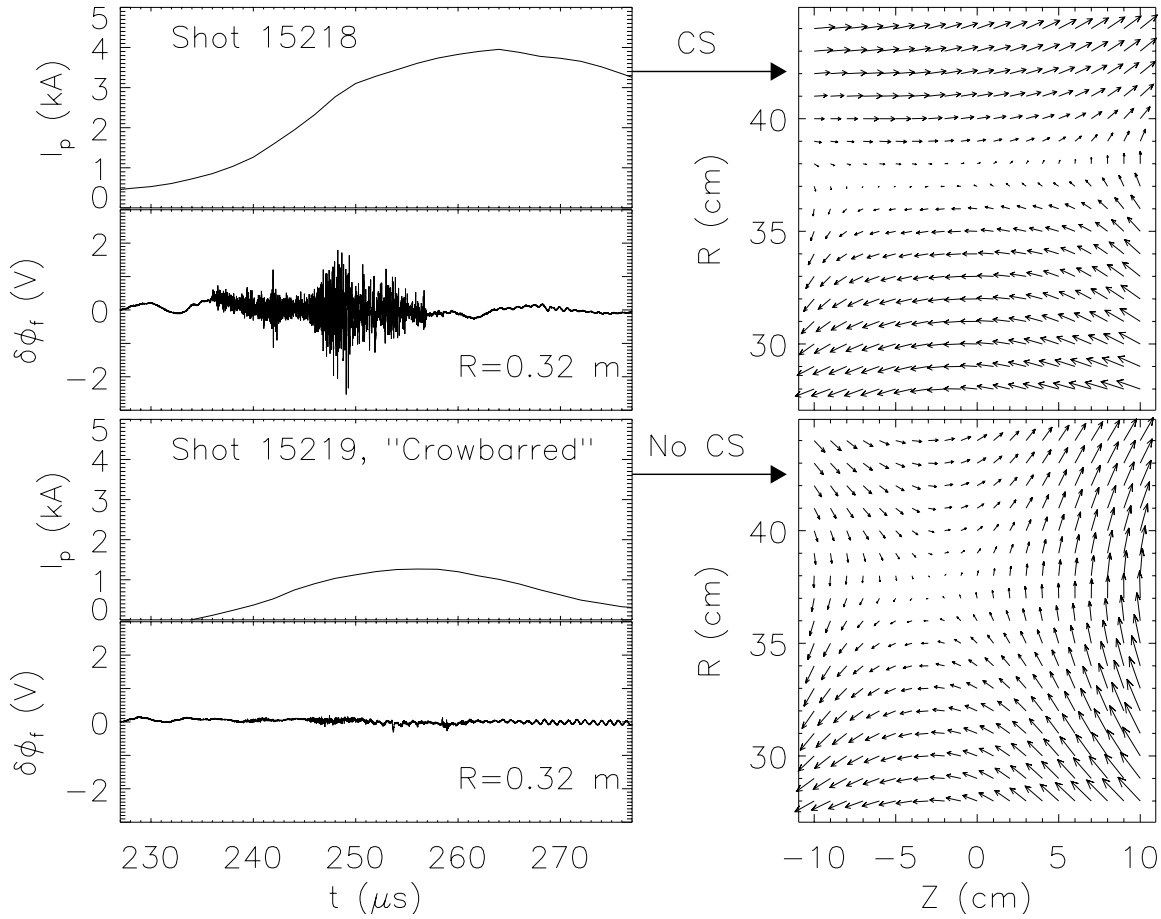

Figure 4.2: Magnetic and fluctuation measurements for two consecutive discharges. In the first, a current sheet is formed and fluctuations are observed. In the second, the driving coil is crowbarred, and very little fluctuations amplitude is observed.

gases, hydrogen and helium. Each plot is generated through averaging the spectrum of 10 discharges whose local magnetic field value falls within a 50G window of the magnetic field value annotating the graph. There is an upward shift evident in the power spectrum with increasing field strength and decreasing ion mass, consistent with the shift in the local lower hybrid frequency. Figure 4.3(b) shows a comparison between all discharges in helium and hydrogen, summed over all local field values. This figure demonstrates a clear downward shift in the frequency

spectrum of the observed fluctuations in helium discharges. Figure 4.3(c) shows the power spectrum of the fluctuations averaged over 97 discharges, including both hydrogen and helium shots, with the frequency normalized to the local lower hybrid frequency of each discharge. The averaged spectrum is quite broad, but is clearly situated near the lower hybrid frequency. Figure 4.4 shows the value of the frequency at the peak of the fluctuation spectrum versus the measured magnetic field, for discharges in hydrogen. While there is some scatter in the data, the peak frequency scales fairly consistently with the lower hybrid frequency.

The theory of the LHDI predicts that the peak of the growth rate should occur at a wavenumber associated with a real frequency of roughly the lower hybrid frequency. The observed frequency spectrum is consistent with the linear theory in this regard, as the peak is near the lower hybrid frequency. The LHDI theory also predicts a fairly wide range of wavenumbers where appreciable growth is found, as shown in Figure 2.2. The observation of a fairly wide spectrum in frequency is consistent with this linear prediction. It should also be noted that, for the most part, the observed spectrum is qualitatively similar to what might be expected of decorrelated double probe measurements – that is, the features observed in Figure 3.13(a) due to effects of a differential measurement generally aren't observed (though may be present in the high-field case).

These high-frequency fluctuations dominate the spectrum of the floating potential measurements, and no other readily identifiable features are observed in a consistent manner at any radial location. Figure 4.5 presents the average large-window ($100\mu s$) FFT of 100 floating potential measurements on the inner edge of the MRX current sheet ($0.30\text{cm} < r < 0.38\text{cm}$) in hydrogen discharges. This figure

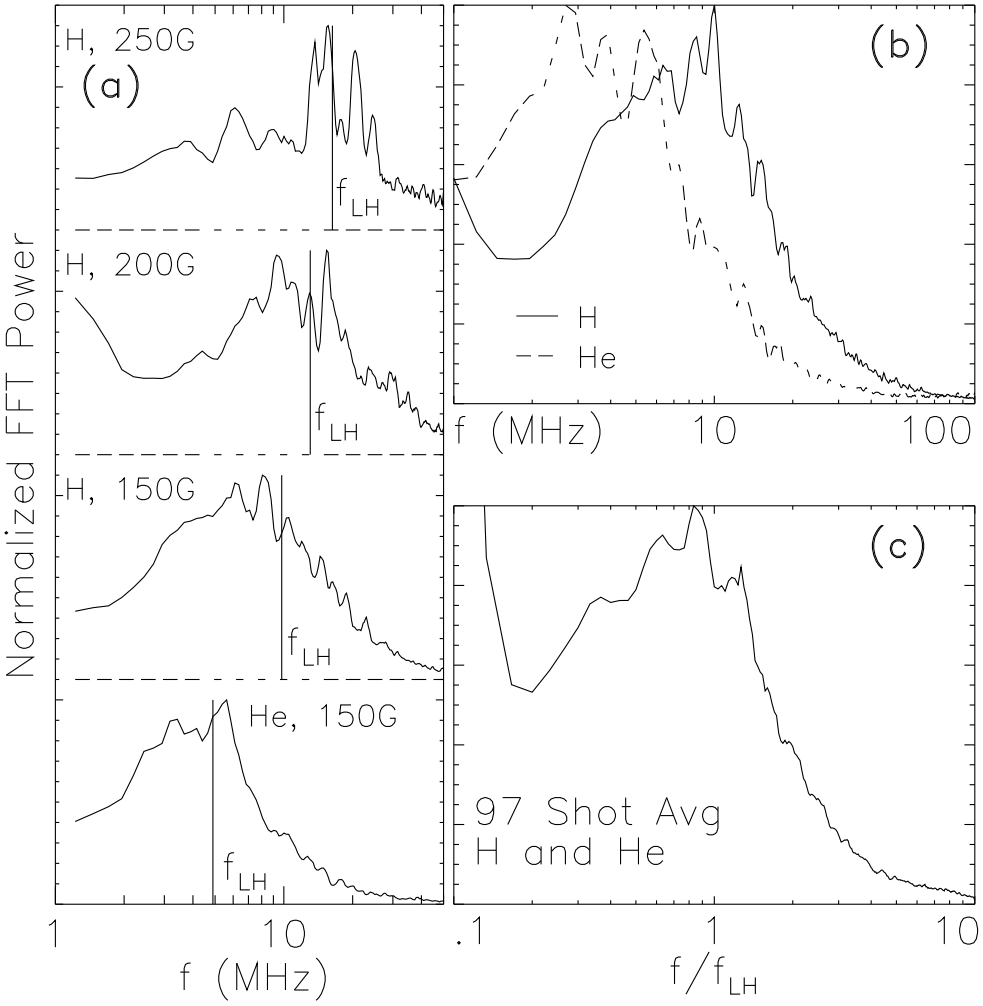

Figure 4.3: (a) Average floating potential power spectrum in helium and hydrogen at different average field strengths. (b) Comparison of fluctuation spectra in helium and hydrogen discharges, summing over all local field values. (c) Average power spectrum for 97 discharges, with frequency normalized to the local lower hybrid frequency for each discharge.

is shown to provide a broader view of the spectrum of measured floating potential fluctuations. Clearly shown in the figure is the LHDI feature extending from a few MHZ to 10's of MHz. Low frequency features in the spectrum are likely provided by MHD timescale movement of the current sheet. The coherent features near 1 MHz in the spectrum are due to ringing in the transmission lines associated

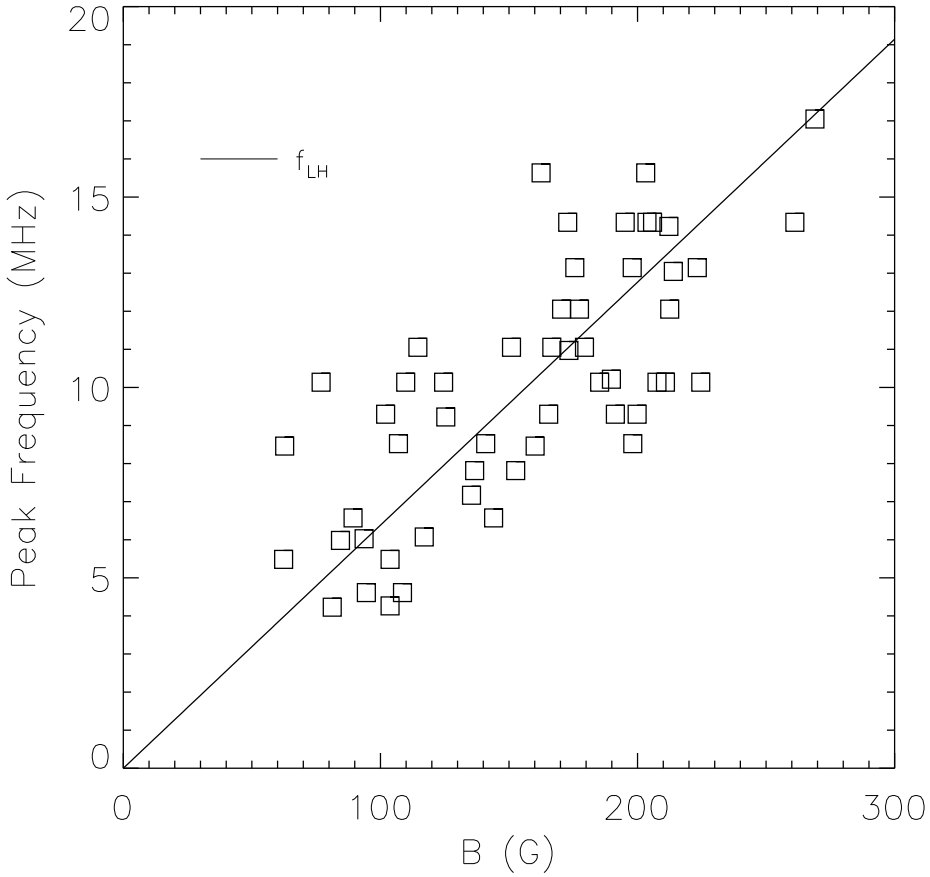

Figure 4.4: Frequency at the peak of the fluctuation spectrum versus measured local field in hydrogen. The solid line represents the lower hybrid frequency

with the capacitor bank circuitry.

4.1.2 Spatial amplitude profiles and time behavior

The LHDI is expected to be driven by density gradients and cross-field currents, which would suggest that it might be localized near these energy sources in MRX current sheets. In order to determine if the observed fluctuations are consistent with these expectations, a study of the radial amplitude profile was performed, and the results of this study are presented here. A comparison with the linear

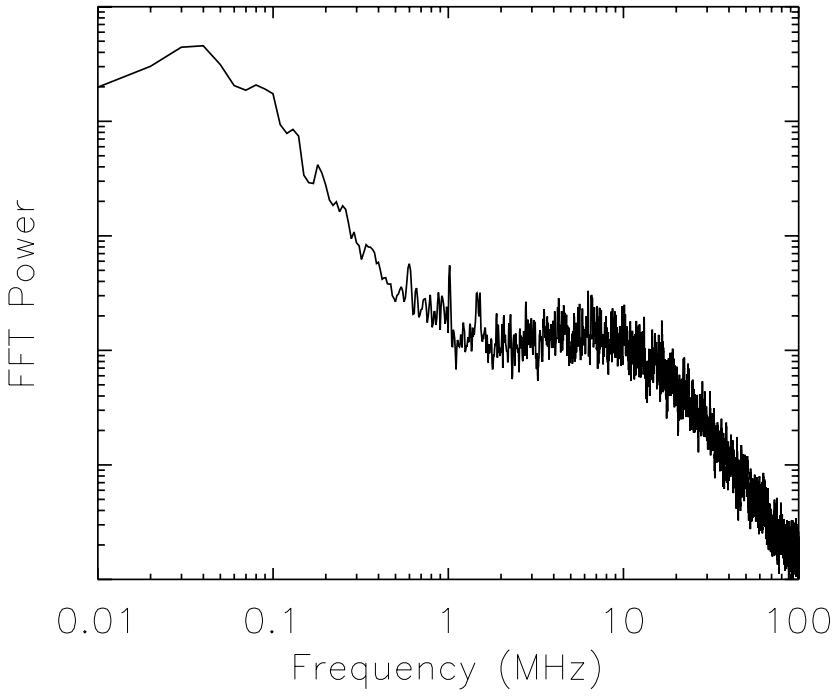

Figure 4.5: Long-time window ($t = 100\mu s$) FFT power averaged over 100 measurements.

theory developed in Chapter 2 is presented, and provides further support for the conclusion that the measured fluctuations are due to the LHDI. A discussion of the observed time behavior of the fluctuations, also based on the linear theory, is provided.

Radial amplitude profile measurement

Radial profiles of the amplitude of the floating potential fluctuations were constructed through shot-to-shot positioning of the probe and averaging over many shots at each position. Figure 4.6 shows average radial profiles of the root-mean-square fluctuating floating potential amplitude superimposed on the computed average current density profile at four times during a set of more than 200 low-collisionality ($\lambda_{mfp}/\delta \sim 5 - 10$) MRX discharges (12/10 kV, 4 mT fill pressure,

hydrogen). The current densities shown are computed by first fitting the average measured magnetic field profile to a Harris sheet profile, then deriving the current density from the fit. The magnetic measurements shown are made at a small toroidal separation ($10 - 15^{\circ}$) from the fluctuation diagnostic. As the current sheet is formed, the width of the sheet thins to be comparable to the ion skin depth while the radial position of the current sheet moves outward (due to the hoop force) in order to establish equilibrium with the applied equilibrium field. The plotted fluctuation amplitude is determined through first high-pass filtering individual fluctuation measurements at 1 MHz (digitally), then averaging the square amplitude at each radial position. The error bars represent shot-to-shot variations in the measurement. The fluctuations are observed to grow up on the inner edge of the current sheet, then strengthen and track the current sheet as it moves toward an equilibrium position. Later in time, the amplitude decays fairly rapidly even though the current sheet persists and reconnection continues. Individual realizations of the fluctuation amplitude (such as shown in Figure 4.1) depend on the placement of the probe and the motion of the current sheet relative to the probe. The timescales present in individual signals are therefore a combination of the motion of the unstable region toward or away from the probe and the global timescales for the fluctuation amplitude shown in Figure 4.6.

Figure 4.7 shows a contour plot in the $r - t$ plane of the rms floating potential amplitude, along with the trajectory of the center of the current sheet and sheet thickness (R_o and $R_o \pm \delta$, determined from the fit of the average magnetic field to a Harris profile). This figure shows in more detail how the fluctuation amplitude follows the trajectory of the current profile. As reconnection proceeds, the equilibrium is altered by the depletion of flux inside the current sheet. This lowers the B^2

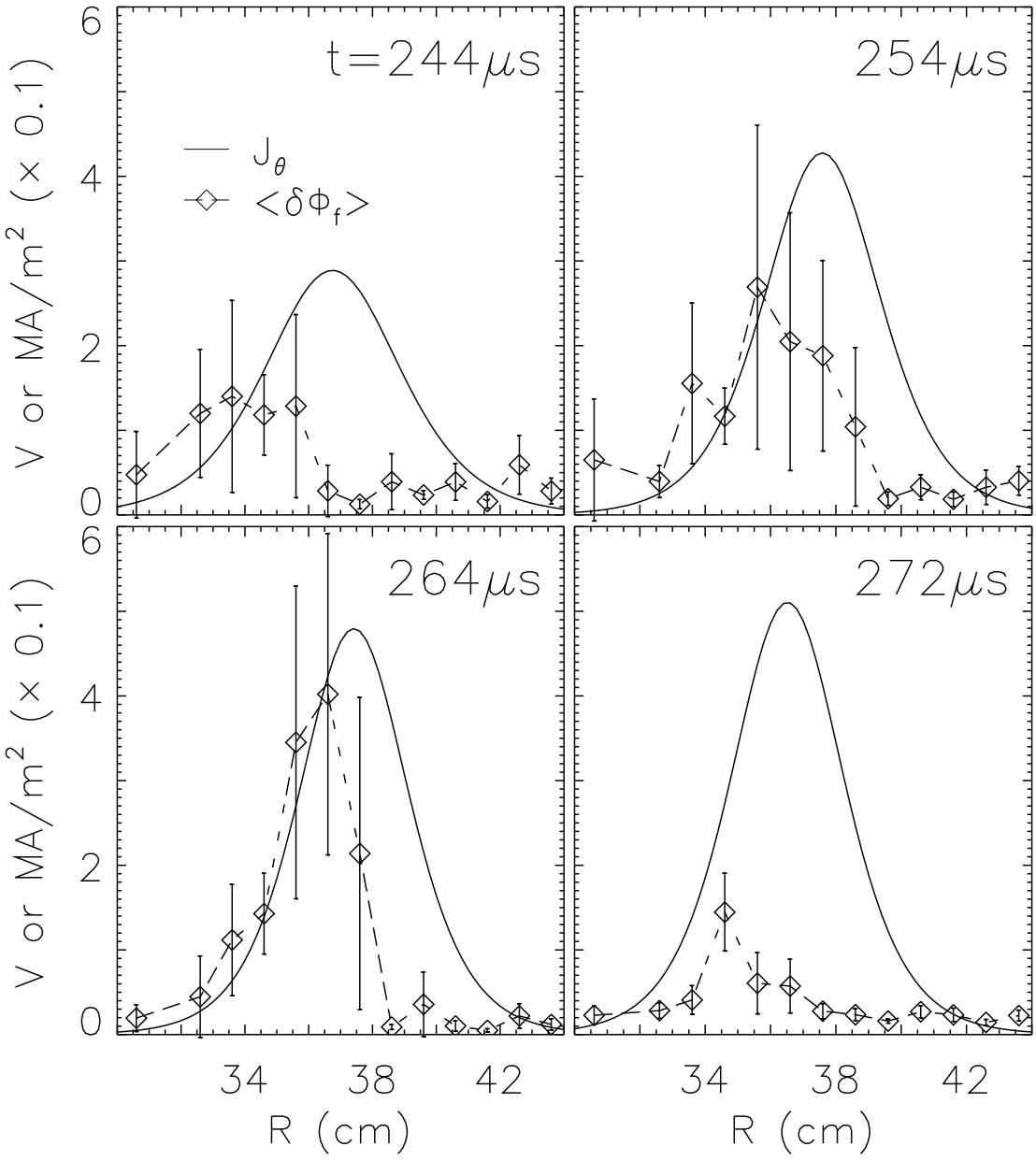

Figure 4.6: Radial profiles of rms fluctuation amplitude at $z = 0$ and current density in the MRX current sheet at four times.

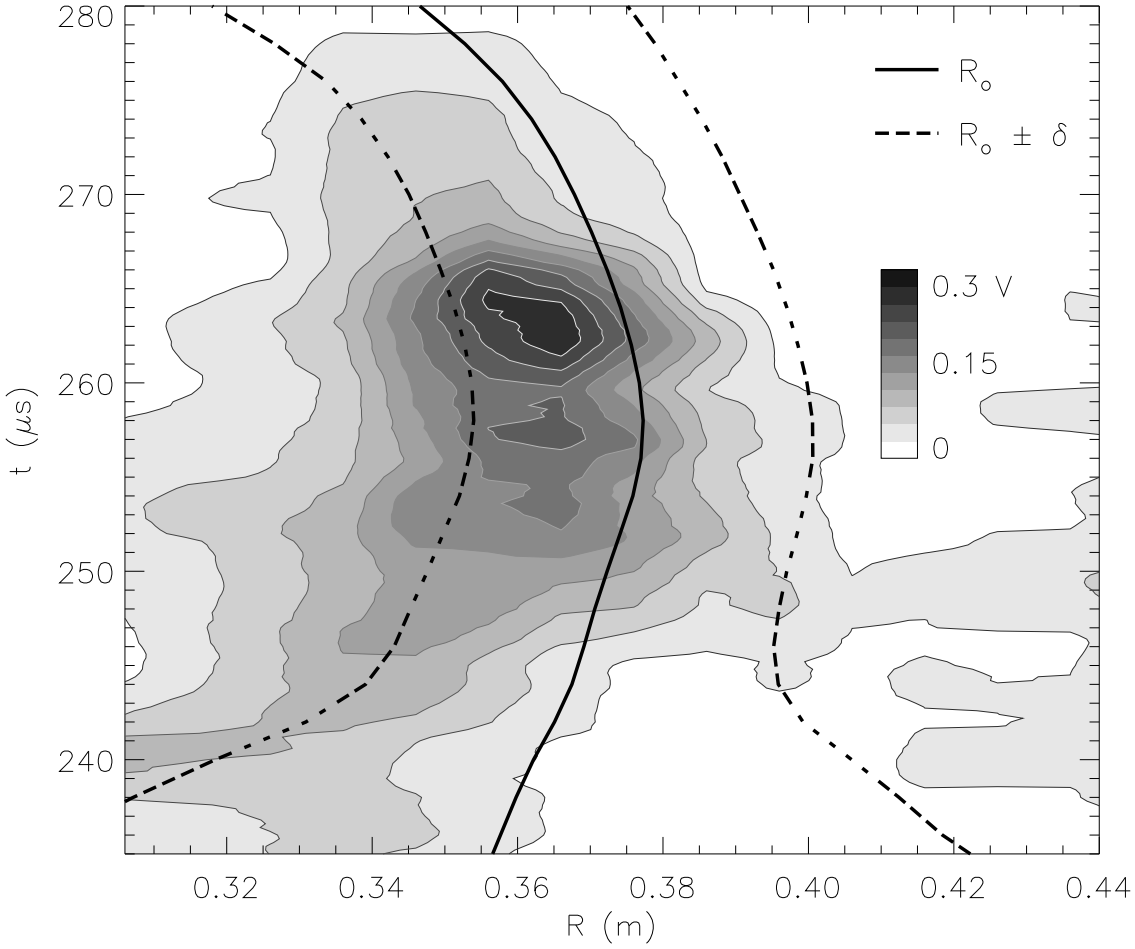

Figure 4.7: Contours of rms fluctuation amplitude in the $r - t$ plane. Superimposed is the trajectory of the current sheet center (R_o) and the current sheet thickness ($R_o \pm \delta$).

pressure pushing out on the current sheet, resulting in an inward shift of the equilibrium position, as shown in the figure after $t \approx 258\mu s$. Reconnection continues as the current sheet moves inward, until roughly $t = 280\mu s$.

Comparison with LHDI theory

The radial profile measurements raise a key question: Why is the radial amplitude profile asymmetric? We will address this question using the linear electrostatic model of the LHDI derived in Chapter 2. Linear calculations of the local growth rate profile of the LHDI were performed based on measured profiles of density, electron temperature and magnetic field. Electron temperature and density profiles were acquired in a similar fashion to the fluctuation profile: through shot-to-shot positioning of a triple Langmuir probe and averaging over several shots (at least 10) per position. The triple Langmuir probe measured density profile at $t = 264\mu s$, along with a Harris sheet fit to the measured average magnetic field profile, is shown in Figure 4.8(a). Both the magnetic field and the density are observed to be radially asymmetric with respect to the center of the current sheet. The magnetic field asymmetry is due to the cylindrical geometry of the field coils (flux cores) in MRX, which generate stronger fields inside the current sheet location than outside. The density asymmetry arises so that radial force balance can be achieved with this magnetic field profile [YAMADA *et al.*, 2000]. The density gradient is a source of free energy for the LHDI, and a stronger gradient on the inner edge implies the growth rate should be larger there. In addition, the density gradient creates an radially asymmetric cross-field electron-ion flow speed difference, $V_d = j/ne$. This cross-field drift is also an important drive for LHDI, and for a symmetric current density, the larger density on the outer edge produces a

smaller flow difference between the ions and electrons. The combination of the density and magnetic field asymmetries produces a strong asymmetry in the profile of the electron beta ($\beta_e = 8\pi n T_e / B^2$), as shown in Figure 4.8(b). The beta on the inner edge of the current sheet is on the order of 10%, compared to the outer edge which has near unity beta. The large beta on the outer edge should be a significant stabilizing influence on the LHDI.

In order to compute a profile of maximum LHDI growth rate, a smooth fit to the density profile measurement (dotted line in Figure 4.8(a), arbitrarily using a Lorentzian with different "temperatures" on either side of the current sheet) along the fitted magnetic field and current profiles at $t = 264\mu s$ were used to compute parameters in Equation 2.3 (assuming $T_i/T_e = 1, 2, 3$). The cross-field ion velocity (V) in this equation was determined by equating the plasma current density to $j = ne(V + v_{D,e})$, where $v_{D,e}$ is the electron diamagnetic velocity. Dispersion relations and growth rates for the LHDI were then found through numerically finding roots of Equation 2.3, using model parameters determined from measured plasma parameters at each radial location. Figure 4.8(d) shows the profile of the maximum growth rate (maximized over wavenumber) which resulted from these calculations. The predicted growth rate profile is quite asymmetric, in fact growing modes are only found on the inner edge of the current sheet. Growth is suppressed on the outer edge by the large beta and low ion drift speed and small normalized density gradient. The growth rate profile compares well with the measured fluctuation amplitude profile at $t = 264\mu s$, which is repeated in Figure 4.8(c) for clarity. There is no reason to expect quantitative agreement between the saturated amplitude of the fluctuations and the linear growth rate in this case. However, the linear growth rate profile should indicate where the drive for the instability is strongest

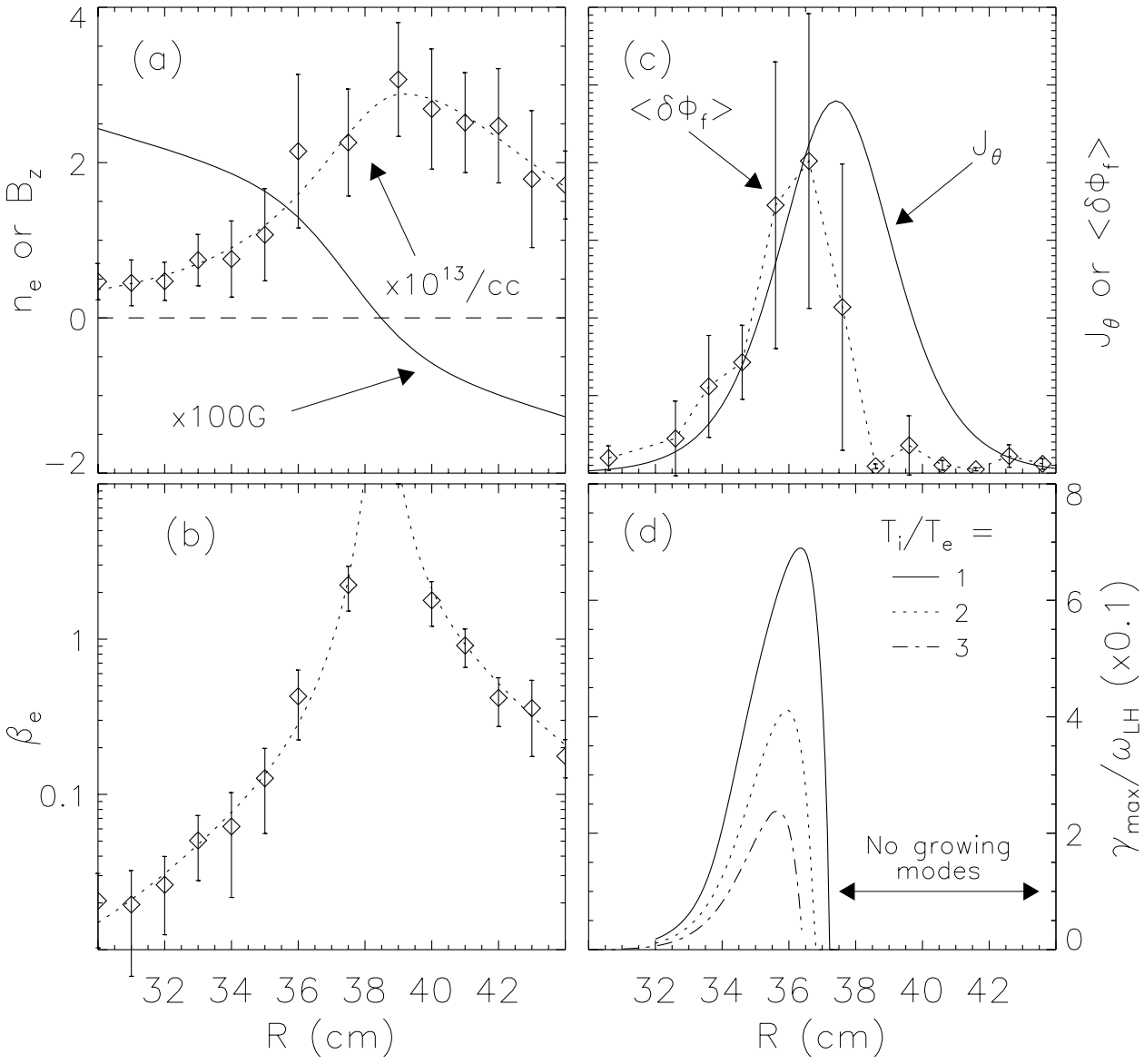

Figure 4.8: (a) Radial profiles of fitted average magnetic field and density, including a smooth fit to the density profile (two-temperature Lorentzian). (b) Electron beta calculated from measured electron density, electron temperature, and magnetic field. (c) Fluctuation amplitude and current density profiles at $t = 264\mu s$. (d) Computed peak growth rate profile for the LHDI, for the measured profiles and for $T_i/T_e = 1, 2, 3$.

and hence should suggest the saturated amplitude might be largest.

The radial profiles shown in Figure 4.6 seem to suggest that some penetration of the LHDI into the magnetic null is observed in these measurements. However, It is important to note that the peak of the current density is slightly offset from the magnetic null early in the reconnection process in MRX, due to the asymmetries inherent in the cylindrical geometry in MRX. This is demonstrated in Figure 4.9, where profiles of fitted magnetic field, fit-derived current density, and measured fluctuation amplitude are plotted. From this figure, the fluctuation amplitude does

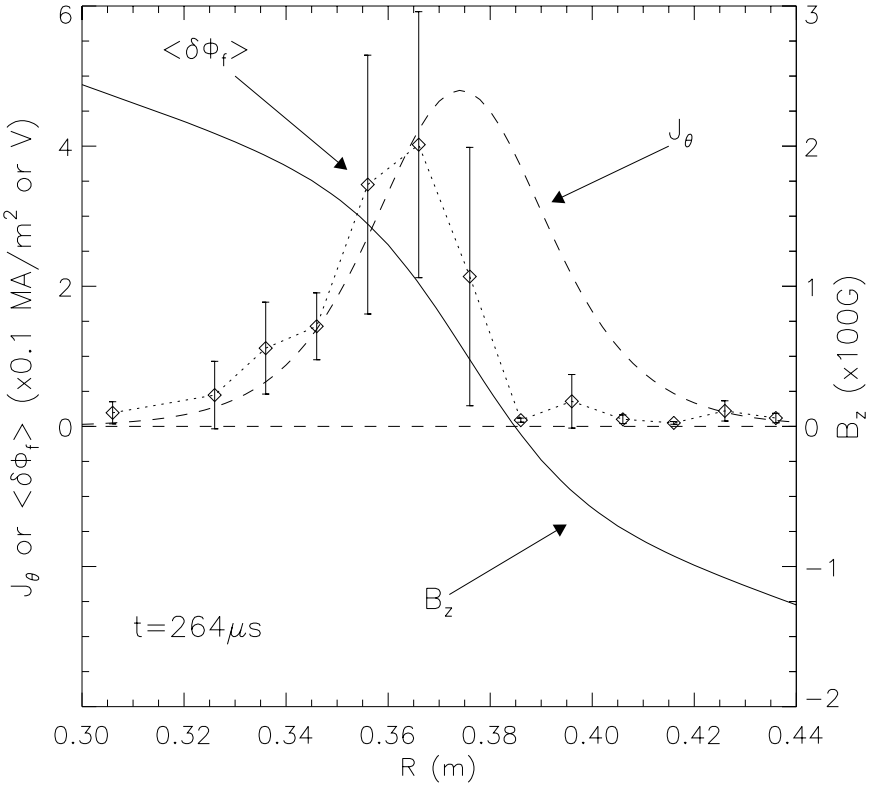

Figure 4.9: Profiles of magnetic field, current density, and fluctuation amplitude at $t = 264\mu s$, demonstrating that no significant penetration of the LHDI into the magnetic null is observed.

not penetrate into the null, consistent with linear theoretical predictions of beta stabilization. The peak of the current density and the magnetic null move closer

in MRX and eventually coincide as reconnection continues and the current sheet becomes more symmetric late in time [YAMADA *et al.*, 2000].

Discussion of amplitude time behavior

The amplitude of the fluctuations in this set of discharges is observed to decrease rapidly shortly after $t = 265\mu s$. The radial profiles of measured plasma parameters change fairly smoothly by comparison, and therefore do not seem to provide an answer for the rapid timescale of the decrease. Figure 4.10 shows radial profiles of electron density and electron beta, along with smooth fits to the data, near the time of peak amplitude ($t = 264\mu s$) and at a later time, after the amplitude decrease ($t = 274\mu s$). The profiles are observed to be quite similar, with a slight decrease in density and a slight increase of electron beta on the inner edge of the current sheet due to decrease in the local magnetic field during reconnection. One unknown parameter in these experiments in hydrogen is the ion temperature. It is expected that the ions should be heated and the ion temperature should rise monotonically during reconnection, based on measurements in helium plasmas [HSU *et al.*, 2001] (see Figure 1.7). This ion heating could increase the T_i/T_e ratio and also increase the total plasma beta. DAVIDSON *et al.* [1977] have shown that at normalized drift speeds $V_d/v_{th,i} \gtrsim 1$ the critical beta at which the LHDI is suppressed can drop with increasing T_i/T_e. Figure 4.8(d) shows some support for this in MRX parameter regimes as the calculated linear growth rate drops with increasing T_i/T_e. We expect that the ion temperature should be less than the electron temperature before reconnection begins, again based on previous measurements in helium. An estimate of the ion temperature at late times can then be made through considering an MHD force balance across the current sheet. The MHD momentum equation,

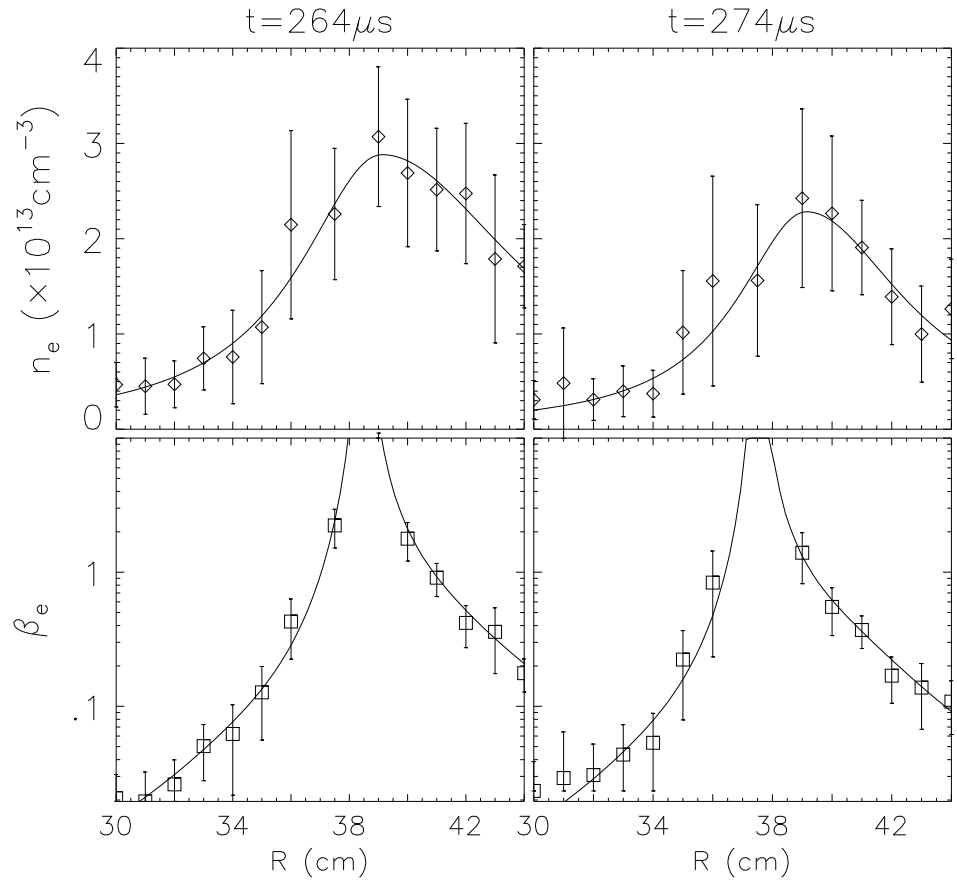

Figure 4.10: Radial profiles of electron density and electron beta at $t = 264\mu s$ and $t = 274\mu s$.

assuming steady state and negligible flow speeds can be simply written:

$$\frac{\mathbf{j} \times \mathbf{B}}{c} \approx \nabla p \tag{4.1}$$

The flow speeds along $z = 0$ during steady state reconnection in MRX are a small fraction of the Alfvén speed, typically $v/v_A \lesssim 10\%$. These flows are energetically dominated by the magnetic field and plasma pressure and therefore the radial force balance should be well described by Eqn 4.1. Integrating the momentum equation over radius in MRX, starting from $r_o = 0.28$m where $\mathbf{j}$ is small, we find:

$$\Delta p \approx \int_{r_o}^{r} j_\theta B_z dr \tag{4.2}$$

Figure 4.11 shows an application of Eqn. 4.2 at $t = 274\mu s$. The measured electron pressure is insufficient to support an equilibrium with the magnetic field, and the unmeasured ion pressure must make up the difference. The total plasma pressure calculated assuming the ion temperature is twice the electron temperature is shown and is found to be comparable to the integrated magnetic force, suggesting that $T_i/T_e \gtrsim 2$ at this point in time. The linear growth rate should drop somewhat

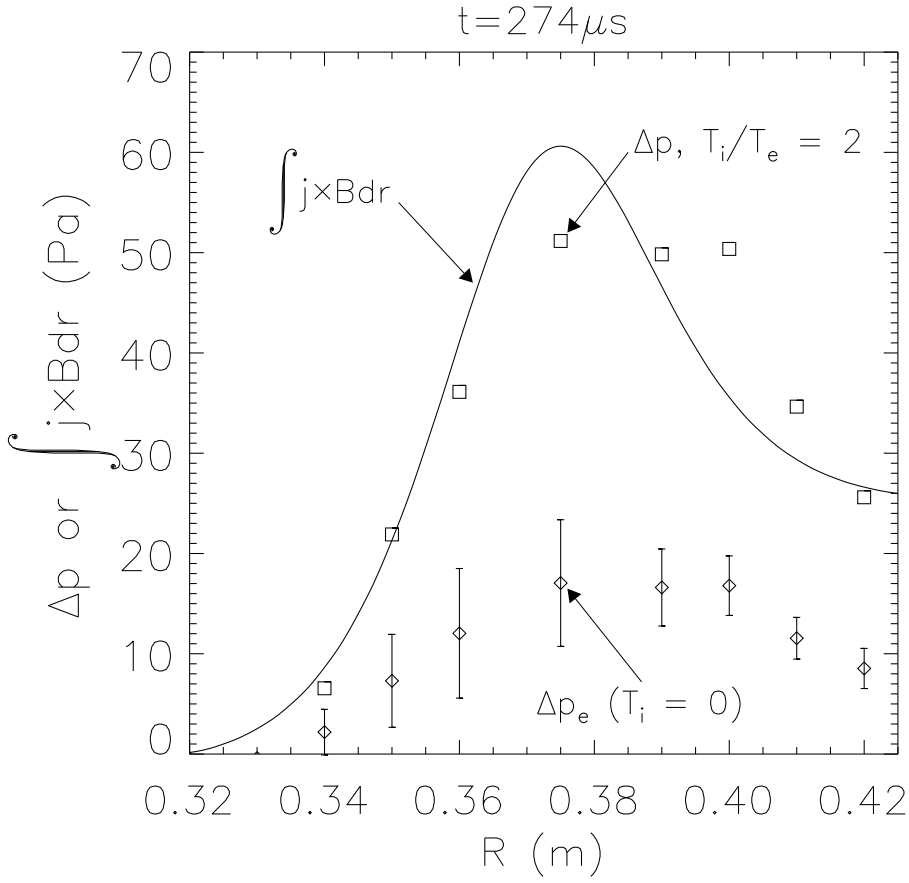

Figure 4.11: Comparison between integrated $j \times B$ force and electron pressure and total pressure for $T_i = 2T_e$.

due to an increase in the temperature ratio to $T_i/T_e \sim 2$ (see Figure 4.8), but this may not fully explain the observed greater than four-fold drop in the fluctuation

amplitude.

We can offer some additional suggestions as to the source of the rapid decrease of the fluctuation amplitude observed in these discharges. A nonlocal theory is likely to be necessary to fully describe the LHDI in MRX current sheets, due to the presence of gradients in both the r and z direction. In particular, it is important to note that the local theory assumes that the strongest growing mode occurs at $k_{\parallel} \sim 0$, or at infinite parallel wavelength. The current sheet in MRX is, of course, of finite length, and largest parallel wavelength is likely set by this length. It is possible that plasma conditions away from the center of the current sheet (along z) could have repercussions on the behavior of the instability near the center of the current sheet, due to the tendency for the instability to grow at large parallel wavelength. For instance, it is known that the plasma pressure downstream in the MRX current sheet builds up during reconnection [Ji *et al.*, 1999], and this might lead to large downstream beta. This beta might stabilize the LHDI at large z, limiting the $k_{\parallel}$ available for modes driven at the center. This effect, coupled with rising beta and T_i/T_e at the center, could possibly result in the observed rapid drop of LHDI amplitude near the center of the current sheet for the given parameters. Flows that develop during the reconnection process could result in convection of unstable LHDI fluctuations away from the unstable site, which could possibly explain the drop in amplitude with time. However, spectroscopic and probe-based flow measurements in MRX have indicated that flow rates during reconnection are small compared to the Alfvén or ion thermal speed (roughly 10% of these values) [Hsu, 2000]. This fact, coupled with the strong predicted growth rate for the LHDI, suggests that convection of unstable waves should not be a large sink of fluctuation energy compared to the local input from the linear growth rate. An additional

possible explanation is that the observed time behavior is due to a nonlinear phenomenon. The saturation mechanism for the LHDI could be effected by changing parameters in the current sheet, and might result in a lower saturated amplitude. Finally, a comment on the effects of wave coherence on the double probe measurement should be offered. As shown in Figure 3.13(b), one might expect a reduction in the response of the probe at very small normalized separation, $\Delta x/\rho_e$. The electron gyroradius does get larger due to a slow drop in the magnetic field, however, this change (roughly a 20% drop in the field strength from $t = 264\mu s$ to $t = 274\mu s$, making $\Delta x/\rho_e$ drop from roughly 5 to roughly 4) is not sufficient to push the probe response into the severely damped region (assuming the probe tips are not decorrelated). At the same time, if this was the case, any magnetic fluctuation amplitude might get stronger. Preliminary magnetic measurements presented later in this chapter and in Appendix B show that this is very likely not the case.

4.1.3 Spatial correlations and propagation characteristics

The linear theory provides predictions for wavelength and phase velocity of the LHDI, and further evidence for the presence of this instability in MRX could be provided through comparing measured spatial correlations in the fluctuations with the theoretical predictions. In this section, studies of the decorrelation length in the measured fluctuations are presented along with statistical dispersion relations derived from the cross-spectrum of two spatially separated differential probes.

Spatial correlations in the fluctuations were investigated using spatially separated double floating Langmuir probes. Three probes were constructed for this purpose, with probe-to-probe spacings of 1, 3.5, and 10 mm. The decorrelation

length in the fluctuations was investigated through calculating the coherency between separated differential probe signals, which is defined as:

$$\gamma = \frac{|\mathcal{X}_{a,b}|}{\sqrt{|\delta\tilde{\phi}_{f,a}|^2 |\delta\tilde{\phi}_{f,b}|^2}}$$

Where $\delta\tilde{\phi}_{f,a}$ is the Fourier transform of signal **a**, and $\mathcal{X}_{a,b} = \delta\tilde{\phi}_{f,a}\delta\tilde{\phi}_{f,b}{}^*$ is the cross spectrum of signals **a** and **b**. Figure 4.12 shows the mean coherency, averaged over the LHDI feature in the frequency spectrum and over 20 discharges per separation, versus probe separation (normalized to the electron gyroradius). Here the separation, Δx is in the toroidal direction, which is the current direction and the expected propagation direction for the LHDI.

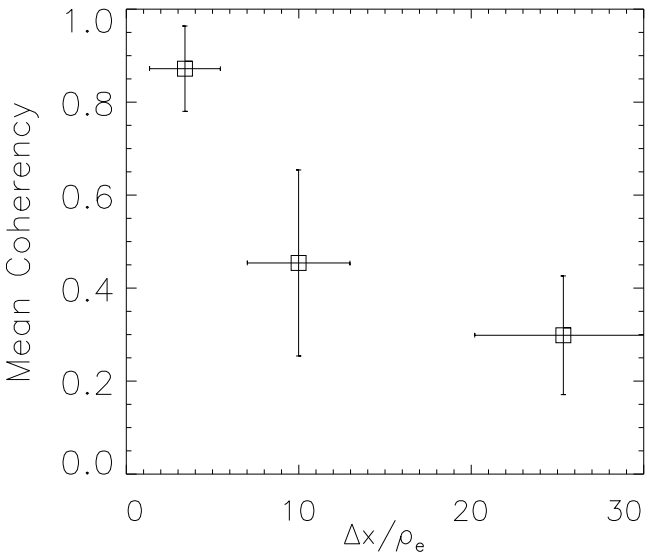

Figure 4.12: The mean coherency of spatially separated measurements of LHDI fluctuations in MRX.

The signals are quite coherent at the smallest separation (1 mm), but the coherency drops rapidly as the separation becomes larger. A decorrelation length for the turbulence can be estimated as the length at which the coherency drops to

$1/e$. From Figure 4.12, a decorrelation length $L_c \lesssim 10\rho_e$ is estimated. This length is comparable to the theoretically predicted wavelength for the strongest growing portion of the LHDI spectrum ($\lambda \sim 2\pi\rho_e$). This estimate implies that significant new growth occurs over a single wavelength, an implication which is consistent with the predicted strong linear growth rate for the LHDI ($\gamma \sim \omega_{LH}$). This measurement also suggests that the probe tips of the 3 mm separated probe (which was used for single point measurements in the turbulence) should be decorrelated, and that coherent effects due to the wavelength of the waves (discussed in Chapter 3) should not significantly effect the measured spectrum.

Statistical dispersion relations of the fluctuations in the 1 mm separation case were obtained using the statistical method of BEALL *et al.* [1982], which was reviewed in Chapter 3. The computation was performed using three sets of data, each with different probe orientations with respect to the magnetic field. The first two orientations were perpendicular to the magnetic field, one with the probe oriented in the electron diamagnetic direction and the second with the probe oriented in the ion diamagnetic direction. The distinction between these two orientations is made by labeling one of the two probes as primary (call it probe **a**, for instance), and orienting the two probes such that probe **a** is upstream with respect to the second probe in a flow in either the ion or electron diamagnetic direction. This distinction is made primarily as a test for any systematic asymmetries in the probes – if the two probes make measurements in an identical fashion, rotating the probe should result in a positive measurement of k in the wave propagation direction and a negative k measurement when oriented in the opposite direction. The dispersion relations resulting from orientations in the electron (labeled 0°) and ion (labeled 180°) diamagnetic directions are shown in Figure 4.13. The phase velocity derived

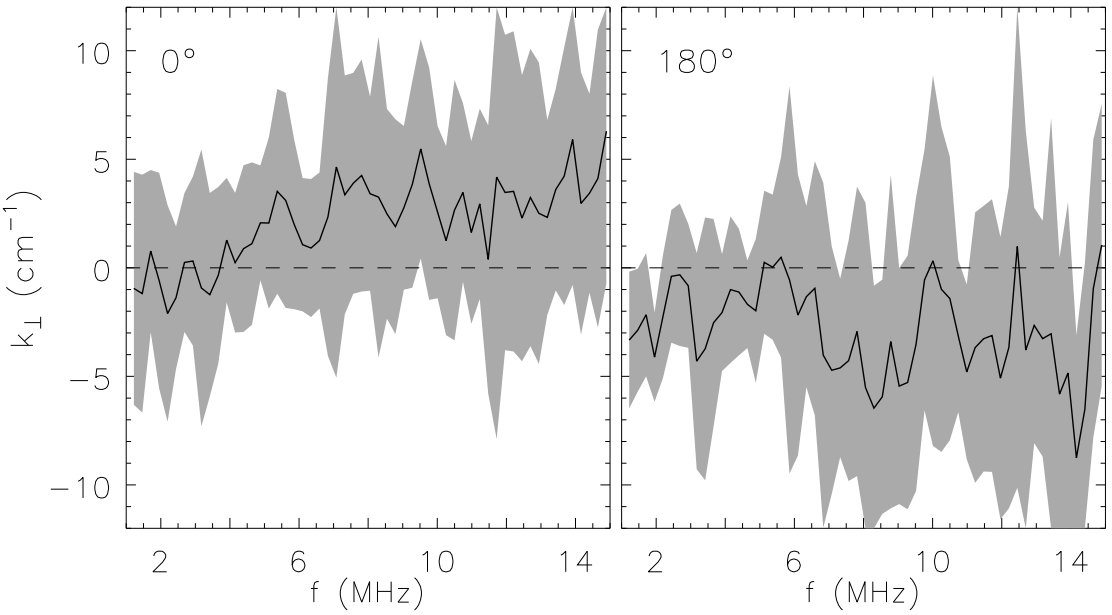

Figure 4.13: Statistical dispersion relations for two probe orientations (0°/180° = electron/ion diamagnetic direction).

from this figures is quite high, $v_\phi \sim 125$ km/s, compared to an expected phase speed near the ion thermal velocity ($v_{\text{th,i}} \sim 30$ km/s). The gray regions surrounding the black $k_\perp$ curves represent the spectral width of the $k_\perp$ calculation, which is quite large. The spectral width represents the spread in measured $k_\perp$ and the size of this spread is due to the observation of, on average, a large spread in the phase shift in the cross spectrum at each frequency in the turbulence. This fact precludes a statistically significant determination of the wavelength and phase velocity of the fluctuations. However, a preference for propagation in the electron diamagnetic direction is revealed by the measurement of primarily positive $k_\perp$ for orientation in the electron diamagnetic direction, and negative $k_\perp$ for the opposite direction. This direction of propagation is consistent with the LHDI when observed in the ion rest frame. Spectroscopic ion flow velocity measurements have been performed in

the MRX which suggest that the ion rest frame is the correct lab frame in the current sheet [Hsu *et al.*, 2001]. The LHDI is expected to propagate primarily in the toroidal direction in MRX, and should have rapid phase velocity, small k, and no preference for propagation direction along the field. A computation of the dispersion relation for the case with the probes oriented along the magnetic field is shown in Figure 4.14. While the spectral width of this $k_{\|}$ calculation is also quite large, the measurement reveals small $k_{\|}$ and no sign of preference for direction of propagation.

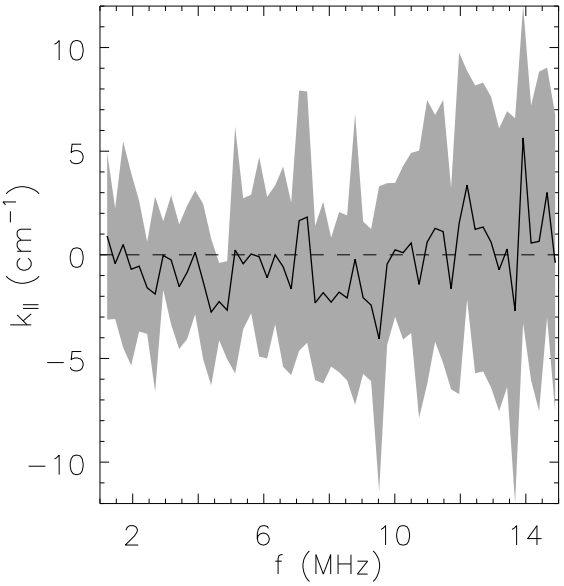

Figure 4.14: Statistical dispersion relation for probe orientation along the magnetic field.

The spectral width of these wavenumber measurements could be due to several reasons, including deficiencies in the measurement technique and effects in

the plasma. One possible deficiency in the measurement technique is the uncertainty in the instantaneous direction of the magnetic field during the measurement. The value of B_z is locally determined (within a few cm using the 1D magnetic probe), however the radial and toroidal fields are measured on the other side of the torus (approximately 180° away in toroidal angle) and may not accurately represent the fields in the toroidal plane of the fluctuation measurement. This may lead to projection effects which would make the wavelength appear longer, but the effect should be proportional to $\cos\theta$ and may not be large enough to explain the observed width. In addition, if there is some k_r to the wave, which we have assumed is zero in the theory presented in Chapter 2, we may be only measuring a projection of $k_\perp$ in the toroidal direction. This would lead to a smaller estimate for the wavenumber and a faster apparent phase velocity, consistent with the observations. Non-local treatment of the LHDI in a Harris sheet reveals radial eigenmodes, each of which has a slightly different dispersion relation [YOON, 2001]. Several of these eigenmodes are likely to be excited in the MRX current sheet, which could result in the appearance of a broad range of wavenumbers at each frequency in the turbulence. An additional linear effect which might lead to the observations is the variation of the dispersion relation with $k_\parallel$. Figure 2.2 shows the predicted dispersion relations for MRX relevant parameters and for several values of $k_\parallel$. Over the range of $k_\parallel$ shown, the phase velocity of the LHDI varies around a factor of 2 at the peak of the growth. LHDI modes with various $k_\parallel$ might be expected in MRX, and this could lead to the difficulty in determining the phase velocity of the waves. One final possible explanation based on linear theory is that the ion flow rate in the current sheet is not exactly zero and perhaps even varies with time. As shown in Chapter 2, in the electron rest frame, the dispersion relation for the LHDI can be

multi-valued, resulting in two different wavelength values at a single frequency. If the ions are not at rest in the lab frame, this type of effect might contribute to raising the measured spectral width in the turbulence. Nonlinear effects may also contribute to the observed spectral width. The LHDI has a fairly strong predicted linear growth rate in MRX, which is comparable to the real frequency (a prediction supported by decorrelation length estimates). It is therefore not unreasonable to expect rapid nonlinear saturation of the instability and nonlinear modifications to the wavelength spectrum of the turbulence. The linear characteristics of the instability, such as the phase velocity, may not be preserved in the nonlinearly saturated state, and this may be reflected in the measurement.

4.1.4 Comments on the saturated amplitude

In Chapter 2 a brief review of saturation mechanisms for the LHDI was offered, including plateau formation, current relaxation, trapping, electron resonance broadening, and nonlinear mode-mode coupling. Although collisional dissipation is not enough to explain the rate of reconnection in these discharges, sufficient collisions are available such that plateau formation and trapping might not be effective. In addition, the simulations reviewed in Chapter 2 suggest that electron dissipation is responsible for saturating the LHDI, and that ion trapping should not be important. We will therefore compare the measured amplitude of the fluctuations to the theoretical predicted saturated amplitude due to two models presented in Chapter 2: electron resonance broadening ([HUBA *et al.*, 1978], Eqn. 2.4) and nonlinear mode-mode coupling ([DRAKE *et al.*, 1984], Eqn. 2.5). The peak amplitude (in both space and time) observed in the radial scan presented Section 4.1.2 is roughly $\langle \delta\phi_f \rangle_{max} \sim 0.6V$ (note that in Figure 4.6 the amplitude is averaged over $2\mu s$ as

the resolution of the magnetic data is limited to that timescale). In Section 3.3.2 of the previous chapter, a discussion on the effect of coherent waves on a differential potential measurement was presented, showing that the expected average square amplitude of the differential measurement should be roughly twice the actual amplitude, assuming the probe separation was $\Delta x/\rho_e \gtrsim 3$[1]. The electron gyroradius at the position of peak amplitude at $t = 264\mu s$ in Figure 4.6 is $\rho_e \sim 0.6$mm, making $\Delta x/\rho_e \sim 5$, large enough that this estimate should apply. Therefore, we will assume that our differential measurement of $\sqrt{\langle \delta\phi_f^2 \rangle /2} \sim \sqrt{\left\langle \phi_p^2 \right\rangle} \approx 0.40V$ indicates normalized plasma potential fluctuation value of ($T_e \approx 8$eV):

$$\frac{e\left\langle \phi_p \right\rangle_{max}}{T_e} \sim 5\%$$

The electron resonance broadening model predicts a value for the normalized fluctuating electric field energy density, $\mathcal{E}/nT_i$, where $\mathcal{E} \approx \tilde{E}^2_{max}/8\pi = k^2_{max}\left\langle \phi^2 \right\rangle_{max}/8\pi$, which we now need to calculate. As was discussed in the previous section, a statistically significant value for the mode wavelength was not measured, however we can estimate the wavenumber in these fluctuations from the linear theory, $k \sim \rho_e^{-1}$. Using this estimate, we find that the peak fluctuating electric field value, based on $\phi \sim 0.40V$ and $k \sim \rho_e^{-1} \sim 1700m^{-1}$, is $\tilde{E} \sim 700$ V/m. Using this estimate and $n \sim 2.5 \times 10^{13}\text{cm}^{-3}$ and $T_i \sim T_e \sim 8$eV, we find that in these measurements:

$$\frac{\mathcal{E}_{max}}{nT_i} \sim 7 \times 10^{-8}$$

Now we can compute the predictions, based on measured plasma parameters, of the electron resonance broadening and nonlinear mode coupling saturation models for comparison. The electron resonance broadening model predicts, using

[1]The linear growth rate spectrum used in this calculation is the spectrum at the peak of the radial growth rate profile shown in Figure 4.8(d)

$n \sim 2.5 \times 10^{13}\text{cm}^{-3}$, $T_\text{i} \sim T_\text{e} \sim 8$ eV, $B \sim 100$G (at $r \approx 0.36$cm):

$$\left(\frac{\mathcal{E}}{nT_\text{i}}\right) \approx \frac{2}{5}\frac{m_\text{e}}{M}\frac{\Omega_\text{e}^2}{\omega_{\text{p,e}}^2}\left(\frac{T_\text{i}}{T_\text{e}}\right)^{1/4}\frac{V^2}{v_{\text{th,i}}^2} = 5 \times 10^{-8}$$

This value is quite comparable to the computed value of $\mathcal{E}/nT_\text{i}$ for the measurements reported here ($\sim 7 \times 10^{-8}$). However, it should be pointed out that we might expect the electron resonance broadening mechanism to be hampered by electron collisions in MRX, so it might be surprising to find agreement with this prediction. The nonlinear Landau damping saturation mechanism predicts:

$$\frac{e\phi}{T_\text{i}} \approx 2.4\left(\frac{2m_\text{e}}{M}\right)^{1/2}\frac{V}{v_{\text{th,i}}} \approx 20\%$$

This prediction is larger than the normalized amplitude deduced from the measurements (5%), but is quite close considering the limitations of the theoretical model used in this calculation. The theory used to make this estimate ignored coupling of wave energy in unstable long parallel wavelength modes to damped shorter parallel wavelength modes [DRAKE *et al.*, 1984]. For this reason, it may overpredict the saturated amplitude in these experiments.

In a stable plasma, a certain level of electric field fluctuations is expected due to thermal effects. An estimate of the expected thermal equilibrium fluctuation level in the LHDI frequency range can now be made to compare to the measured fluctuation level. We assume that there are $N \sim k_\perp^2 k_\parallel/(2\pi)^3$ normal modes, each with energy kT. For the frequency range of interest, these modes have $k_\perp \sim 1/\rho_\text{e}$ and $k_\parallel \sim \sqrt{M/m_\text{e}}/\rho_\text{e}$. This estimate yields a normalized thermal fluctuation level of:

$$\frac{\mathcal{E}}{nT} \approx 3 \times 10^{-14}$$

This is significantly lower than the measured fluctuation level, clearly indicating that an unstable (non-thermal) feature drives these fluctuations.

4.1.5 Magnetic measurements of LHDI

A discussion of electromagnetic modifications to the LHDI was offered in Chapter 2, suggesting that magnetic fluctuations should be expected along with electrostatic LHDI fluctuations in high-beta current sheets. While the detailed study performed using electrostatic diagnostics (as presented above) has not yet been reproduced with magnetic diagnostics, evidence for electromagnetic LHDI fluctuations have been found and are presented here.

Magnetic pick-up loops were used to study magnetic fluctuations in low-collisionality current sheets (12/10 kV, 4mT, hydrogen). These studies revealed high frequency ($f \lesssim f_{\mathrm{LH}}$) magnetic fluctuations on the inner edge of the current sheet. A time trace of $\dot{B}_z$ measured at $r = 0.34$m is shown in Figure 4.15, along with a floating potential measurement at the same radial location (but separated in toroidal angle by roughly 45°). Also shown are FFT's of each signal, with the magnetic signal first integrated in time so that the FFT represents the spectrum of B rather than $\dot{B}$. The spectrum for the magnetic signal is strongest at lower frequencies when compared to the electrostatic spectrum, but does extend up to the lower hybrid frequency. The predominance of lower frequency components in the measured signal could be due to effects related to the size of the magnetic coil compared to the wavelength of the LHDI, as discussed in Chapter 3. The magnetic fluctuations are observed on the inner edge of the current sheet concomitantly with the electrostatic LHDI fluctuations measured using floating probes. The magnetic signals tend to arise later in time than the electrostatic signals, but do not, on average, persist longer. These signals are identified as magnetic LHDI fluctuations, which should be expected to appear due to electromagnetic corrections to the LHDI in high beta current sheets. The amplitude of these fluctuations is $\delta B \sim 5 - 10G$ or

$\delta B/B \sim$ a few percent, similar to the normalized amplitude in the electrostatic fluctuations. A relationship between electrostatic and magnetic fluctuation amplitude for the LHDI was presented by HUBA *et al.* [1978], although only for $T_e \ll T_i$:

$$\delta B = \frac{v_{th,i}}{c}\sqrt{\frac{M}{m_e}}\frac{\omega_{p,e}^2}{\Omega_e^2}\delta E$$

Using typical MRX parameters, and $\delta E \sim 700\text{V/m}$, this expression yields $\delta B \sim$ 1G, which is comparable to the measured fluctuation signals. However, it is likely that the magnetic probe is incapable of measuring the total fluctuation amplitude, as the wavelength of the LHDI can be comparable to the size of the coils used in these measurements. Based on Figure 3.16, this correction factor may be $\gtrsim 5$ for $\rho_e d \sim 4-5$, where d is the coil diameter (here 3 mm), but only if the magnetic LHDI spectrum is the same as the electrostatic spectrum. The fluctuations are observed to be strongest in the B_z component, which is on average an order of magnitude larger than fluctuations in the toroidal component (B_r fluctuations were not measured in these studies). This polarization is consistent with the electromagnetic LHDI, which is flute like and should not generate significant B_θ or B_r.

Additional (primarily low frequency) magnetic fluctuations are observed at large radius (outside the current sheet) and early in time ($220\mu s \lesssim t \lesssim 265\mu s$) and also near the center of the current sheet but late in time ($t \gtrsim 280\mu s$). These fluctuations are discussed in Appendix B, along with a discussion of preliminary studies of the radial profile of magnetic fluctuations in MRX.

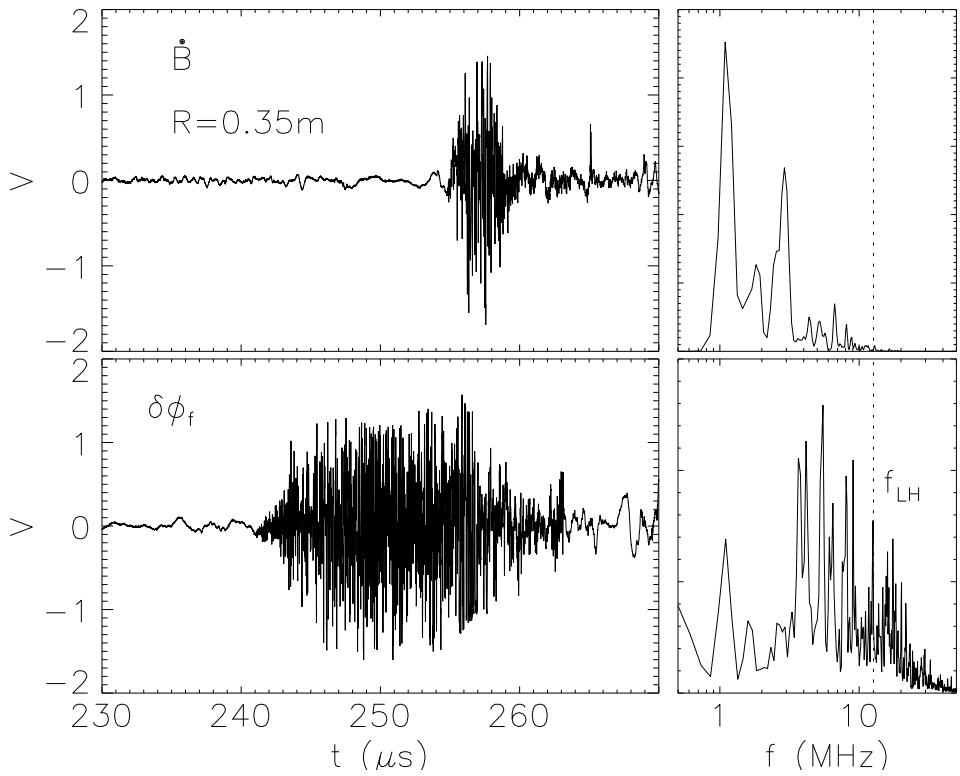

Figure 4.15: Time traces of magnetic and floating potential measurements at $r = 0.35$m, along with FFT's of the signals. The FFT of the magnetic signal is corrected to show the spectrum of B rather than $\dot{B}$.

4.2 Role of the LHDI in reconnection in MRX

One of the primary motivations for studying fluctuations in MRX is to determine the role of any observed fluctuations in the reconnection process. Of particular interest is whether or not the LHDI can generate anomalous resistivity in MRX current sheet and explain the observations listed in section 1.3.1: (1) $E_\theta/\eta_{sp} j_\theta \gg 1$, (2) $\delta \sim c/\omega_{p,i}, \rho_i$ (and $V_d/v_{th,i} \sim 3$), and (3) ion heating. Point (3) is not addressed in this work, and is left as an open question. The data and analyses presented in this section suggest that the LHDI does not produce significant anomalous resistivity and is not essential for reconnection in MRX. This conclusion stems largely

from consideration of the radial profile of the fluctuation amplitude, the time behavior of the fluctuation amplitude and the scaling of the fluctuation amplitude with collisionality.

4.2.1 Radial profiles

There are two points relevant to the question of anomalous resistivity which are raised by the measured amplitude profiles and the linear theoretical calculations presented in section 4.1.2. The first is that the measured amplitude is excluded from the high-beta magnetic null, as has been theoretically predicted by many [see, e.g. HUBA *et al.*, 1978]. The simplest mechanism of anomalous resistivity generation by turbulence is by effective scattering of the current carrying particles by the wave electric fields. The measured amplitude profile of the LHDI makes it quite difficult to apply this model to the MRX current sheet, as the turbulence is not strong at the center of the current sheet, where it is needed to provide dissipation and explain the discrepancy in the electron force balance (as shown in Figure 1.5). However, more complicated theories of anomalous resistivity generation might be constructed around this profile. For instance, these may incorporate some radial non-local effects of edge turbulence on the current sheet center. For example, one might argue that since the current density is at least partially due to diamagnetic currents, radial particle diffusion due to LHDI on the edge could lead to a relaxation of the density profile and reduce the current density, producing a seemingly resistive effect. For this reason, the radial amplitude profile alone can not rule out a critical role of the LHDI in reconnection in MRX.

The second point raised by the radial profile measurements and the accompanying theoretical calculations is that the LHDI is not marginal on the edge of MRX

current sheets. The calculated growth rates at the edge are comparable to the real frequency, a calculation which is supported experimentally by the observation of very short decorrelation length in the turbulence. This observation suggests that the scale length of the current sheet is not set by the marginal state of the LHDI, but is instead determined by some other mechanism. It is possible that the linear marginal state of the LHDI is not relevant, and that instead a nonlinear marginal condition sets the thickness of the current sheet (for example, anomalous dissipation may not set in until a finite amplitude is reached). However, the thickness of the current sheet does not change in any observable manner even though the amplitude of the fluctuations is observed to drop fairly dramatically (evident in Figure 4.7). This observation alone does not provide the evidence necessary to conclude that the LHDI is not generating significant resistivity in MRX current sheets, but is strongly suggestive that there is some other mechanism controlling the thickness of the current sheet. Other mechanisms which might provide control over the current sheet thickness, such as the Hall term in the generalized Ohm's law, will be discussed in Chapter 5.

4.2.2 Time behavior of the LHDI amplitude

An observation which provides further support for a conclusion that the LHDI is not be essential for reconnection in MRX is the measured time behavior of the fluctuation amplitude. The time behavior of the fluctuation amplitude is compared to that of the average reconnection electric field (E_θ) and the average central current density (J_θ) in Figure 4.16. The reconnection electric field is the time derivative of calculated poloidal flux value in the center of the current sheet, and represents

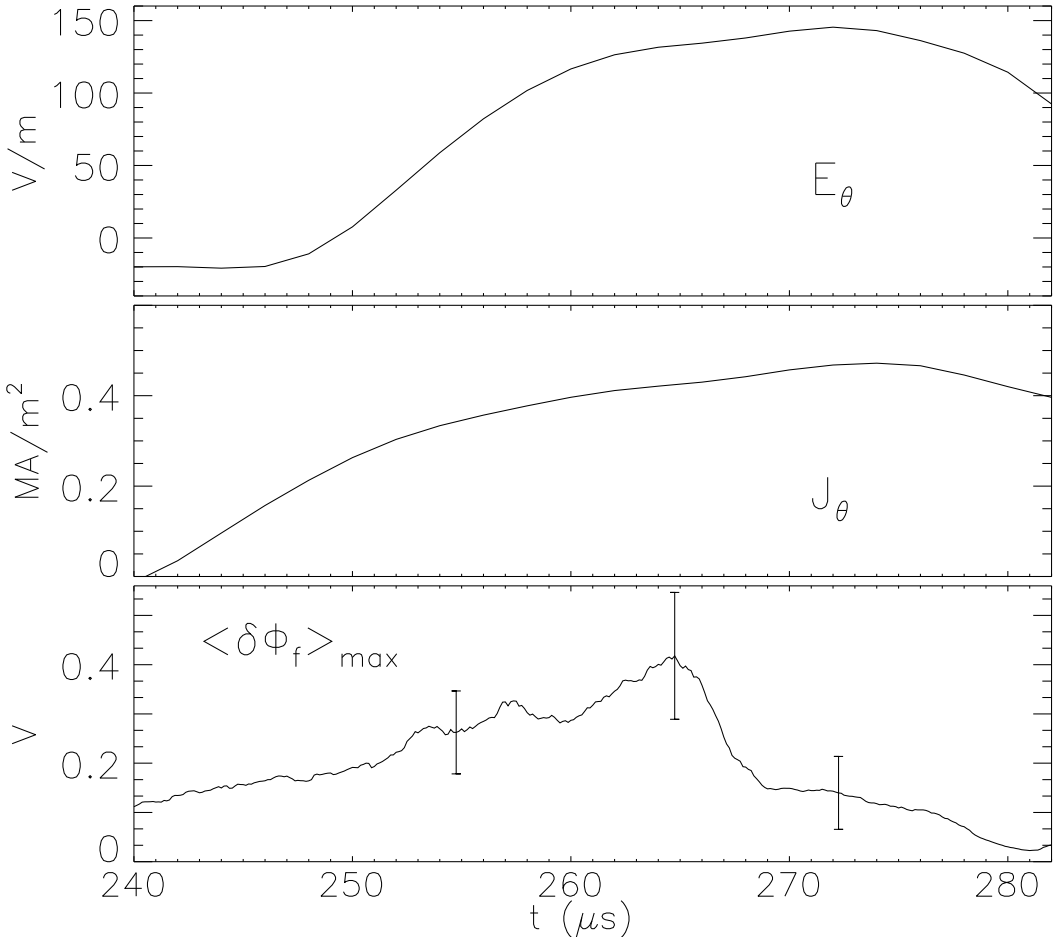

Figure 4.16: Time traces of reconnection electric field, peak current density, and peak rms fluctuation amplitude in 12/10kV 4mT hydrogen discharges.

the rate of reconnection (rate of destruction of poloidal flux interior to the current sheet in radius). From this figure, the quasi-steady reconnection phase can be identified as the time period over which the reconnection electric field is steady, roughly from $t = 260\mu s$ to $t = 280\mu s$. The fluctuation amplitude shown in this figure ($\langle \delta\phi_f \rangle_{max}$) is the peak value in space at each point in time. As was discussed in section 4.1.2, the fluctuation amplitude grows as the current sheet forms and reconnection begins, but is seen to decrease rapidly with time before the end of the quasi-steady reconnection phase. Both the reconnection electric field and the

peak current density seem rather insensitive to the fairly extreme time behavior of the peak fluctuation amplitude near $t = 265\mu s$. This observation suggests that the LHDI fluctuations are not essential for reconnection in MRX, since the reconnection rate is essentially unphased by a rapid change in the amplitude of the fluctuations. In fact, there is some evidence that the reconnection electric field and current density actually *increase* slightly following the rapid decrease in the fluctuation amplitude near $t = 275\mu s$. Although this observation is not conclusive, this might suggest that the LHDI actually impedes the reconnection process in MRX. A similar conclusion has been made with respect to recent three-dimensional Hall MHD simulations of reconnection where the LHDI is seen to arise [ROGERS *et al.*, 2000].

The measurements reported here are done only near $z = 0$, and it is possible that the fluctuations persist at high amplitude elsewhere in the current sheet even though the amplitude drops dramatically at the measurement location. However, measurements of plasma profiles downstream ($|z| > 0$) have been made, and these measurements suggest shallower density gradients and lower current densities than at $z = 0$. Therefore it is expected that the strongest drive for the LHDI should be located at $z = 0$. Even if the fluctuations did persist elsewhere, the simplest theoretical picture of anomalous resistivity generation in MRX by the LHDI, through effective scattering of the current carrying particles at the null, is unlikely to be valid in light of the observations. In the case that significant fluctuation amplitude does exist late in time at large z, one might construct a theory to explain the resistivity enhancement based on electron force balance averaged over a magnetic field line [KULSRUD, 2001]. In the case that the collisional mean-free path is long, electrons near the center of the current sheet may be effectively connected

to regions at large z where fluctuations may persist and provide anomalous dissipation. Here a point-wise electron force balance (using equation 1.3) may not be appropriate, and force balance might be maintained in an average sense along the field line. Another possibility is that, even though the amplitude of the fluctuations drops, the efficiency in resistivity generation increases accordingly. If the resistivity is provided by, for example, an average turbulent electrostatic force on the electrons ($\langle \delta n \delta E \rangle$), the phasing between the density and electric field fluctuations is crucial to determining the magnitude of the force. So in this sense, the amplitude of the fluctuations may not be the only factor determining the magnitude of the anomalous resistivity generated. These suggested alternative theories of anomalous resistivity generation are quite complicated due to the constraints put on such theories by the observations presented in this chapter. It is perhaps more likely that the offered conclusion that the LHDI is not providing significant anomalous resistivity is correct, and that some other simpler mechanism explains reconnection in MRX. Several possible mechanisms will be offered in Chapter 5.

4.2.3 Scaling of fluctuation amplitude and quasilinear resistivity with collisionality

The discussions already presented in this section provide a strong suggestion that the LHDI is not of crucial importance during reconnection in MRX. An additional data set which provides further support for this conclusion was was taken to explore the dependence of the fluctuation amplitude and computed quasilinear resistivity on the collisionality in MRX current sheets. The data shown in Figure 1.5

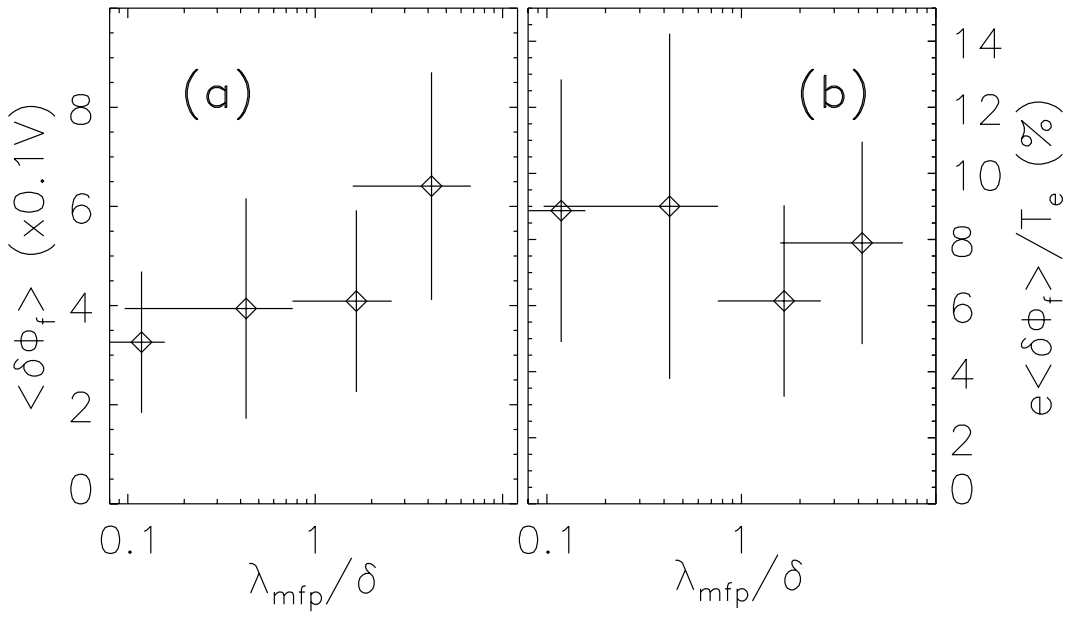

Figure 4.17: (a) Fluctuation amplitude and (b) normalized fluctuation amplitude versus collisionality from a scan in fill pressure.

demonstrate that Coulomb collisions alone are sufficient to explain the reconnection electric field (and hence the reconnection rate) in high-collisionality discharges in MRX. If the fluctuations were in some way responsible for providing anomalous resistivity or for setting the reconnection electric field in MRX current sheets, one might expect that the amplitude would be suppressed at high collisionality, where $E_\theta/\eta_{sp} j_\theta \sim 1$. Fig. 4.17(a) shows the measured peak fluctuation amplitude (peak amplitude in both space and time) versus λ_{mfp}/δ from a scan of fill pressure. The amplitude of the fluctuations does tend to increase with decreasing collisionality (increasing λ_{mfp}/δ). However, if the fluctuation amplitude is normalized to the measured electron temperature, which from Boltzmann's equation might be considered a crude estimate of $\delta n/n$ in the turbulence, we find that there is essentially no change in this quantity with collisionality, as shown in Fig. 4.17(b). Theoretical studies of the effects of collisions on the growth rate of the LHDI have been done

by HUBA and OSSAKOW [1981], resulting in an estimate for the collision frequency at which the LHDI is completely suppressed [DRAKE *et al.*, 1984]:

$$\nu_c \approx 0.814 \left(\frac{V_d}{v_{th,i}}\right)^2 \omega_{LH} \tag{4.3}$$

For the most collisional data point in Figure 4.17, the electron collision frequency is calculated to be $\nu_e \approx 375$ MHz, and the critical collision frequency calculated using Eqn. 4.3 is $\nu_c \approx 430$ MHz. The highly collisional discharges are therefore approaching the estimate for the point at which the LHDI might be collisionally suppressed, but are sufficiently below this point so that it is not surprising to observe high amplitude fluctuations.

Theoretical estimates of effective collision rates produced by LHDI fluctuations depend on the normalized amplitude of the fluctuations, $\mathcal{E}_k/nT \sim (\delta n/n)^2$ (see Eqn. 2.8). Figure 4.17(b) then suggests that the effective collision rate provided by the LHDI fluctuations in MRX should be fairly constant as the collisionality is drastically changed in the current sheet. However, as the collisionality is raised in MRX $\nu_{e,i}$ increases dramatically, and therefore the normalized LHDI resistivity, $\nu_{LHDI}/\nu_{e,i}$ might behave in a manner consistent with Figure 1.5. We can now compute the normalized effective LHDI collision rate for this set of data, using Eqn. 2.8 along with the measured amplitude, plasma parameters and the linear theoretical estimates for the LHDI shown in Figure 4.8. For example, for the lowest collisionality data point in Figure 4.17,

$$\begin{aligned}
\nu_{LHDI} &= \mathrm{Im}\left(k_\perp \frac{4\omega_{p,i}^2}{k_\perp^2 v_{th,i}^2}\zeta_i Z(\zeta_i)\right)_{k_{\perp,max}} \frac{T_i}{m_e V}\frac{\mathcal{E}}{nT_i} \\
&= \frac{\omega_{p,i}^2}{\Omega_i^2}\frac{v_{th,i}}{V}\frac{\mathcal{E}}{nT_i}\mathrm{Im}\left(\frac{4}{k_\perp \rho_e}\zeta_i Z(\zeta_i)\right)_{k_{\perp,max}} \omega_{LH} \\
&\approx 0.6\omega_{LH} = 26\mathrm{MHz}
\end{aligned}$$

This estimate is actually lower than the Coulomb collision rate for that data point, $\nu_{e,i} \approx 35$MHz, suggesting a resistivity enhancement of less than a factor of two. Figure 4.18 shows the computed LHDI resistivity enhancement along with the measured resistivity enhancement ($E/\eta_{sp}j$) as a function of collisionality for all the data points in the pressure scan. While the LHDI resistivity enhancement does increase with decreasing collisionality, it is clearly insufficient to explain the observed value of $E/\eta_{sp}j$. It should be noted that the effective collision rate is computed using the maximum fluctuation amplitude (maximum in both time and space), and therefore provides a very generous estimate of the LHDI resistivity. The amplitude at the center of the current sheet, where $E/\eta_{sp}j$ is measured, is significantly lower than this peak amplitude, and an estimate of the effective collisionality there should be more than an order of magnitude lower.

4.3 Summary

In this Chapter, detailed measurements of fluctuations in the MRX current sheet were presented. These measurements have led to the first experimental identification of the lower-hybrid drift instability in a laboratory current sheet, and to the first opportunity for a detailed study of the role of this instability in magnetic reconnection. Support for identifying the measured fluctuations as being due to the LHDI was provided by detailed measurements of the frequency spectrum, radial amplitude profiles and spatial correlations. A local linear theory of the LHDI was used to successfully explain asymmetries observed in the measured radial fluctuation amplitude profile. Correlation measurements indicated a decorrelation length in the turbulence which was comparable to the theoretically predicted

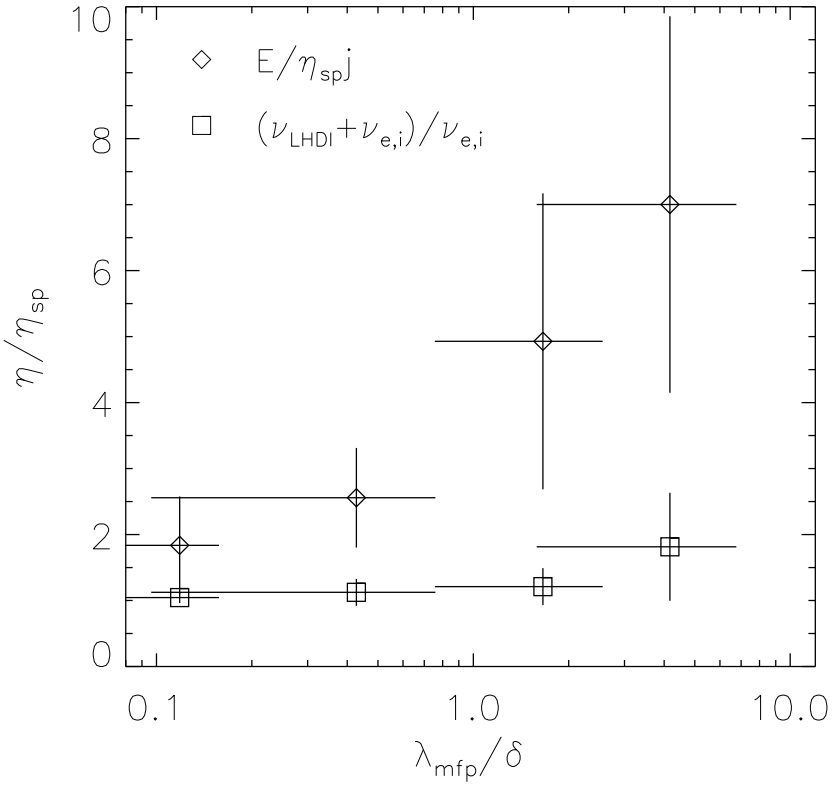

Figure 4.18: Measured resistivity enhancement and computed LHDI resistivity enhancement as a function of collisionality

wavelength of the LHDI, an observation which is consistent with a theoretically predicted strong linear growth rate. Measurements of phase velocity in the fluctuations suggested a preference for propagation in the electron diamagnetic direction, but a statistically significant value for the phase velocity was not found due to a large variations in the measured phase at each frequency in the turbulence. Estimates of the expected saturation amplitude by electron resonance broadening and nonlinear mode coupling were made based on measured plasma parameters. The estimate for the measured potential fluctuation amplitude was found to be comparable to the electron resonance broadening estimate, but roughly a factor of

4 lower than the nonlinear Landau damping estimate.

The observations presented suggest that the LHDI does not play an essential role in reconnection in MRX. The role of the LHDI in the reconnection process in MRX was explored through studying the spatial and temporal behavior of the fluctuation amplitude and through studying the dependence of the fluctuation amplitude on the current sheet collisionality. The observed radial profile of the fluctuations is consistent with several theoretical predictions that the LHDI should not penetrate to the high-beta null point. In addition, it was noted that the current sheet profile in MRX is not the marginal state of the LHDI, and that it is therefore possible that the spatial scale of the current sheet is not controlled by the turbulence alone. The temporal behavior of the fluctuation amplitude provided further support for the conclusion that the LHDI is not essential to reconnection in MRX. The amplitude was observed to drop dramatically during reconnection, while the reconnection rate (electric field) was steady. The mechanism for the drop in amplitude is still not fully understood, but this observation makes it difficult to claim that the LHDI is providing anomalous dissipation during reconnection in MRX. Finally, a study of the effect of collisionality in the current sheet on the fluctuation amplitude and computed effective collisionality was performed. The normalized fluctuation amplitude was found to be fairly insensitive to the collisionality in MRX current sheets. The quasilinear estimate of the LHDI collisionality was found to fall short of the Coulomb collision rate in low collisionality discharges, even when the peak fluctuation amplitude is used in the computation, further suggesting that the LHDI is not responsible for enhancing the resistivity in MRX current sheets.

Chapter 5

Summary and Discussion

THE ROLE OF TURBULENCE in the process of magnetic reconnection has been debated for decades. In this dissertation, the first experimental study of fluctuations in a neutral current sheet formed in an MHD plasma is presented. The primary result of this dissertation is the experimental observation of the lower-hybrid drift instability operating in the current sheet of MRX. This represents the first observation and detailed characterization of this instability in a current sheet in the laboratory. The detection of the LHDI in MRX provided the unique opportunity to study the role of the instability in magnetic reconnection, in an experiment where the reconnection rate can not be explained by classical collisional dissipation. The data and analysis presented in this dissertation suggest that the LHDI is not essential to the reconnection process in MRX. Both the observation of the LHDI and the analysis of its role in reconnection in MRX could have a wide-ranging impact. Specifically the observation that turbulence does not seem to be crucial for reconnection to occur in collisionless MRX plasmas could be applicable to reconnection in the solar corona, the magnetosphere, and in

other laboratory devices such as magnetically confined fusion experiments.

5.1 Dissertation summary

High-frequency fluctuations were detected in the MRX neutral sheet using a novel diagnostic technique in which wideband amplifiers were embedded near the tips of floating Langmuir and magnetic pick-up probes. The identification of the observed high-frequency fluctuations as lower-hybrid drift waves was made following detailed studies of the spectrum, radial amplitude profile and spatial correlations of the fluctuations. A scan of the lower hybrid frequency in the MRX current sheet was made through varying the field strength and mass of the working gas. This scan demonstrated consistency between the measured frequency spectra and the theoretical expectation for the LHDI. The radial amplitude profile of the fluctuations was found to be asymmetric with respect to the current sheet location, with the amplitude strongly peaked on the inner edge of current sheets formed in MRX. The observed asymmetry was successfully explained using a local, electrostatic, linear theory of the LHDI along with measured profiles of density, temperature, and magnetic field. Asymmetries in the driving forces behind the LHDI, the density gradient and cross-field drift, coupled with an asymmetric profile of stabilizing plasma beta provide an explanation for the measured radial profile. The amplitude of the fluctuations was observed to peak early in the reconnection process and then drop fairly dramatically before the end of the quasi-steady reconnection phase in MRX. The details of this time behavior are still not fully understood, but a potential explanation was offered based on ion heating during reconnection. Studies of

spatial correlations in the observed fluctuations yielded an estimate for the decorrelation length which was comparable to the theoretically predicted wavelength of the LHDI. This observation is consistent with the linear theoretical prediction of a very strong growth rate for the LHDI in MRX current sheets, $\gamma \sim \omega_r \sim \omega_{LH}$. The propagation characteristics of the fluctuations were investigated through construction of statistical dispersion relations using the phase in the cross-spectrum of spatially separated probes. These investigations revealed a preference for propagation in the electron diamagnetic direction, but a statistically significant value for the phase velocity of the waves was not determined. The inability to accurately determine the phase velocity was likely contributed to linear effects, such as the three-dimensional nature of the wave vector, as well as turbulent nonlinear broadening of the wave dispersion.

The primary motivation for studying fluctuations in the MRX current sheet was to ascertain the role of turbulence in the process of magnetic reconnection. The observations reported in this dissertation indicate that the LHDI is not essential in determining the reconnection rate in MRX current sheets. This conclusion is supported by the radial profile and time behavior of the fluctuation amplitude as well as the scaling of the fluctuation amplitude with current sheet collisionality. The radial profiles, as discussed above, were seen to be consistent with the linear theory of LHDI, as the instability is observed to be suppressed at the high-beta magnetic null in the center of the current sheet. This observation suggests that no local anomalous resistivity can be produced by the LHDI at the null in MRX. In addition, it seems unlikely that the LHDI is the dominant physical mechanism controlling the width of the current sheet in MRX, as the instability is not marginal and is in fact very strongly growing. Perhaps the strongest evidence suggesting

that the LHDI is not essential in determining the reconnection rate in MRX comes from the observed time behavior of the instability amplitude. The fluctuation amplitude is measured to grow during formation of the current sheet and early in the reconnection process. However, the amplitude peaks early during reconnection and drops significantly while the reconnection rate (the reconnection electric field) remains fairly steady. Again, the exact mechanism behind this time behavior is not clearly understood; however, this observation casts doubt on the role of the LHDI in producing sufficient anomalous resistivity in MRX. An additional study of the behavior of the LHDI amplitude with collisionality was performed, motivated by the observation of classical reconnection (described by collisional resistivity) at high current sheet collisionality. Very little change in the peak normalized amplitude of the LHDI was observed as the collisionality was increased over an order of magnitude. An estimate of the quasilinear collision rate due to the LHDI was made, finding that the collision rate at the peak of the amplitude in space and time is no larger than the Coulomb collision rate in MRX plasmas, even in low-collisionality current sheets. While these observations are not necessarily conclusive in ruling out any important role of the LHDI in MRX current sheets, they place significant constraints on any theory which would invoke this instability in producing anomalous resistivity during reconnection.

5.2 Future directions

While LHDI turbulence is observed during reconnection in MRX, it is very unlikely to be the explanation for fast reconnection in collisionless plasmas in MRX.

In addition, the diagnostics used for this study are capable of detecting fluctuations up to roughly ten times the lower hybrid frequency, and currently there are no other fluctuations observed which are likely candidates to provide anomalous resistivity[1]. For this reason, it is currently difficult to construct a theory of fast reconnection based on anomalous resistivity in MRX. Therefore in order to gain understanding of the physical mechanism behind reconnection in MRX, the experimental focus should likely be shifted away from turbulence and fluctuations and to other possibilities. One prominent alternative possibility is that the recent Hall dominated reconnection theories are applicable to MRX. In addition, resistivity generation by collisions with neutrals and by particle orbit effects is possible. Following a description of these alternative possibilities, a discussion of further fluctuation studies will be offered.

5.2.1 Hall dominated reconnection in MRX

The theory of collisionless reconnection based on the Hall term in the generalized Ohm's law was briefly presented in Chapter 1. This theory might offer an explanation for observations in MRX, and experiments designed to look for the signatures of this type of reconnection should be undertaken. Simulations of Hall dominated reconnection predict the possibility of a two-scale current sheet – with an ion current sheet on the $c/\omega_{p,i}$ scale and a much sharper electron current sheet on the scale at which collisionless dissipation is available ($c/\omega_{p,e}$ for inertial dissipation, for example) [SHAY *et al.*, 1998]. First of all, it is interesting to note that MRX current sheets are observed to have $c/\omega_{p,i}$ thickness. The data in this dissertation have

[1] Appendix B discusses other magnetic fluctuations which have been observed. These seem unlikely to provide anomalous resistivity based on early observations.

cast doubt on the role of turbulence in controlling this thickness, and it is quite possible that instead the Hall term plays this role. The two-scale current sheet could provide an explanation for the observed discrepancy in the electron force balance in MRX current sheets (see Figure 1.5). From the perspective of the Hall dominated simulations, the discrepancy is not caused by an enhanced resistivity, but instead by a small scale (currently unobserved) structure in the current density. These current structures are expected on quite small scales, perhaps as small as $c/\omega_{p,e}$, and it is quite likely that current diagnostics are incapable of detecting it. The electron skin depth, $c/\omega_{p,e} \approx 0.5mm$ in MRX, is actually 6 times smaller than the diameter of the pick-up coils used to make measurements in MRX (thus the primary issue is not the separation between coils, but the size of the coils themselves). In addition to structures in current density, in these simulations the generation of a quadrupole structure in out-of-plane magnetic field near the null point (out-of-plane refers to toroidal field in MRX) is observed. The structure in the out-of-plane field is also at small scales (again, $c/\omega_{p,e}$ in some simulations), and it is unlikely that the current set of diagnostics is capable of detecting these structures. New diagnostics need to be developed in order to study structures at small scales in the current sheet, and test the viability of the Hall dominated theories in MRX current sheets. Very few three-dimensional simulations of collisionless reconnection including Hall effects have been done, but the initial simulations have suggested that turbulence might be driven by the electron scale current sheet, and might result in a break-up of that current sheet structure [ROGERS *et al.*, 2000; DRAKE, 1997]. The turbulence observed in these simulations is very high frequency ($\omega \gtrsim \Omega_e$, due to a Kelvin-Helmholtz type instability) and does not contribute an anomalous resistivity, but may provide a viscous or hyperresistive effect at small scales. Even in the case

where the electron current sheet breaks-up, it is found that the rate of reconnection is still controlled by the physics of the standing whistler wave (in these models the reconnection rate is insensitive to the dissipation mechanism, whether it be a laminar mechanism such as electron inertia, or a viscous or hyperresistive dissipation due to electron timescale turbulence). In this case, the electron scale current structure may not be observable in MRX, yet the signature of the standing whistler wave (the out-of-plane magnetic field) should persist. Future experiments might therefore focus on detection of this feature, through the development of high resolution magnetic diagnostics.

5.2.2 Neutral resistivity

Another possible explanation for the discrepancy in the electron force balance in the current sheet of MRX is the effects of neutral collisions on the resistivity. The ionization fraction in MRX, based on the assumption that the neutral density is uniform in space and is determined by the fill pressure prior to ionization is roughly 10-30% (for 2-8 mT fill pressure, peak density is roughly 1-10$\times 10^{13}$cm^{-3}). Therefore a large fraction of the gas inside the vacuum chamber during the plasma discharge is possibly not ionized. The ratio between the Coulomb collision frequency and the neutral collision frequency is (where σ_o is the electron-neutral collision cross-section):

$$\frac{\nu_o}{\nu_e} = \frac{n_o}{n_e}\frac{\sigma_o}{2.9\times 10^{-6}\sqrt{m_e}}T_e^2$$

The ratio scales as T_e^2/f_{ion} (assuming σ_o is largely independent of the electron temperature), where $f_{ion} = n_e/n_o$. The electron temperature in MRX is seen to rise from roughly 5 eV to 10 eV as the collisionality is lowered, while the ionization fraction is roughly constant, suggesting that this ratio should increase in a fashion

qualitatively consistent with the discrepancy in the electron force balance shown in Figure 1.5. However, even though the collision rate scales consistently with the resistivity enhancement, the cross section for electron-neutral collisions is quite low and the absolute value of the collision rate might be far too small to explain the observed enhancement. For example, the cross section for elastic collisions with neutrals is roughly $\sigma_o \approx 1 \times 10^{-16}\text{cm}^2$, yielding a neutral collision rate of around 1 MHz in low Coulomb collisionality MRX plasmas. This rate is an order of magnitude less than the Coulomb collision rate in these plasmas, which is around 35 MHz. In order for neutrals to explain the reconnection rate in MRX, the cross section must be significantly enhanced by inelastic processes. Numerical studies are currently under way to determine the neutral density profile in MRX. These studies will be complimented by spectroscopic experiments of neutral emission profiles in MRX.

5.2.3 Inertial resistivity

SPEISER [1970] first introduced the concept that the finite lifetime of particles in a current sheet can produce a resistive effect due to particle inertia. Speiser assumed that the current-carrying particles experience the reconnection electric field for a finite time τ_c before being lost from the current sheet. During this time, inertia limits the speed, and hence current, which these particles can obtain in the accelerating electric field. Speiser's single-particle orbit model predicts the lifetime of the particles in the current sheet is approximately the cyclotron orbit timescale in the reconnected field present in the outflow region (B_r in MRX). Orbits about this field carry the particles in the outflow direction, allowing them to escape. In MRX, Speiser's simple effective inertial collision rate is far too small to explain the rate

of reconnection ($\tau_c \gtrsim 10\mu s$). However, recent detailed theoretical work on orbits in current sheets [EGEDAL and FASOLI, 2001b] and in field-reversed configuration (FRC) plasmas [GLASSER and COHEN, 2001] have shown that effective scattering due to orbit effects may provide significant resistivity and particle heating. Recent experiments studying the formation of current sheets in a magnetic cusp geometry have suggested that, at certain values of the applied drive electric field, current sheet formation is suppressed entirely by single-particle orbit effects, resulting in an effective infinite inertial resistivity [EGEDAL and FASOLI, 2001a]. These results are consistent with previous theoretical studies of current sheet equilibria which suggest that below a critical electric field orbit effects prevent current sheet formation [BURKHART *et al.*, 1992]. MRX is clearly in the regime where current sheet formation is allowed, and therefore the applicability of these orbit effects to resistivity enhancement in MRX is unclear. Experimental investigation of these effects in MRX would be quite difficult, most likely requiring detailed knowledge of the particle distribution functions in the current sheet. However, theoretical studies of single-particle orbits in MRX geometry could be carried out to ascertain their importance.

5.2.4 Further fluctuation studies

The study of the LHDI presented in this dissertation is by no means an exhaustive study of the properties of this instability in MRX current sheets. Measurements of the fluctuation characteristics should be performed in other locations in the $r-z$ plane in MRX, in order to fully understand the spatial and time behavior of the instability amplitude. This type of study is motivated by the possibility that a non-local resistivity generated by the LHDI may be present in MRX. It is possible that if

fluctuations are present downstream, the friction produced by these waves at $z > 0$ could somehow be transferred to the center of the current sheet by collisionless effects along a magnetic field line [KULSRUD, 2001]. In addition, studies of the full two-dimensional amplitude profile are motivated by predictions from Hall dominated three-dimensional simulations of reconnection where the LHDI is driven by electron-scale structures associated with standing whistler waves downstream from the center of the current sheet [ROGERS *et al.*, 2000]. The time behavior of the fluctuation amplitude is not fully understood, and an understanding of the behavior of the fluctuations at large z could help resolve this issue. Another topic which should be investigated is the role of the observed LHDI fluctuations in ion heating in MRX. Ion heating has been studied in detail in reconnection current sheets in MRX [HSU *et al.*, 2000], and it is possible that the LHDI contributes to the observed heating. In addition, much work remains to be done in characterizing the magnetic fluctuations whose preliminary observations are outlined in Appendix B. Studies of these fluctuations similar to those performed on electrostatic fluctuations in this dissertation should be undertaken in order to identify their source.

Additional fluctuation measurements could be performed at higher frequency ranges than studied in this dissertation. The role of higher frequency fluctuations ($\omega \gtrsim \Omega_e$) in resistivity generation is questionable due to the likely inability of waves in this frequency range to effectively interact with the ions and exchange momentum between electrons and ions. However, higher frequency fluctuations might be important in generating viscous and hyperresistive dissipation [ROGERS *et al.*, 2000]. Instabilities in this frequency range might also lead to a break up of small scale features expected to form as a result of the Hall term in MRX current sheets [DRAKE, 1997]. Capacitive probes constructed using impedance matching

probe tip buffer amplifiers should be capable of detecting fluctuations in the GHz frequency range [BENJAMIN, 1982].

Appendix A

Analysis of field perturbations due to a ferrous transformer core

HIGH-BANDWIDTH PULSE TRANSFORMERS are employed in the amplifier circuits used in the electrostatic (Langmuir probe) fluctuation diagnostics described in Chapter 3. These transformers are wound on toroids of high-μ ferrous material, which could potentially perturb the local field when inserted into a plasma. This perturbation might alter the field near the tip of the probe and hence disturb the floating potential measurement being performed. The extent of the field perturbation can be calculated straightforwardly by assuming the transformer core to be spherical with a radius of 1.5 mm (the actual cores are toroidal with major radius plus minor radius equal to 1.5 mm, making this assumption conservative). Consider the case where a uniform background field, B_0, exists and the spherical core is inserted into the field[1]. The problem can be solved

[1]This problem can be found in electricity and magnetism textbooks [GRIFFITHS, 1989; JACKSON, 1998]

by assuming the core is a linearly permeable material and through taking a perturbative approach. First assume the zero-order field is the field inside the core and calculate the magnetization of the sphere:

$$\mathbf{M}_0 = \chi_\mathrm{m}\mathbf{H}_0 = \frac{\chi_\mathrm{m}}{\mu_\mathrm{o}(1+\chi_\mathrm{m})}\mathbf{B}_0$$

Where χ_m is the magnetic susceptibility of the core. The field within a sphere of material with magnetization $\mathbf{M}$ is $\mathbf{B} = (2/3)\mu_\mathrm{o}\mathbf{M}$. The first order magnetic field inside the core due to the zeroth order magnetization is then:

$$\mathbf{B}_1 = \frac{2}{3}\frac{\chi_\mathrm{m}}{1+\chi_\mathrm{m}}\mathbf{B}_0 = \frac{2}{3}K\mathbf{B}_0$$

where $K = \chi_\mathrm{m}/(1+\chi_\mathrm{m})$. It can easily be shown that higher order corrections to the field inside the sphere are:

$$\mathbf{B}_\mathrm{n} = \left(\frac{2}{3}K\right)^n \mathbf{B}_0$$

This results in a geometric series solution for the magnetic field inside the sphere:

$$\mathbf{B} = \sum_{n=0}^{\infty}\left(\frac{2}{3}K\right)^n \mathbf{B}_0 = \frac{1}{1-2K/3}\mathbf{B}_0$$

So that the exact solution to the magnetic field inside the sphere is:

$$\mathbf{B} = \frac{1+\chi_\mathrm{m}}{1+\chi_\mathrm{m}/3}\mathbf{B}_0 \tag{A.1}$$

The field outside of the core is dipolar, with dipole moment $\mathbf{m} = (4\pi/3)R^3\mathbf{M}$, where R is the radius of the sphere. The assumption that the core is linear is strictly incorrect, however, the relation:

$$\mathbf{B} + 2\mu_\mathrm{o}\mathbf{H} = 3\mathbf{B}_0$$

is valid in the nonlinear core [JACKSON, 1998]. Here the upper limit for the field internal to the core ($\mathbf{B}$) is still $3\mathbf{B}_0$, which is the $\chi_m \to \infty$ limit of equation A.1. Figure A.1 shows contours in the $r-z$ plane of magnetic field strength in the presence

of the ferrous core, normalized to the initial field strength, B_0, for the $\chi_m \rightarrow \infty$ limit of equation A.1. The position of the probe shaft (for both $1/4''$ and $3/8''$ cases) as well as the placement of the probe tips is shown in this figure. The field due to the core falls off rapidly toward the probe tips, and should be a negligible perturbation to the background field near the tips. A stronger perturbation is found along the z axis of the core (along the unperturbed field direction), with a 20% perturbation at the edge of the $1/4''$ shaft and a 6% perturbation near the edge of the $3/8''$ shaft. These perturbations fall off sharply, and any perturbation to the plasma should be dominated by the presence of the probe shaft itself. The use of a very small ferrous core in the buffer amplifier circuit should therefore not result in a significant perturbation of the local field and should not adversely effect fluctuation measurements. Magnetic field measurements near the fluctuation probe shaft (using the 29-channel 1D probe array within 1-2 cm of the probe shaft in the z direction) support this conclusion, showing no evidence of a perturbation due to the transformer core (within $\sim 5\%$ error bars).

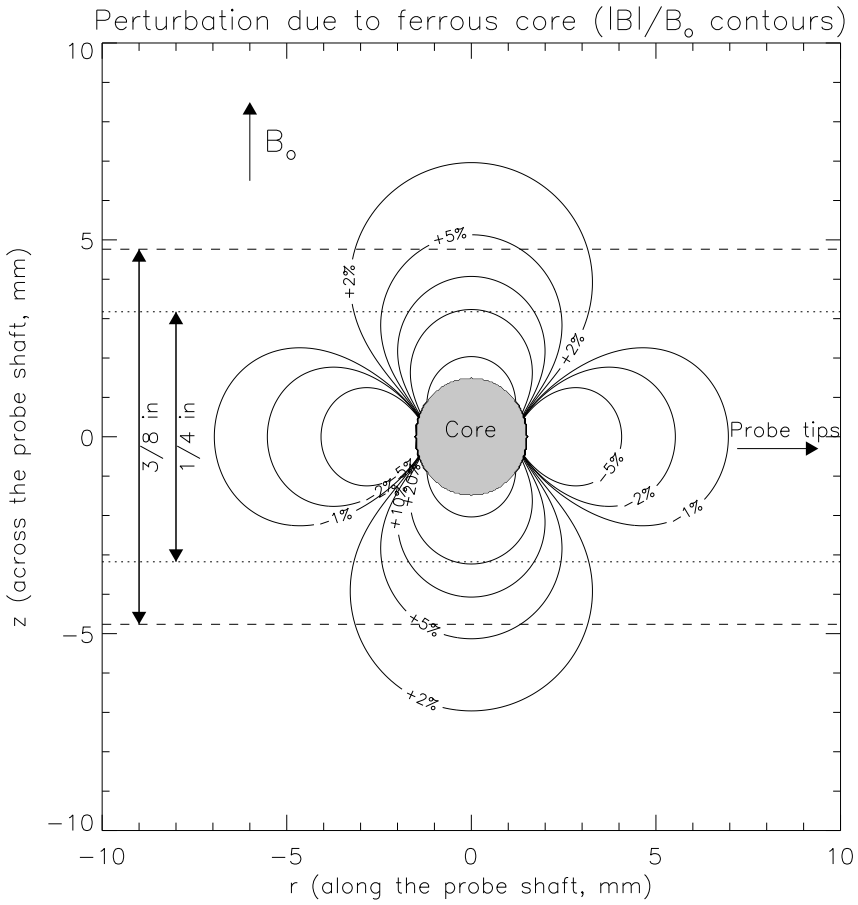

Figure A.1: Magnetic perturbation due to ferrous transformer core used in buffer amplifiers in fluctuation probes. The size of 1/4″ and 3/8″ shafts are shown. The probe tips are approximately 10 mm away along *r* from the core.

Appendix B

Survey of magnetic fluctuations in MRX

ADDITIONAL magnetic signals were observed during studies of the lower-hybrid drift instability in MRX current sheets. The instabilities or other plasma phenomena associated with these signals have not yet been positively identified, but in this appendix we will comment on the characteristics of the fluctuations and possible roles they may have during reconnection in MRX.

Magnetic fluctuations were measured in low-collisionality null-helicity current sheets in MRX using the magnetic fluctuation diagnostic described in Chapter 3. Three classes of fluctuations are observed in the measurements: (1) Lower hybrid frequency range signals which are observed at the inner edge of the current sheet; (2) Broadband, intermediate frequency (0.1MHZ $\lesssim f \lesssim$ 10MHz) signals observed at larger radii (39cm $\lesssim r \lesssim$ 45cm); and (3) Low frequency ($f \sim$ 500kHz), short-lived signals observed near the center of the current sheet and late in time

($t \gtrsim 280\mu s$). The first class of fluctuations, an example of which was shown in Figure 4.15, are attributed to the LHDI and were discussed briefly in Chapter 4.

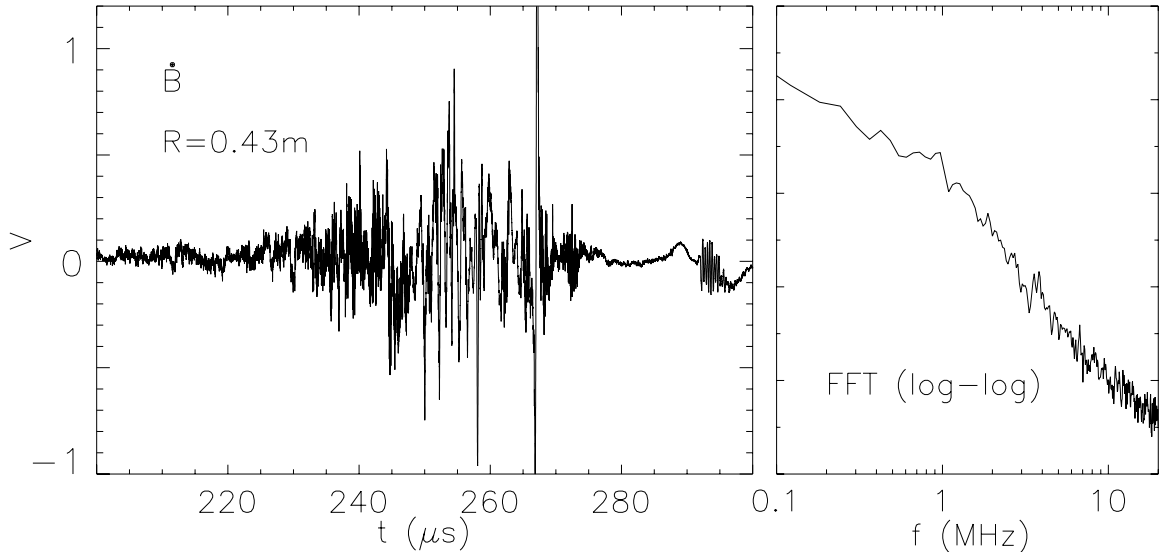

Figure B.1: Magnetic measurement at $r = 0.43$m, along with an FFT of the signal, corrected to show the spectrum of B rather than $\dot{B}$.

Figure B.1 shows an example of the second class of magnetic signals, which are observed at radii larger than the current sheet center, starting at the outer edge and persisting as far as 10 cm away (this measurement is taken at $r = 0.43cm$, measuring fluctuations in B_z). An FFT of the example signal (corrected to show the spectrum of B rather than $\dot{B}$) shows the spectrum is broadband and fairly featureless, extending up to several MHz (relevant frequencies at this spatial location: $f_{\mathrm{LH}} \sim 4$MHz, $f_{\mathrm{c,i}} \sim 100$kHz). The peak value of δB derived from this measurement is roughly 10G, making $\delta B/B \sim 10\%$. Nearly equal amplitude fluctuations are observed in B_z and B_θ for this class of signals. Figure B.2 shows contour plots of electrostatic and magnetic fluctuation rms amplitude (both high-pass filtered at 500 kHz, B_z measured with magnetic diagnostics) for a radial scan performed in low-pressure hydrogen discharges (12/10 kV, 3.5 mT). The trajectory of both the

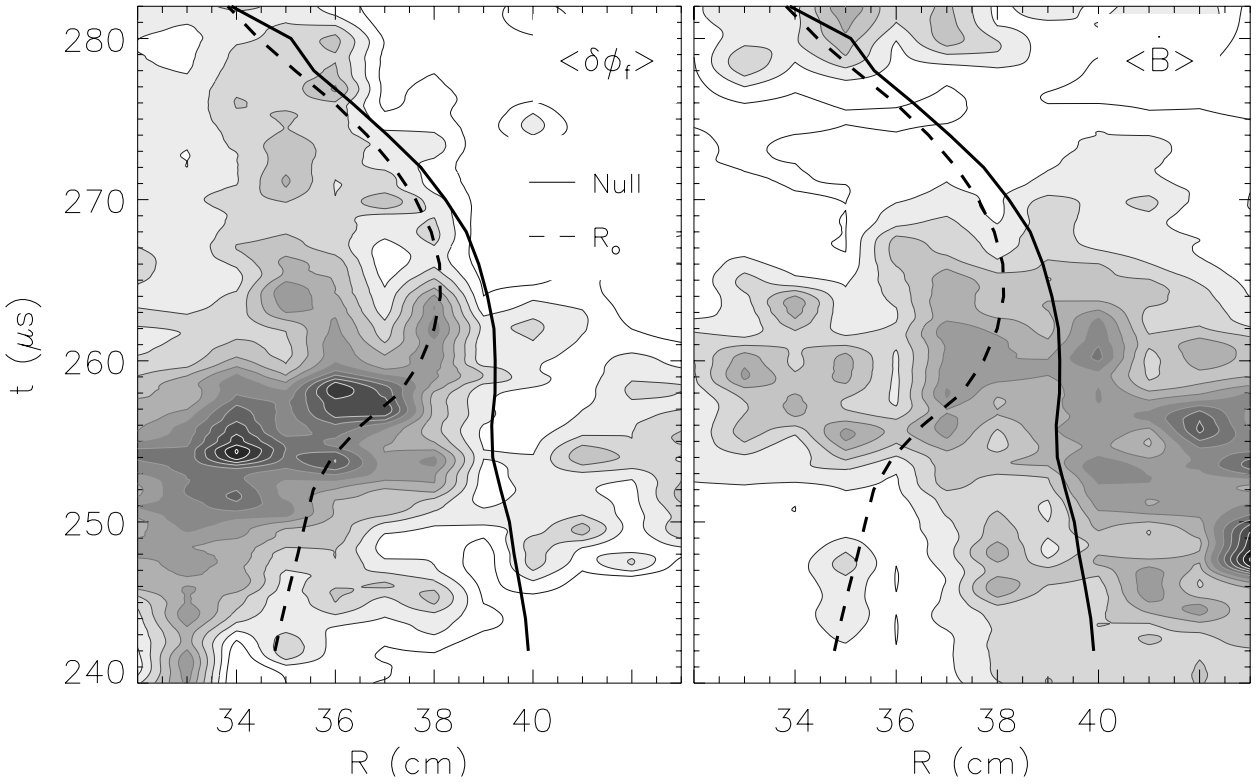

Figure B.2: Contours of rms amplitude of $\delta\phi_f$ and $\dot{B}$ during 12/10 kV, 3.5 mT discharges in MRX. Superimposed are the trajectory of the location of peak current density (dotted line) and of the magnetic null (solid line).

peak of the current density (derived from fitting the magnetic measurements to a Harris profile) as well as the trajectory of the magnetic null are shown. The electrostatic signals are observed to stay primary to the inside of the magnetic null, peaked on the inner edge of the current sheet, as discussed in Chapter 4. The magnetic amplitude profile is less clear-cut, but a transition from signals in class (1) (identified as magnetic LHDI, and shown in Figure 4.15) to those in class (2) (as shown in Figure B.1) is observed when going from inside to outside the null location in radius. The current density is small at $r = 0.43$cm where strong fluctuations (class (2)) are observed, and it is therefore unlikely that these signals are due to a current driven instability. A likely candidate for the energy source of these

fluctuations is flow and flow shear which has been observed spectroscopically at large radius in null-helicity helium discharges. Figure B.3 shows a spectroscopic measurement of the radial profile of toroidal ion flow in MRX [HSU *et al.*, 2001]. The source of these toroidal flows is not clear, although there is some evidence from radial floating potential measurements that they may be due to radial electric fields at on the outer edge of MRX plasmas [HSU *et al.*, 2001].

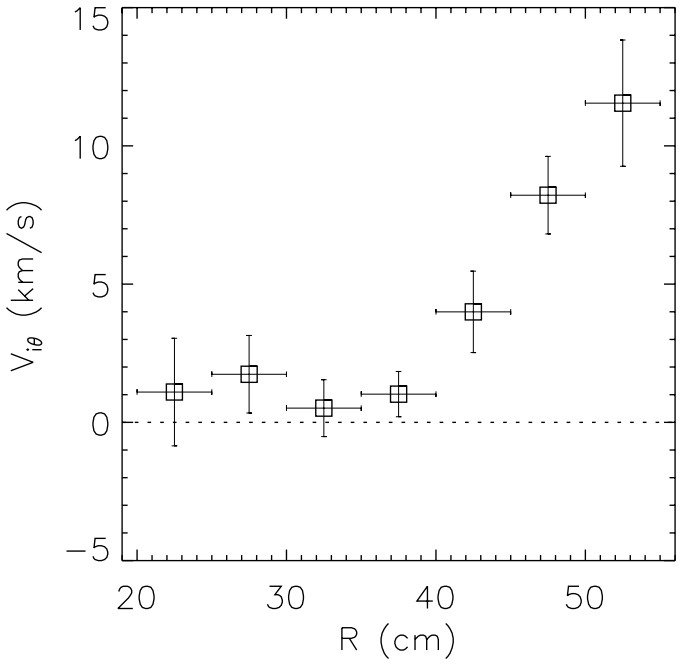

Figure B.3: Spectroscopic measurement of the radial profile of toroidal ion flow in helium discharges in MRX. [HSU, 2000]

The third class of magnetic signals are observed near the center of the current sheet, but very late in time. Figure B.4 shows an example of this type of signal, which is typically low frequency, short lived, and large amplitude (here $\delta B/B \sim 1$). This signal is measured on the inner edge of the current sheet $r = 0.35$m, and includes an observation of magnetic LHDI fluctuations. A wavelet transform was employed to estimate the frequency content of the time integral of this signal, and

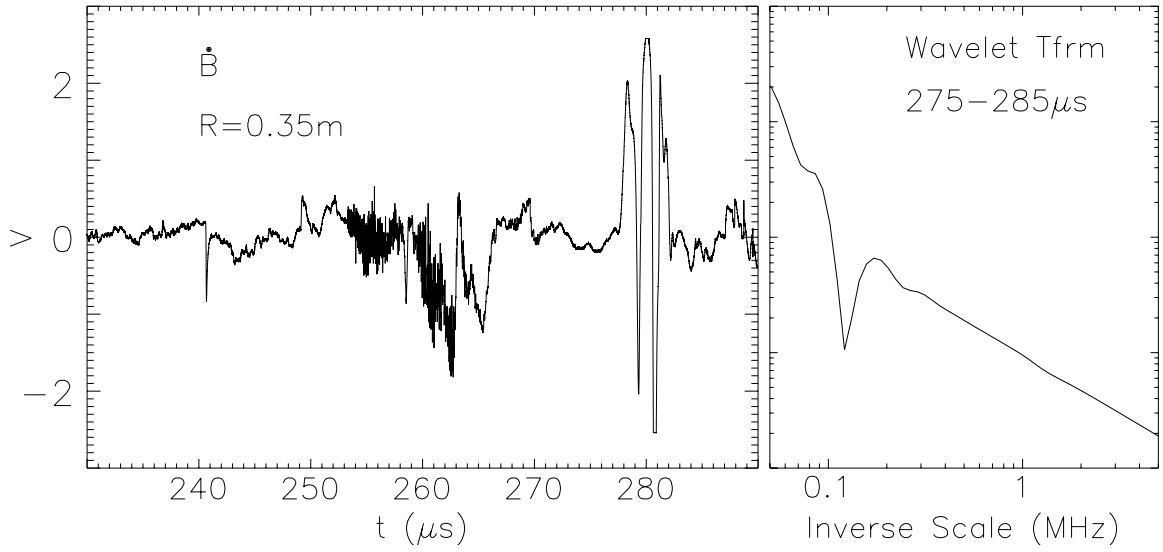

Figure B.4: Magnetic signal showing magnetic LHDI fluctuations and a large amplitude low frequency signal later in time. Also plotted is the wavelet transform of the time integrated low frequency signal.

is also shown in Figure B.4. The signal sits in the 0.1-1 MHz range, which is near the local value of the ion cyclotron frequency ($\Omega_i \sim 300$kHz). This third class of magnetic signals are typically observed near the center of the current sheet, but at or after the end of the quasi-steady reconnection phase ($t \gtrsim 280\mu s$). Figure B.5 shows contours of rms magnetic fluctuation amplitude for frequencies above 100 kHz, from the same radial fluctuation scan as presented in Figure B.2. The third class of signals are localized near (just above) the trajectory of the null, and late in time ($t \gtrsim 280\mu s$). The time behavior of the amplitude of the these late-time signals is compared to the behavior of the electric field and plasma current at late times in Figure B.6. In this figure, the maximum (in space) fluctuation amplitude for signals above and below 800 kHz is compared to the reconnection electric field and the total plasma current. The third class of signals are observed to arise near $t = 275\mu s$ and peak near $t = 282\mu s$. Soon after the peaking of these low-frequency signals,

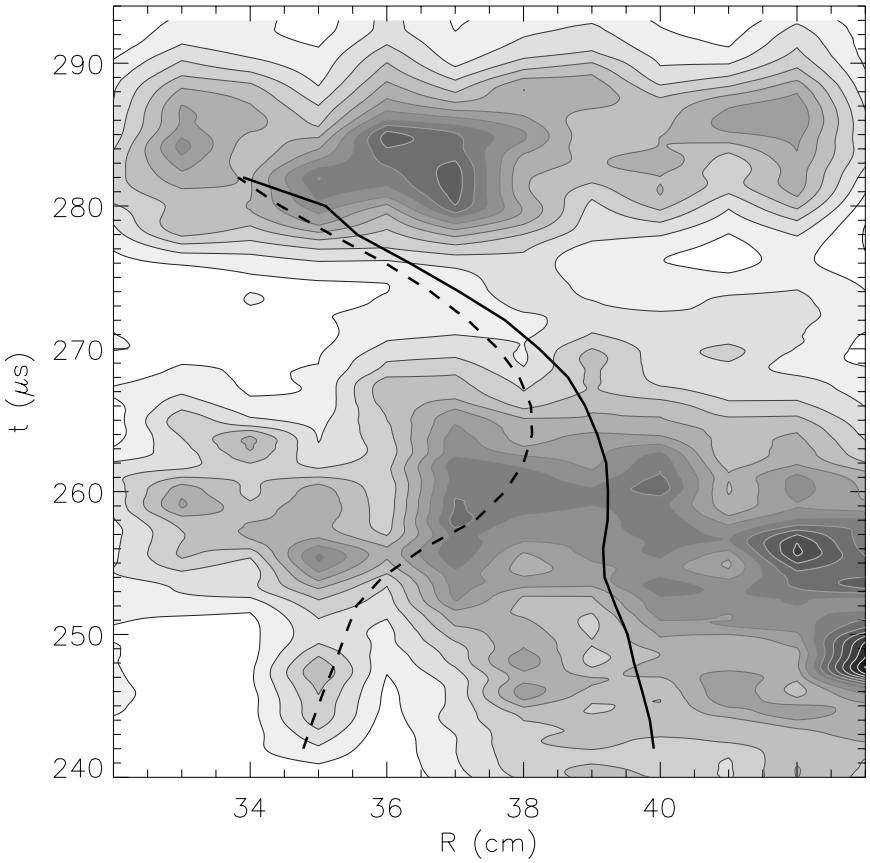

Figure B.5: Contours of rms magnetic fluctuation amplitude using a 100 kHz high-pass filter. Trajectories of the magnetic null (solid line) and the location of peak current density (dotted line) are also shown.

the electric field is seen to rise dramatically, while the total plasma current begins a fairly rapid decay. This event could be interpreted as a disruption of the current sheet current, and could be caused by an instability associated with the third class of magnetic signals. An instability which is predicted to have characteristics quite similar to this third class of magnetic signals ($\omega \sim \Omega_i$) is the drift-kink instability (DKI) [ZHU and WINGLEE, 1996]. Three-dimensional particle simulations of reconnection by HORIUCHI and SATO [1999] show a similar picture to the observations presented in this appendix: the LHDI grows on the edge of the current sheet,

but dissipates in strength as the DKI grows in the center of the current sheet. This possibility is quite interesting, as the DKI has never before been observed in any plasma, yet has been invoked often in the theoretical literature. Currently, there is an active theoretical debate over whether the growth rate of the DKI can be significant anywhere other than in particle simulations with artificially low values of m_e/m_i [DAUGHTON, 1999]. If this is an observation of the DKI, the detailed characterization of this instability in MRX would be quite a contribution. However, there is a less provocative alternative explanation for these signals. Current sheets formed in MRX are "line-tied" to the flux cores during current sheet formation and reconnection. The tension provided by the field lines surrounding both the current sheet and the flux cores provides some stabilizing influence against any unstable motion of the current sheet. At late times, reconnection has depleted the number of lines which are "tying" the current sheet to the flux cores, and the current sheet may "pinch-off" from the flux cores as an independent object. This pinching-off was exploited in spheromak formation using flux cores in the S-1 spheromak [YAMADA *et al.*, 1981]. Once the current sheet has been separated from the flux cores, any number of unstable motions of the new separated object (FRC-like in the null-helicity case) may occur (e.g. tilting) that might lead to the signals observed at late time.

We can now make some comments on the relevance of the observed magnetic fluctuations to the process of reconnection in MRX. While the third class of fluctuations may have dramatic effects on the current sheet late in time, they occur too late to be important during the quasi-steady phase of reconnection. It is interesting to note that both the magnetic LHDI and the second class of magnetic signals have similar time behavior as the quasi-steady phase of reconnection begins, as

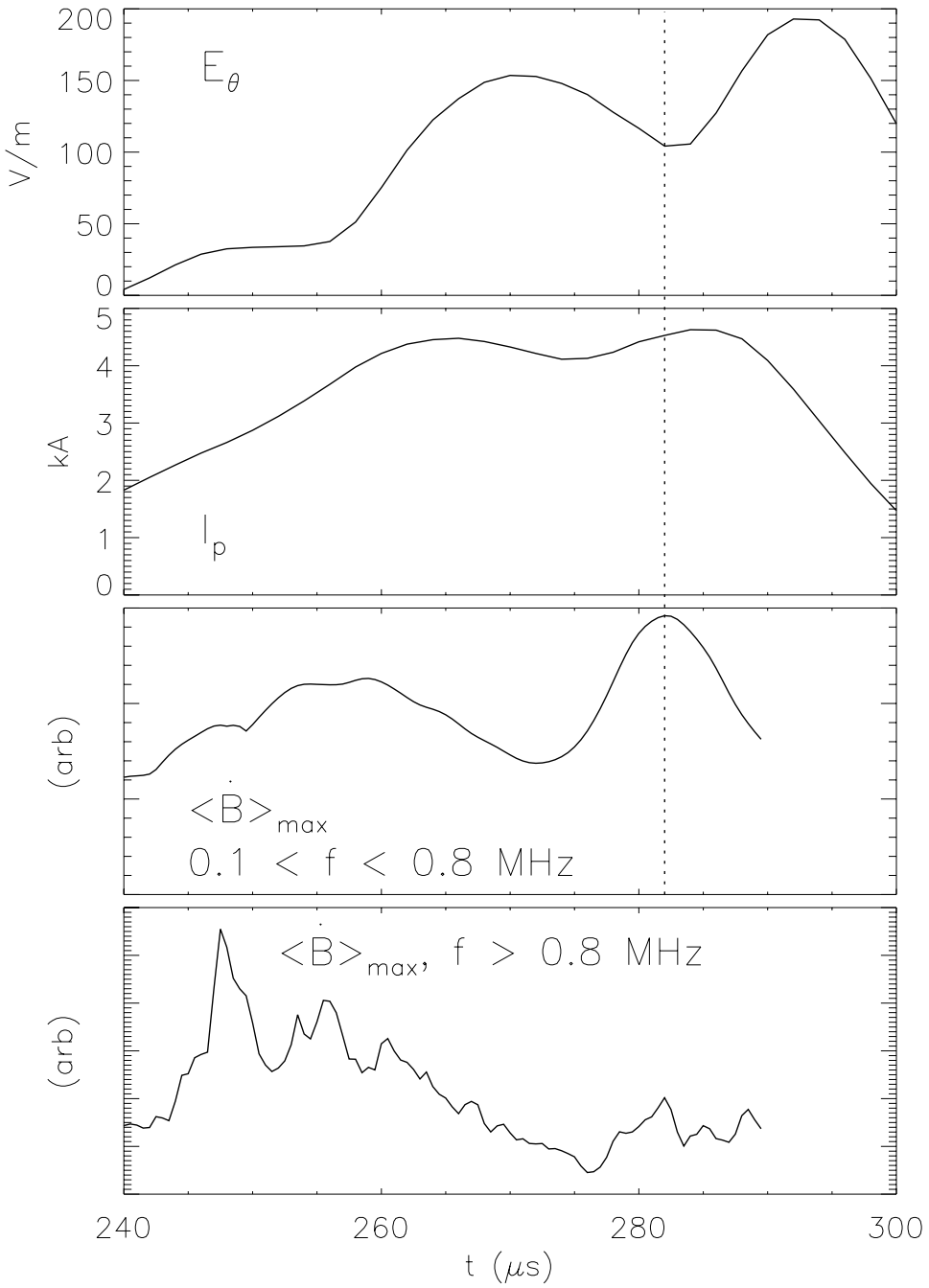

Figure B.6: Time history of reconnection electric field (E_θ), total plasma current (I_p), and peak magnetic fluctuation amplitude for low (0.1MHz $< f <$ 0.8MHz) and high ($f >$ 0.8MHz) frequency fluctuations. The dotted line indicates the time of peak amplitude of the late-time, low-frequency signals.

shown in the bottom plot in Figure B.6 or in the contour plots in Figures B.2 and B.5. On average, the fluctuation amplitude of both types of signals drops off early in the reconnection process, in a similar manner to the electrostatic LHDI signals discussed in Chapter 4. In addition, while significant amplitude is seen near the magnetic null early in time (where $\delta B/B$ must be quite large), the second class of fluctuations seems to be driven by an energy source that may have little to do with the presence of a current sheet. The low frequency plot in Figure B.6 also shows peaking early in the reconnection process, but finite amplitude remains during the quasi-steady reconnection phase. The remaining amplitude is dominated by the low-end of the frequency range, and is likely due to $5 - 10\mu s$ features associated with macroscopic motions of the current sheet that are unlikely to contribute any resistive effect. These observations are preliminary and certainly do not conclusively rule out important roles of these additional fluctuations during reconnection in MRX. However, these observations do not provide any substantial support for overturning the primary conclusion of this thesis: that constructing a theoretical picture of reconnection in MRX based on turbulent resistivity has become quite difficult due to the measurements presented herein.

Bibliography

ANTIOCHOS, S., DEVORE, C., and KLIMCHUK, J. (1999). A model for solar coronal mass ejections. *Ap. J.* **510**, 485.

AREFEV, V. (1970). Instability of a current-carrying homogeneous plasma. *Sov. Phys. Tech. Phys.* **14**, 1487.

BAUM, P. and BRATENAHL, A. (1974). Spectrum of turbulence at a magnetic neutral point. *Phys. Fluids* **17**, 1232.

BEALL, J., KIM, Y., and POWERS, E. (1982). Estimation of wavenumber and frequency spectra using fixed probe pairs. *J. Appl. Phys.* **53**, 933.

BENJAMIN, N. (1982). High-impedance capacitive divider probe for potential measurements in plasmas. *Rev. Sci. Inst.* **10**, 1541.

BIRN, J., DRAKE, J., SHAY, M., ROGERS, B., DENTON, R., HESSE, M., KUZNETSOVA, M., MA, Z., BHATTACHARGEE, A., OTTO, A., and PRITCHETT, P. (2001). Geomagnetic Environmental Modeling (GEM) Magnetic Reconnection Challenge. *J. Geophys. Res. Space. Phys.* **106**, 3715.

BISKAMP, D. (1986). Magnetic reconnection via current sheets. *Phys. Fluids* **29**, 1520.

BISKAMP, D. (1994). Magnetic reconnection. *Phys. Rep.* **237**, 179.

BRACKBILL, J., FORSLUND, D., QUEST, K., and WINSKE, D. (1984). Nonlinear evolution of the lower-hybrid drift instability. *Phys. Fluids* **27**, 2682.

BUNEMAN, O. (1958). Instability, Turbulence, and Conductivity in Current-Carrying Plasma. *Phys. Rev. Lett.* **1**, 8.

BURKHART, G., DRAKE, J., DUSENBURY, P., and SPEISER, T. (1992). A particle model for magnetotail neutral sheet equilibria. *J. Geophys. Res.* **97**, 13799.

CHEN, S.-L. and SEKIGUCHI, T. (1965). Instantaneous direct-display system of plasma parameters by means of triple probe. *J. Appl. Phys.* **36**, 2363.

CHEN, Y. and BIRDSALL, C. (1983). Lower-hybrid drift instability saturation mechanisms in one dimension. *Phys. Fluids* **26**, 180.

CHEN, Y., NEVINS, W., and BIRDSALL, C. (1983). Stabilization of the lower-hybrid drift instability by resonant electrons. *Phys. Fluids* **26**, 2501.

CHOUEIRI, E., KELLY, A., and JAHN, R. (1991). Current-driven plasma acceleration versus current-driven energy dissipation part II : Electromagnetic wave stability theory and experiments. In *Proceedings of the 22nd International Electric Propulsion Conference*, page 91, Pisa, Italy.

CORONITI, F. and EVITAR, A. (1977). Magnetic Field Reconnection in a Collisionless Plasma. *Ap. J. Suppl. Series* **33**, 89.

DAUGHTON, W. (1999). The unstable eigenmodes of a neutral sheet. *Phys. Plasmas* **6**, 1329.

DAVIDSON, R. (1978). Quasilinear stabilization of the lower-hybrid-drift instability. *Physics of Fluids* **21**, 1376.

DAVIDSON, R. and GLADD, N. (1975). Anomalous transport properties associated with the lower-hybrid drift instability. *Phys. Fluids* **18**, 1327.

DAVIDSON, R., GLADD, N., WU, C., and HUBA, J. (1977). Effects of finite plasma beta on the lower-hybrid drift instability. *Phys. Fluids* **20**, 301.

DRAKE, J. (1997). Breakup of the electron current layer during 3-D collisionless magnetic reconnection. *Geophys. Res. Lett.* **24**, 2921.

DRAKE, J., GUZDAR, P., HASSAM, A., and HUBA, J. (1984). Nonlinear mode coupling theory of the lower-hybrid-drift instability. *Physics of Fluids* **27**, 1148.

EGEDAL, J. and FASOLI, A. (2001a). Collisionless magnetic reconnection in a toroidal cusp. *Phys. Plasmas* **8**, 1935.

EGEDAL, J. and FASOLI, A. (2001b). Single-particle dynamics in collisionless magnetic reconnection. *Phys. Rev. Lett.* **86**, 5047.

FAHRBACH, H., KÖPPENDÖRFER, W., MÜNICH, M., NEUHAUSER, J., RÖHR, H., SCHRAMM, G., SOMMER, J., and HOLZHAUER, E. (1981). Measurement of lower hybrid drift fluctuations in the boundary layer of a high-beta plasma by collective CO2 laser light scattering. *Nuclear Fusion* **21**, 257.

GARY, S. (1980). Wave-particle transport from electrostatic instabilities. *Phys. Fluids* **23**, 1193.

GEKELMAN, W. and STENZEL, R. (1984). Magnetic field line reconnection experiments 6. Magnetic Turbulence. *J. Geophys. Res.* **89**, 2715.

GEKELMAN, W. and STENZEL, R. (1985). Measurement and instability analysis of three-dimensional anisotropic electron distribution functions. *Phys. Rev. Lett.* **54**, 2414.

GLASSER, A. and COHEN, S. (2001). Electron acceleration in the field-reversed configuration (FRC) by slowly rotating odd-parity magnetic fields (RMF). Technical Report PPPL-3554, Princeton Plasma Physics Laboratory.

GRIFFITHS, D. (1989). *Introduction to electrodynamics*. Prentice Hall.

GURNETT, D., FRANK, L., and LEPPING, R. (1976). Plasma waves in the distant magnetotail. *J. Geophys. Res.* **81**, 6059.

HAERENDEL, G. (1978). Microscopic plasma processes related to reconnection. *J. Atmos. Terr. Phys.* **40**, 343.

HAMBURGER, S. and FRIEDMAN, M. (1968). Electrical conductivity of a highly turbulent plasma. *Phys. Rev. Lett.* **21**, 674.

HARRIS, E. (1962). On a plasma sheath separating regions of oppositely directed magnetic field. *Il Nuovu Cimento* **23**, 115.

HEYVAERTS, J., PRIEST, E., and RUST, D. (1977). An emerging flux model for the solar flare phenomenon. *Ap. J.* **216**, 123.

HORIUCHI, R. and SATO, T. (1999). Three-dimensional particle simulation of plasma instabilities and collisionless reconnection in a current sheet. *Phys. Plasmas* **6**, 4565.

HOWELL, R. and NAGAYAMA, Y. (1985). Ion energy measurements on a reversed-field pinch experiment using Doppler broadening. *Phys. Fluids* **28**, 743.

HSU, S. (2000). *Experimental study of ion heating and acclereration during magnetic reconnection*. PhD thesis, Princeton University.

HSU, S., CARTER, T., FIKSEL, G., JI, H., KULSRUD, R., and YAMADA, M. (2001). Experimental study of ion heating and acceleration during magnetic reconnection. *Phys. Plasmas* **8**, 1916.

HSU, S., FIKSEL, G., CARTER, T., JI, H., KULSRUD, R., and YAMADA, M. (2000). Local measurement of nonclassical ion heating during magnetic reconnection. *Phys. Rev. Lett.* **84**, 3859.

HUBA, J., GLADD, N., and PAPADOPOULOS, K. (1977). The lower-hybrid-drift instability as a source of anomalous resistivity for magnetic field line reconnection. *Geophys. Res. Lett.* **4**, 125.

HUBA, J., GLADD, N., and PAPADOPOULOS, K. (1978). Lower-hybrid-drift wave turbulence in the distant magnetotail. *J. Geophys. Res.* **83**, 5217.

HUBA, J. and OSSAKOW, S. (1981). On 11-cm irregularities during equatorial spread F. *J. Geophys. Res.* **86**, 829.

HUBA, J. and PAPADOPOULOS, K. (1978). Nonlinear stabilization of the lower-hybrid drift instability by electron resonance broadening. *Phys. Fluids* **21**, 121.

HUBA, J. and WU, C. (1976). Effects of a magnetic field gradient on the lower hybrid drift instability. *Phys. Fluids* **19**, 988.

HUTCHINSON, I. (1987). *Principles of plasma diagnostics*. Cambridge University Press.

JACKSON, J. (1998). *Classical electrodynamics*. John Wiley and Sons.

JI, H., YAMADA, M., HSU, S., and KULSRUD, R. (1998). Experimental Test of the Sweet-Parker Model of Magnetic Reconnection. *Phys. Rev. Lett.* **80**, 3256.

JI, H., YAMADA, M., HSU, S., KULSRUD, R., CARTER, T., and ZAHARIA, S. (1999). Magnetic Reconnection with Sweet-Parker characteristics in two-dimensional laboratory plasmas. *Phys. Plasmas* **6**, 1743.

KRALL, N. and LIEWER, P. (1971). Low-frequency instabilities in magnetic pulses. *Physical Review A* **4**, 2094.

KRALL, N. and ROSENBLUTH, M. (1962). Trapping instabilities in a slightly inhomogeneous plasma. *Phys. Fluids* **5**, 1435.

KULSRUD, R. (1998). Magnetic reconnection in a magnetohydrodynamic plasma. *Phys. Plasmas* **5**, 1599.

KULSRUD, R. (2001). private communication.

MASUDA, S., KOSUGI, T., HARA, H., TSUNETA, S., and OGAWARA, Y. (1994). A loop-top hard X-ray source in a compact solar flare as evidence for magnetic reconnection. *Nature* **371**, 495.

MCPHERRON, R. (1979). Magnetospheric substorms. *Rev. Geophys. Space Phys.* **17**, 657.

PARKER, E. (1957). Sweet's mechanism for merging magnetic fields in conducting fluids. *J. Geophys. Res.* **62**, 509.

PETSCHEK, H. (1963). Magnetic field annhilation. In *Physics of Solar Flares*, page 425.

PREIST, E., FOLEY, C., HEYVAERTS, J., ARBER, T., CULHANE, J., and ACTON, W. (1998). Nature of the heating mechanism for the diffuse solar corona. *Nature* **393**, 545.

PRITCHETT, P., CORONITI, F., and DECYK, V. (1996). Three-dimensional stability of thin quasi-neutral current sheets. *J. Geophys. Res.* **101**, 27413.

ROGERS, B., DRAKE, J., and SHAY, M. (2000). The onset of turbulence in collisionless magnetic reconnection. *Geophys. Res. Lett.* **27**, 3157.

SHAY, M., DRAKE, J., DENTON, R., and BISKAMP, D. (1998). Structure of the dissipation region during collisionless magnetic reconnection. *J. Geophys. Res.* **103**, 9165.

SHINOHARA, I. and HOSHINO, M. (1999). Electron heating process of the lower hybrid drift instability. *Adv. Space Res.* **24**, 43.

SHINOHARA, I., NAGAI, T., FUJIMOTO, M., TERASAWA, T., MUKAI, T., TSURUDA, K., and YAMAMOTO, T. (1998). Low-frequency electromagnetic turbulence observed near the substorm onset site. *J. Geophys. Res.* **103**, 20365.

SPEISER, T. (1970). Conductivity without collisions or noise. *Planet. Space Sci.* **18**, 613.

STIX, T. (1992). *Waves in Plasmas*. American Institute of Physics.

SWEET, P. (1958). In LEHNERT, B., editor, *Electromagnetic Phenomena in Cosmical Physics*, page 123. Cambridge Univ. Press, New York.

SYROVATSKII, S. (1971). Formation of current sheets in a plasma with a frozen-in strong magnetic field. *Sov. Phys. JETP* **33**, 933.

SYROVATSKII, S. (1972). Critical problems of magnetospheric physics. In DYER, E., editor, *Solar terrestrial physics*, page 119. National Academy of Sciences.

TANAKA, M. and SATO, T. (1981). Simulations on lower hybrid drift instability and anomalous resistivity in the magnetic neutral sheet. *J. Geophys. Res.* **86**, 5541.

TILLEY, D., CHOUEIRI, E., KELLY, A., and JAHN, R. (1996). Microinstabilities in a 10-kilowatt self-field magnetoplasmadynamic thruster. *J. Propul. Power* **12**, 381.

TRINTCHOUK, F., YAMADA, M., JI, H., KULSRUD, R., and CARTER, T. (2001). Measurement of the transverse Spitzer resistivity during collisional magnetic reconnection. to be submitted to PRL.

UGAI, M. (1995). Computer studies on powerful magnetic energy conversion by the spontaneous fast magnetic reconneciton mechanism. *Phys. Plasmas* **2**, 388.

UZDENSKY, D. and KULSRUD, R. (2000). Two-dimensional numerical simulation of the resistive reconnection layer. *Phys. Plasmas* **7**, 4018.

WINSKE, D. (1981). Current-driven microinstabilities in a neutral sheet. *Phys. Fluids* **24**, 1069.

WINSKE, D. and HEWETT, D. (1975). Flute instabilities in 2-dimensional simulations of strongly inhomogeneous theta-pinch plasmas. *Phys. Rev. Lett.* **35**, 937.

WINSKE, D. and LIEWER, P. (1978). Particle simulation studies of the lower-hybrid drift instability. *Phys. Fluids* **21**, 1017.

WU, C., ZHOU, Y., TSAI, S., and GUO, S. (1983). A kinetic cross-field streaming instability. *Phys. Fluids* **26**, 1259.

YAMADA, M., FURTH, H., HSU, W., JANOS, A., JARDIN, S., OKABAYASHI, M., SINNIS, J., STIX, T., and YAMAZAKI, K. (1981). Quasistatic formation of the spheromak plasma configuration. *Phys. Rev. Lett.* **46**, 188.

YAMADA, M., JI, H., HSU, S., CARTER, T., KULSRUD, R., BRETZ, N., JOBES, F., ONO, Y., and PERKINS, F. (1997a). Study of driven magnetic reconnection in a laboratory plasma. *Phys. Plasmas* **4**, 1936.

YAMADA, M., JI, H., HSU, S., CARTER, T., KULSRUD, R., ONO, Y., and PERKINS, F. (1997b). Identification of Y-shaped and O-shaped diffusion regions during magnetic reconnection in a laboratory plasma. *Phys. Rev. Lett.* **78**, 3117.

YAMADA, M., JI, H., HSU, S., CARTER, T., KULSRUD, R., and TRINTCHOUK, F. (2000). Experimental investigation of the neutral sheet profile during magnetic reconnection. *Phys. Plas.* **7**, 1781.

YAMADA, M., LEVINTON, F., POMPHREY, N., BUDNY, R., MANICKAM, J., and NAGAYAMA, Y. (1994). Investigation of magnetic reconnection during a sawtooth crash in a high-temperature tokamak plasma. *Phys. Plasmas* **1**.

YAMADA, M. and OWENS, D. (1977). Cross-field-current lower-hybrid instability and stochastic ion heating. *Phys. Rev. Lett.* **38**, 1529.

YAMANAKA, K. (1977). Threshold of electromagnetic instability in a magnetic neutral sheet. *Physica Scripta* **17**, 15.

YOON, P. (2001). Private communication.

YOON, P., LUI, A., and CHANG, C. (1994). Lower-hybrid-drift instability operative in the geomagnetic tail. *Phys. Plasmas* **1**, 3033.

ZHU, Z. and WINGLEE, R. (1996). Tearing instability, flux ropes, and the kinetic current sheet instability in the Earth's magnetotail: A three-dimensional perspective. *J. Geophys. Res.* **101**, 4885.